Remote Sensing of Environment 344 (2026) 115505

Contents lists available at ScienceDirect

Remote Sensing of Environment

journal homepage: www.elsevier.com/locate/rse

CAMS radiation service v4.6 for solar energy: Evaluation of Himawari based surface solar irradiance products

Faiza Azam[a,*], Diego Rodrigues de Miranda[a], Marion Schroedter-Homscheidt[a], Mireille Lefèvre[b], Laurent Saboret[c], Yves-Marie Saint-Drenan[b]

[a] Deutsches Zentrum für Luft- und Raumfahrt (DLR) e.V., Institute of Networked Energy Systems, Carl-von-Ossietzky-Str. 15, 26129 Oldenburg, Germany
[b] MINES Paris, Université PSL Centre Observation Impacts Energie (O.I.E.), 1 Rue Claude Daunesse, 06904 Sophia-Antipolis, France
[c] Vaisala, Spaces Les Templiers, 950 Route Des Colles, 06410 Biot, France

ARTICLE INFO

Editor by: Menghua Wang

Keywords:
CAMS radiation service
Surface solar irradiance
Geostationary satellites
HIMAWARI
Sky conditions
Cloud type
Retrieval uncertainty
Solar energy

ABSTRACT

The Copernicus Atmospheric Monitoring Service (CAMS) offers solar radiation service (CRS) which provides time series of surface solar irradiance (SSI) as its primary product. As a first step towards the global evolution of the service for solar energy applications, the Himawari measurements by Japan Meteorological Agency (JMA) are integrated since version 4.6. This study introduces a hierarchical evaluation framework and evaluates CRS for 32 stations distributed in different climates inside the Himawari field of view (FOV). Besides standard all-sky validation the framework includes APOLLO_NG cloud-type specific evaluation as well as seasonal, diurnal and interannual variability. The assessment is further deepened with the establishment of an irradiance variability based classification as a diagnostic tool for SSI validation allowing quantitative evaluation of various error sources due to different cloud conditions on the retrieval performance. The rMBE and rRMSE in all-sky conditions are in the ranges −7.4 to 4.9% and 8 to 30% for hourly Global Horizontal Irradiance (GHI), and − 26.6 to 15.3% and 18 to 64.1% for Beam Normal Irradiance (BNI), respectively. The evaluations show very good performance of CRS schemes under clear-sky and nearly clear-sky conditions and good handlings of thin clouds in most stations. However, broken cloud fields are observed to introduce notable overestimation. While a direct comparison with other validation studies for the Himawari FOV is limited due to differences in temporal and spatial coverage, CRS v4.6 achieved overall performance levels comparable to or better than other published approaches.

1. Introduction

Solar energy is projected to become a dominant source of energy in the global energy mix before the mid of this century (IEA, 2022; Nijsse et al., 2023). Information on solar radiation time series of appropriate spatiotemporal resolution is important for resource assessment, system performance prediction and monitoring, grid integration and management as well as energy forecasting. Geostationary satellites are widely used to generate surface solar irradiance (SSI) products. They are capable of providing the spatial distribution and dynamic evolution of atmospheric contents such as clouds which are the primary modulators of SSI. The cloud evolution, movement, cloud type (phase, shape and size distribution) and its optical properties influence the magnitude and the spatiotemporal variability of the SSI in a non-linear and dynamic manner (Sengupta et al., 2018; Lopez et al., 2024; Mol et al., 2023, 2024). Unlike ground measurements, satellite imagery offers a large spatial coverage, and delivers SSI estimates with a better accuracy as compared to numerical weather prediction models (Urraca et al., 2018; Verbois et al., 2023).

Geostationary satellite-based SSI retrieval dates back to around 1980 with the application of empirical statistical or simple physical radiative transfer modeling approaches (Tarpley, 1979; Gautier et al., 1980; Möser and Raschke, 1984; Pinker and Ewing, 1985; Cano et al., 1986; Schmetz, 1989). Early statistical approaches typically used the cloud transmission or the clearness index (Beyer et al., 1996; Perez et al., 2002; Hammer et al., 2003; Rigollier et al., 2004), while later developments introduced fast radiative transfer parameterizations using atmospheric state variables (Pinker and Laszlo, 1992; Pinker et al., 2002; Deneke

* Corresponding author at: Deutsches Zentrum für Luft- und Raumfahrt (DLR) e.V, Institute of Networked Energy Systems, Carl-von-Ossietzky-Str. 15, 26129 Oldenburg, Germany.
E-mail address: faiza.azam@dlr.de (F. Azam).

https://doi.org/10.1016/j.rse.2026.115505
Received 26 September 2025; Received in revised form 1 May 2026; Accepted 25 May 2026
Available online 11 June 2026

et al., 2008; Geiger et al., 2008; Mueller et al., 2009; Greuell et al., 2013; Xie et al., 2016; Qu et al., 2017; Sengupta et al., 2018; Laszlo et al., 2020; Letu et al., 2020, 2022, 2023). Among these methods, the Heliosat family of algorithms has become one of the most widely used method for operational irradiance retrieval from geostationary satellite observations. Earlier versions of Heliosat relied on cloud-index approaches, whereas Heliosat-4 (Qu et al., 2017) belongs to the class of fast radiative transfer model-based retrieval schemes.

Most geostationary satellite-based SSI retrieval algorithms have been developed over time using observations from Meteosat satellites over Europe, Africa, the Middle East and parts of South America, or from the Geostationary Operational Environmental Satellites (GOES) over the Americas. With the launch of the Himawari geostationary satellites equipped with Advanced Himawari Imager (AHI) instruments, several studies have investigated SSI retrieval for the Asia-Oceania region (e.g. Shi et al., 2018; Damiani et al., 2018; Qin et al., 2021; Bright, 2019; Hou et al., 2020; Ma et al., 2020; Yu et al., 2019; Letu et al., 2022, Letu et al., 2023; Yu et al., 2021; ABoM, 2022; Tan et al., 2023; Li et al., 2023; Valor et al., 2023; Meher et al., 2024). These studies employ a range of approaches including physical retrieval methods, cloud-index based models previously implemented for MSG and GOES, and machine learning techniques adapted to the spectral characteristics of Himawari observations.

More recently, the application of the data driven, machine learning, and hybrid approaches is also emerging in the SSI estimation (Takenaka et al., 2011, Linares-Rodriguez et al., 2013; Jiang et al., 2019; Hao et al., 2020; Hou et al., 2020; Ma et al., 2020; Tan et al., 2023, Verbois et al., 2023, Schuurman and Meyer, 2024). For these methods, the challenges of providing physical explanations and generalization are a topic of current research (Verbois et al., 2023; Schuurman and Meyer, 2024).

These methodological developments have enabled several operational satellite-based SSI services, which provide irradiance data for climate monitoring and solar energy applications. Examples include the CAMS Radiation Service (CRS), which is the subject of this study. Other services are based on polar-orbiting satellites, such as the Clouds and the Earth's Radiant Energy System (CERES) or the Hi-GLASS (High-resolution Global LAnd Surface Satellite) (Jiang et al., 2023), as well as geostationary satellite-based services including the Satellite Application Facility on Climate Monitoring (CM SAF) Surface Solar Radiation Dataset – Heliosat (SARAH), the National Solar Radiation Database (NSRDB), the Japanese Aerospace Exploration Agency (JAXA) p-tree system and the Australian Bureau of Meteorology (ABoM) radiation service. In addition, several commercial providers such as SolarGIS, Solcast, and Meteotest offer satellite-derived irradiance datasets, often incorporating post-processing using ground observations to improve product accuracy. Regional datasets are also provided by institutions such as the Commonwealth Scientific and Industrial Research Organisation (CSIRO) for the Australian continent. Radiation products based on polar orbiters such as CERES or Hi-GLASS are generally intended for climate studies, whereas datasets based on high temporal resolution from geostationary orbits such as CRS, SARAH, NSRDB, or SolarGIS provide SSI products well suited for solar resource assessment.

These datasets primarily provide spatially gridded irradiance products which differ in spatial and temporal resolution and the intended usage, whereas the CRS provides high temporal resolution point-based irradiance time series as its primary product which is the focus of the presented analyses. Only as secondary derived product, CRS provides a gridded dataset for land and coastal areas within the satellite field of view (FOV).

In contrast to other operational services, CRS provides besides global, diffuse and direct radiation components also the detailed input of atmospheric variables (e.g. aerosols, water vapor, and albedo) used for the clear sky modeling, the cloud parameters from APOLLO_NG, and the solar geometry information. This detailed input and output characteristics allow a broader usage of CRS in the solar energy field such as solar resource assessment, plant performance monitoring, power forecasting, grid integration, including a close interaction with machine learning based approaches in these application fields. In addition, point-based products as in the CRS allow direct and consistent comparison with ground measurements of SSI used for validation.

Many of these satellite derived SSI datasets, including the CRS, have been intercompared within the worldwide benchmark of SSI products conducted under the IEA-PVPS Task 16 framework (Forstinger et al., 2023), which provides a comprehensive evaluation of these datasets across different climatic regions and with the focus on solar energy applications.

Most of the mentioned studies evaluate irradiances using standard statistical comparisons, typically at temporal resolutions of 10 min or longer and occasionally distinguishing between cloud-free and cloudy conditions. They offer limited insight into the atmospheric conditions or sky regimes that drive retrieval uncertainties.

The present study introduces a hierarchical physically interpretable diagnostic evaluation framework. This approach enables a more detailed analysis of retrieval uncertainties compared with conventional validation studies. Besides providing descriptive performance statistics, the framework is designed to support targeted improvement of SSI retrieval schemes. By identifying retrieval performance under physically interpretable atmospheric regimes, the framework is expected to provide guidance for future developments. In addition to standard cloud-free and all-sky validation, the analysis combines cloud-type discrimination and irradiance variability classification derived from one-minute ground observations. In this study, variability classes derived from GHI minute measurements (de Miranda et al., 2026) are used as an evaluation tool. By linking cloud retrieval characteristics from APOLLO_NG with irradiance variability phenomena due to different atmospheric states, this approach allows a more detailed identification of the atmospheric regimes such as thin cirrus, multilayer clouds, and broken cloud fields as well as the quantification of uncertainties of satellite-derived irradiance retrievals in these conditions. Cho et al. (2015) and references therein discuss frequency and causes of failing cloud property retrievals in depth. They also provide a review of the relevant literature of cloud retrieval errors. The focus of our study is to quantify the effects of various cloud and retrieval conditions on the accuracy as a new assessment method from the user perspective. The objective of this study is therefore to introduce and demonstrate a diagnostic evaluation framework that supports future retrieval development, rather than to implement new retrieval parameterizations within the presented work. This provides additional scientific insight into the behavior and limitations of nowadays operational SSI retrieval schemes and especially the CRS v4.6.

Section 2 outlines the Himawari data exploited in the SSI retrieval, the ground data used in the evaluations and the quality control carried out in the CAMS regular evaluations and also followed in the present assessment. Section 3 explains new implementations of the cloud retrieval algorithm APOLLO_NG and Heliosat-4 for SSI retrieval for the Himawari FOV. Section 4 describes the evaluation results of CRS SSI products with a special focus on the assessment under different sky conditions as well as on diurnal, seasonal, and interannual variations, and Section 5 points to the main conclusions and outlooks.

2. Data

2.1. Himawari and CRS data

Operationally, CRS uses Himawari series i.e. Himawari-8/9 data received through the EUMETSAT EUMETCast service as full disk L1C data at 2 km and 10 min resolutions. EUMETSAT receives the calibrated and geolocated data in native resolution from the Japanese Meteorological Agency (JMA) in Himawari Standard Format (HSD) for each of the 16 channels ranging from 0.46 to 13.3 μm. EUMETSAT converts the data to HRIT format prior to near-real-time redistribution where each channel is geographically split into 10 segments. For gap-filling in CRS, the Himawari archive data from the Australian Bureau of Meteorology (ABoM) available through an OPeNDAP (Open-source Project for a Network Data Access Protocol) is used. AGLS-OBS (Applications from GEO and LEO Satellites Project – Observation product) contains full disk scan files for each of the 16 Himawari bands, per time resolution and in native spatial resolution.

CRS provides the time series of the global, diffuse and the beam horizontal and normal irradiance (GHI, DHI, BHI and BNI respectively) and their clear-sky counterparts as its primary product in 1 min, 15 min, hourly and daily temporal resolution currently with a one-day delay mode. The data is operationally available at the CAMS Atmospheric Data Store (ADS, https://ads.atmosphere.copernicus.eu/datasets/cams-solar-radiation-timeseries) and can also be accessed through the Python package pvlib since its v0.9.0 release. Users can also obtain all input parameters as aerosols, water vapor, albedo, ozone, solar geometry, and cloud information in 1 min resolution via the expert mode. The time series are available for Meteosat Second Generation (MSG) field of view (FOV) since 2004 and for Himawari since 2016. In addition, a pre-processed gridded dataset over land and coastal surfaces in the MSG and Himawari FOV is also available. The gridded dataset is based on a retrieved collection of the primary time series on a 0.1° spatial grid in 15- min temporal resolution which are re-structured to a gridded monthly file for easier access in energy system analysis studies. This data can also be downloaded through the CAMS ADS, but it should be noted that it is a dataset with a lower resolution than the original CRS data.

2.2. Ground observations database

The evaluation of CRS radiation parameters is part of regular CRS activities. This implies dealing with a large number of different data formats and occurrences of various quality issues that need to be efficiently detected, understood, and addressed. The CRS validation activities are supported by a collection and continuous extension of ground-based SSI measurements on a dedicated THREDDS (Thematic Real-time Environmental Distributed Data Services) server and web interface (https://viewer.webservice-energy.org/in-situ/). The data collection is assembled with consolidated metadata, harmonized netCDF structure following Climate and Forecast (CF) conventions and follows the FAIR mode (Findable, Accessible, Interoperable, Reproducible) principle.

In this study, measurements from 32 stations representing a variety of climates in the Himawari FOV for the time period 2016–2025 from the Baseline Surface radiation Network (BSRN, Ohmura et al., 1998; Driemel et al., 2018), the Australian Bureau of Meteorology (ABoM) stations and the International Energy Agency-Photovoltaic Power Systems Programme (IEA-PVPS) Task 16 (dedicated to Solar resources and forecasts), all provided at the THREDDS server, are used. BSRN stations provide ground-based datasets of GHI, BNI, and DHI components in a 1 min temporal resolution. Accuracy requirements for BSRN data are 5 W/m^2 for GHI and 2 W/m^2 for BNI (Ohmura et al., 1998). The ABoM offers 1 min resolved ground observations at BSRN stations in Australia, but also at several additional stations (ABoM, 2012) GHI, BNI and DHI observations, thus increasing the stations coverage for Australia. Their 95% uncertainty targets are 3% or 15 W/m^2. The IEA-PVPS Task 16 collects the data from the local stations distributed under special agreement.

Fig. 1 shows the map view of the stations used in the assessment and Table 1 details the geographical and site specifics.

Ground-based irradiance measurements require rigorous maintenance of the sensors and data quality control. An open source python library libinsitu (Blanc et al., 2022) is developed and used in CRS. Libinsitu provides tools to transform raw input files into NetCDF format, to explore and query NetCDF data, data transformation to various formats, quality checks application, flagging, and production of the visual Quality control (QC) report. Further details on the QC assessment tests and visual report can be found in Appendix A. Fig. 2 depicts the percentage data availability per year for the stations after the application of the QC while Fig. 3 shows the percentage of flagged data for each station after the application of QC. The time period starting from 2016 is selected as the CRS coverage for the Himawari FOV begins with this year. It should be noted that the ABoM services and some of the BSRN stations did not provide any data after the COVID-19 period. Very low percentages of availability are generally not due to quality flagging but due to the data unavailability.

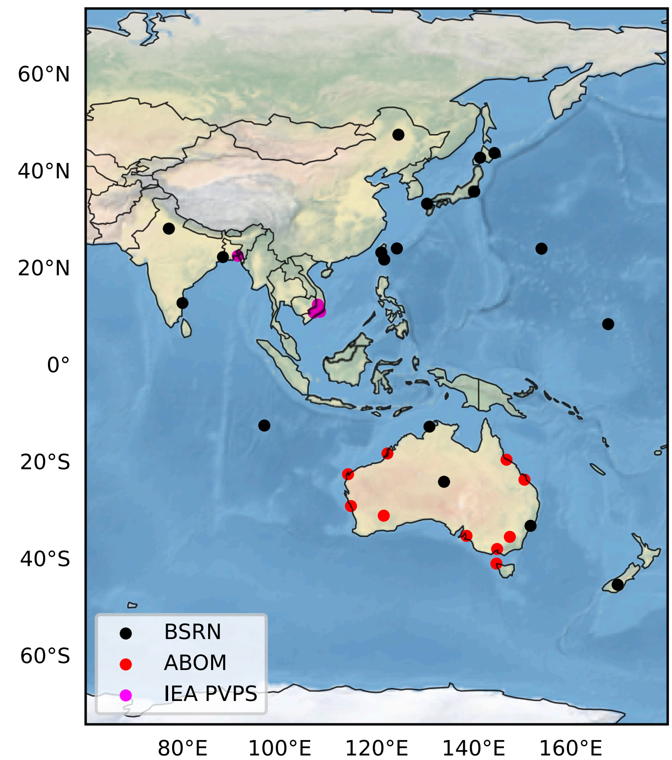

Fig. 1. Map view of the stations in the Himawari field of view used in this study.

3. CRS adaptions to the Himawari FOV

Copernicus Atmospheric Monitoring Service (CAMS) provides SSI products routinely since 2016 through its CAMS Radiation Service (CRS). CRS uses APOLLO_NG (Klüser et al., 2015; Schroedter-Homscheidt et al., 2022) to derive cloud information, which originally used observations from the Spinning Enhanced Visible and InfraRed Imager (SEVIRI) aboard the Meteosat satellites. For the SSI retrieval, the Heliosat-4 retrieval scheme (Lefèvre et al., 2013; Qu et al., 2017; Gschwind et al., 2019) is implemented. While the APOLLO_NG cloud retrieval algorithm and Heliosat-4 irradiance retrieval scheme are existing algorithms within the CRS, their application to the Himawari AHI observations required methodological adaptations and systematic evaluations. These include adjustments related to the spectral characteristics of AHI channels used for cloud detection and optimization and evaluation of the cloud probability threshold used to initiate the cloudy-sky module of Heliosat-4.

The cloud retrieval was updated from APOLLO (AVHRR Processing scheme Over cLouds Land and Ocean) to APOLLO_NG (APOLLO Next Generation) in the CRS version 4.0. Previously applied binary threshold tests for the cloud masking were replaced in APOLLO_NG (Klüser et al., 2015; Schroedter-Homscheidt et al., 2022) with a probabilistic cloud mask using Bayesian statistics. Heliosat-4, a fast physical approximation of the radiative transfer modeling in the atmosphere is composed of separate look-up table (LUT) based SSI models for the clear sky (calculating cloud-free irradiance) and cloudy sky (calculating the irradiance extinction by clouds) namely McClear (Lefèvre et al., 2013; Gschwind

Table 1
Stations available in the Himawari field of view used in this study.

Name	Latitude (°N)	Longitude (°E)	Provider	Short Name	Country	Elevation (m)	VZA (°)	Region type
Bromme	−17.9488	122.234	ABOM	BRO	Australia	9	29.8	Coastal/Subpixel
Townville Areo	−19.25	146.77	ABOM	TOW	Australia	4	23.6	Coastal/Subpixel
Learmonth	−22.2418	114.0957	ABOM	LEA	Australia	6	39.7	Coastal/Subpixel
Rochampton	−23.377	150.4765	ABOM	ROC	Australia	12	29.5	Continental
Geraldton	−28.8047	114.6988	ABOM	GER	Australia	30	44.1	Coastal/Subpixel
Kalgoorlie	−30.7908	121.4613	ABOM	KAL	Australia	368	41.5	Desert
Adelaide	−34.9516	138.5213	ABOM	ADE	Australia	7	40.7	Coastal/Subpixel
Wagga Wagga	−35.1598	147.4562	ABOM	WAG	Australia	213	41.4	Continental
Tullamarine	−37.6672	144.83	ABOM	TUL	Australia	132	43.9	Continental
Cape Grim	−40.6722	144.6883	ABOM	CAP	Australia	92.5	47.2	Coastal/Subpixel
Tateno	36.0581	140.1258	BSRN	TAT	Japan	25	41.8	Continental
Fukuoka	33.5822	130.3764	BSRN	FUA	Japan	3	40.6	Coastal/Subpixel
Minamitorishima	24.2883	153.9833	BSRN	MNM	Japan	7.1	32.1	Coastal/Subpixel
Ishigakijima	24.3367	124.1644	BSRN	ISH	Japan	5.7	34.0	Coastal/Subpixel
Cocos Island	−12.193	96.835	BSRN	COC	Australia	6	52.0	Coastal/Subpixel
Darwin MetOffice	−12.424	130.8925	BSRN	DWN	Australia	32	18.5	Continental
Alice Springs	−23.798	133.888	BSRN	ASP	Australia	547	28.9	Desert
Newcastle	−32.8842	151.7289	BSRN	NEW	Australia	18.5	40.1	Continental
Gurgaon	28.4249	77.156	BSRN	GUR	India	259	75.3	Continental
Tiruvallur	13.0923	79.9738	BSRN	TIR	India	36	69.7	Continental
Howrah	22.5535	88.3064	BSRN	HOW	India	51	63.4	Continental
Yushan Station	23.4876	120.9595	BSRN	YUS	Taiwan	3858	35.3	Mountainous
Lanyu Station	22.037	121.5583	BSRN	LYU	Taiwan	324	33.6	Coastal/Subpixel
Sapporo	43.06	141.3286	BSRN	SAP	Japan	17.2	49.6	Coastal/Subpixel
Abashiri	44.0178	144.2797	BSRN	ABS	Japan	38	50.8	Coastal/Subpixel
Kwajalein	8.72	167.731	BSRN	KWA	Marshall Islands	10	33.0	Coastal/Subpixel
Lauder	−45.045	169.689	BSRN	LAU	NewZealand	350	59.3	Continental
Qiqihar	47.7957	124.4852	BSRN	QIQ	China	170	57.1	Continental
Central Highlands	12.7534	107.8763	IEA_PVPS	CEH	Vietnam	277	40.6	Coastal/Subpixel
Song Binh	11.264	108.3452	IEA_PVPS	SON	Vietnam	61	39.6	Continental
Tri An	11.1024	107.0378	IEA_PVPS	TRI	Vietnam	59	40.9	Coastal/Subpixel
Feni	22.80029	91.35819	IEA_PVPS	FEN	Bangladesh	7	60.6	Coastal/Subpixel

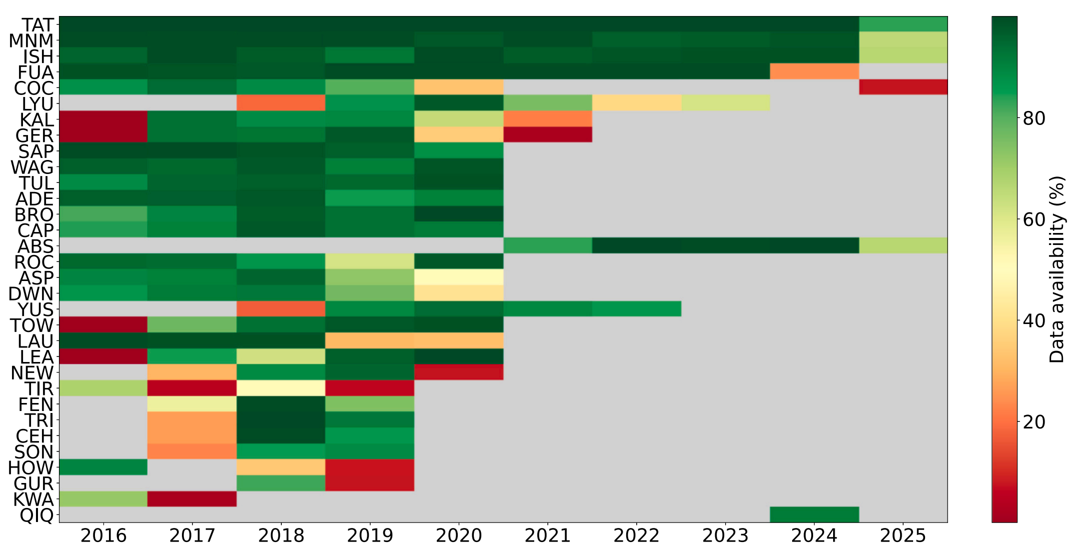

Fig. 2. Percentage availability of data for each station after the application of QC.

et al., 2019) and CAMS-RAD (Qu et al., 2017; Schroedter-Homscheidt et al., 2022) respectively. The LUTs are generated using libRadtran (Mayer and Kylling, 2005 and Mayer et al., 2010). Heliosat-4 uses the inputs on the state of the atmosphere e.g. information on aerosols at 550 nm, total column water vapor and ozone content from the CAMS global forecasting services with 0.4° spatial resolution every 3 h. The solar position is calculated using the SG2 library (Blanc and Wald, 2012). In the clear sky model, the elevation of mountain stations is taken into account for the Rayleigh scattering in the clear sky model. A further correction of the aerosol profile to the location of the station in grid boxes with strongly varying orography is under preparation but not yet available in the operational CRS.

Recent CRS method evolution is provided as an overview in Table 2. The current version 4.6 uses McClear version 3.6 as the clear sky model with the atmospheric input on aerosols, water vapor and ozone taken from most recent CAMS IFS suite. Note that since version 4.5 no bias correction or any tuning to ground observations is applied in the operational CAMS radiation service.

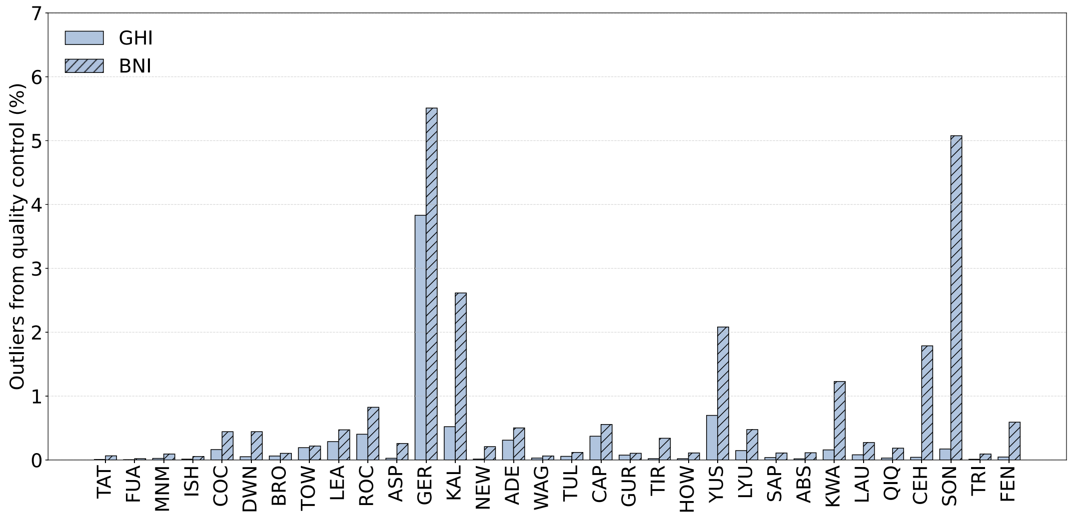

Fig. 3. Percentage of flagged data for each station after QC application.

Several AHI channels have different spectral characteristics compared to the MSG SEVIRI channels, especially the AHI channels 13 (10.4 μm) and 14 (11.2 μm) which are situated inside the SEVIRI 10.8 μm channel bandwidth (see Fig. 4). These channels are used in the Infrared Gross Temperature (IGT), Spatial Coherence Test (SCT), and the T45 cloud mask tests (Klüser et al., 2015). In the IGT 65 × 65 pixels provide a mean value of local brightness temperature and a mean cloud-free background. SCT evaluates large variability in a 3 × 3 pixel neighborhood. The T45 test detects thin clouds and cirrus by a difference in spectral patterns of water and ice phase refractive indices in the two channels. The spectral contrast between Himawari channels 13 (10.4 μm) and 15 (12.38 μm) is more pronounced compared to channels 13 and 14 (11.2 μm). This choice is in line with e.g. the MODIS cloud detection as described in Frey et al. (2008).

The cloud output for the Himawari FOV is in 2 km per 10 min resolution. CRS has an internal temporal resolution of 1 min to take the solar geometry into account. All other input data are used to calculate clearness indices, which are interpolated to the 1 min steps before deriving GHI, BNI and DHI. Therefore, CRS output is in 1 min temporal resolution and only then aggregated to 15, hourly, daily or monthly irradiation, where the aggregation refers to the end of the respective time interval.

The knowledge of the cloud probability from APOLLO_NG renders a flexibility in the selection of the Cloud Probability Threshold (CPT) to produce a cloud mask for the initiation of Heliosat-4. A systematic assessment in a previous study for MSG SEVIRI (Schroedter-Homscheidt et al., 2022) revealed that a cloud probability of 1% is recommended as a threshold to initiate the cloudy module of the Heliosat-4 method. The study was repeated for Himawari observations during the optimization phase of the retrieval with a similar conclusion (Fig. 5). As SSI and especially the BNI is very sensitive to a presence of any small, potentially sub-scale or thin cloud in the pixel, this choice of a very small cloud probability threshold is meaningful.

4. CRS evaluation

The results presented in this section follow a hierarchical diagnostic evaluation framework which was designed to provide a more physically interpretable assessment of retrieval performance beyond conventional statistical validation. The evaluation therefore investigates the behavior of the retrieval across multiple atmospheric regimes, temporal scales, and geographical regions representing different surface types (desert, mountain, continental and coastal regions), while also considering the satellite viewing geometry. The analyses include:

All-sky conditions, including the complete set of observations irrespective of cloud presence, thereby capturing uncertainties associated with cloud detection and cloud property retrieval.

Cloud-type classification, based on the APOLLO_NG cloud retrieval. Cloud-free conditions are identified using the APOLLO_NG cloud mask, while cloudy scenes are grouped into optically thick clouds (APOLLO_NG classes 5–7, representing low-, medium-, and high-level water or mixed phase clouds) and optically thin clouds (type 8, representing thin cirrus). This classification allows the assessment of retrieval performance under cloud conditions with different radiative characteristics.

Variability classification, based on irradiance variability classes derived from 1 min GHI ground observations (de Miranda et al., 2026). These classes represent different irradiance variability conditions and allow the identification of atmospheric situations such as sub-visible clouds, cumulus or broken stratus cloud fields and multilayer cloud systems that are particularly challenging for satellite-based irradiance retrievals.

Temporal variability analyses, including diurnal, seasonal, and interannual variations are performed allowing the assessment of CRS retrieval under different solar zenith angles and daily cloud evolution, systematic changes associated with atmospheric and cloud patterns over the seasons and the stability and robustness of the retrieval across multiple years of Himawari observations. This temporal analysis therefore complements the regime-based evaluation and is meant to contribute to a more comprehensive understanding of the CRS performance.

In addition to performance evaluation, this hierarchical structure enables the isolation of regime-specific error sources, thereby supporting the identification of targeted improvements in the underlying radiative model.

The statistical evaluation presents Mean Bias Error (MBE), defined as the average of CRS estimates minus ground-based observations, and the Root Mean Square Error (RMSE). Relative values are expressed with respect to the mean of the used observations. Statistics are derived from all daytime slots for 60 min averaged observations considering measurements below 80° of solar zenith angle. Averaging is done only if at least 42 observations out of the 60 possible timestamps were valid (30% tolerance to invalid values).

Our SSI validation presented here cannot be compared one-to-one to the results of the existing aforementioned literature. Most studies evaluated the SSI time series extracted from coarser gridded data at 5 km spatial resolution. Furthermore, they deal with different sets of ground stations. Their reported results differ in the collocation criteria

Table 2
Improvements and differences among different CAMS Radiation Service versions

Model parameters		CRS 3.2 2018	CRS 4.0 June 2021	CRS 4.5 Sept. 2022	CRS 4.6 June 2023
Calibration		Reflectances provided by EUMETSAT	Time-dependent updated calibration (Meirink et al. 2013)	same	same
Cloud retrieval		APOLLO, binary cloud mask (Saunders and Kriebel, 1988 & Kriebel et al., 1989)	APOLLO-NG, probabilistic cloud mask (Klüser et al., 2015)	same	same
		Cloud optical thickness (COT) Stephens et al., 1984, clipping COT <0.5	COT using Stephens et al., 1984 scheme. COT LUTs extended to 0.001	same	same
Cloudy/Clear decision Heliosat-4		Based on a binary mask	Cloud probability threshold 1%	same	same
Circumsolar correction		Single COT value	Empirical apparent COT factor for BNI • 0.41 for thin ice clouds • 0.20 for water/mixed clouds	same	Improved parametrization
Aerosol /TWC/O3		MACC reanalysis & CAMS NRT, various versions	MACC reanalysis & CAMS NRT, various versions	CAMS reanalysis* & IFS NWP (various versions) in McClear v3.5	CAMS reanalysis* & IFS NWP (various versions) in McClear v3.6 which considers a new species of aerosol introduced in the IFS CY48r1 suite of CAMS
Bias correction		Empirical multiplication factor	Re-trained bias correction	No bias correction	No bias correction
Coverage		MSG FOV	MSG FOV	MSG FOV	MSG/Himawari FOV

* For CRS v4.5 and 4.6, CAMS reanalysis is used for times series within 2004 and 2020. After 2020, McClear v3.5 or v3.6 with different IFS inputs are used.

implemented for the comparison with ground data, the results are provided mainly for GHI only, and their timescales may also differ from our statistics. Some are only offering daily or monthly average evaluations. For an evenhanded comparison of our results with the previous works, we will mainly allude to the analogical evaluations with ground measurements specifically for the regions and/or networks, the clear-cloudy distinction cases and the temporal resolution of the derived statistics as used in our assessment.

4.1. *All-sky validation*

Table 3 and Fig. 6 summarize the relative biases (rMBE) and relative root mean square error (rRMSE) for GHI and BNI respectively for all stations for an all-sky validation. The stations are ordered in terms of increasing satellite viewing angle (vza) inside the regions. The observations and corresponding CRS time series under all-sky conditions were jointly resampled 2000 times using a non-parametric bootstrap approach (with replacement), allowing the performance metrics to be recomputed for each bootstrap sample. Uncertainty bounds were estimated using the 95% confidence intervals (CI) of the rMBE and rRMSE bootstrap distributions, derived from the 2.5th and 97.5th percentiles.

Overall, the rMBE is predominantly positive for both GHI and BNI for most stations, generally in continental and coastal regions, indicating an overestimation of irradiance by the satellite retrieval. Particularly, for BNI larger overestimation may originate mostly from cases with a close to zero value in the ground-based observation while the satellite estimate is above zero. This can be attributed to the systematic error associated to the pinpoint deviation when comparing several km-sized satellite pixels with the signal of square-cm sized ground observations which results in deviations especially in broken cloud conditions. This plausibility can be further investigated by performing the analysis for different sky conditions (as in Section 4.3). In general, the negative biases appear for the locations with vza higher than 60° which can be associated to the geometrical effects as cloud parallax that is currently not corrected in the retrieval. At large satellite viewing zenith angles (vza $\gtrsim$ 60°), if the displaced cloud signal is interpreted as being located above the site, the retrieval may assume stronger cloud attenuation than actually occurs, leading to an underestimation of the surface irradiance and therefore a negative bias in the SSI retrieval. The magnitude of this effect increases with the cloud height. The negative bias observed at some coastal locations with viewing zenith angles below 60° likely originates from a combination of sub-pixel land-sea heterogeneity, surface reflectance variations, and heterogeneous cloud fields within the satellite pixel.

For all-sky GHI evaluations done on the hourly scale, the MBE without the station COC ranges between −32.3 to 27.3 W/m^2 with a mean of 3.5 W/m^2. For the same stations, RMSE of GHI is between 50.6 and 127.4 W/m^2 with a mean of 77.1 W/m^2. GHI's rMBE ranges between −7.4 and 4.9% and the mean values of all stations is 0.65% excluding the COC station. For the same set of stations, rRMSE of GHI is between 8 and 30% with a mean value of 16.5%. The COC site is excluded as it is located at a very small island with about 500-m wide bow-shaped archipelago land area with shallow water inside it and is characterized by a sub-scale mixed pixel with high uncertainty in surface albedo that may be further amplified due to the dynamic water surface conditions transporting sediments to the surface or showing sea spray depending on wind conditions and water surface roughness. Other stations on small islands as LYU, MNM and KWA also show increased error metrics, but are not excluded from the assessment as their local conditions are not so special as COC. For GHI, the MBE (rMBE) for COC is −64.9 W/m^2 (−12.2%) and RMSE (rRMSE) as 118 W/m^2 (22.2%). In case of BNI, rMBE for COC is −33.6% and the rRMSE is 58.6%. Therefore, the station COC is an outlier with largest deviations for GHI and BNI. Most studies cited above did not include the COC station due to this non-representativeness of the pixel. Yu et al. (2019) and Li et al. (2023) used this site and reported negative biases as −46.7 and − 60.8 W/m^2 and RMSE as 134.1 and 141.7 W/m^2 for GHI and BNI at 10 min resolution, respectively. Further investigations and their physical interpretations regarding the CRS retrieval performance in the island regions including COC is presented in Appendix B.

The previous relevant studies for Himawari FOV are discussed in Table 4. Some of the published studies for Himawari FOV used SSI data with bias correction as Bright (2019), Qin et al. (2021) and ABoM evaluation of their SSI products ABoM (2022). CRS applies no ground observation-based adaptations anymore. It fully relies on a physical retrieval only. Compared to validation studies against datasets without applying any bias corrections, CRS hourly GHI biases are in the same order or smaller, even if relying on different stations and periods. The hourly RMSEs for CRS GHI are in general smaller than the respective RMSE estimates found in other studies.

CRS evaluation results show for all-sky BNI in hourly resolution MBE values without COC in the range − 83.3 and 78.1 W/m^2 with a mean of

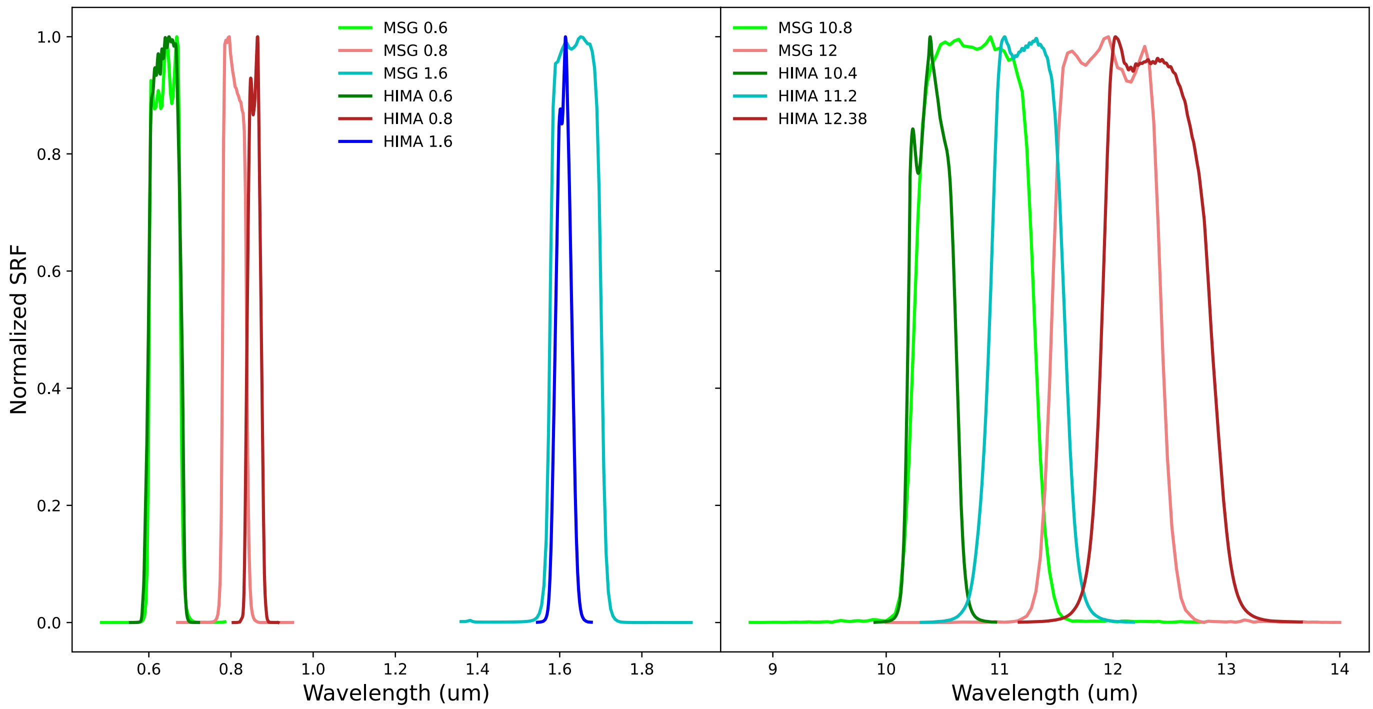

Fig. 4. Normalized Spectral Response Functions (SRFs) of the MSG and Himawari channels exploited in the APOLLO_NG cloud retrieval.

23.5 W/m^2. For the same stations, the RMSE of BNI is between 102.9 and 195 W/m^2 having a mean of 137.8 W/m^2. The MBE and RMSE for the COC station are −136 and 237.5 W/m^2. rMBE values (without COC station) are found between −26.6 and 15.3% with a mean of 4.6% and the rRMSE values are between 18 and 64.1% with a mean value of 34.5%.

Only very few previous studies report on BNI validation. For their all sky hourly BNI for 11 BSRN sites and after applying bias correction, Qin et al. (2021) report MBE between −2.6 and 11.4 W/m^2 with a mean of 3.5 W/m^2 and the RMSE between 101.4 and 152.4 W/m^2 with a mean as 121.1 W/m^2. ABoM (ABoM, 2022) provides results only for 10 min temporal resolution not used in our study. Valor et al. (2023) evaluated BNI against 6 BSRN stations obtaining BNI hourly MBE in the range of −198 and 139 W/m^2 having mean as −9 W/m^2 and RMSE between 327 and 372 W/m^2 and a mean of 347 W/m^2 where their RMSE are based on medians.

Our SSI comparison to other studies is restricted as they deal with different data periods and set of stations. Nonetheless, the assessment for the all-sky irradiance reveals that CRS v4.6 does not require any general bias correction as needed previously in earlier CRS versions. In future, a localized bias correction with locally available ground observation is nevertheless helpful to treat location-specific effects at places where the satellite pixel is not very representative for the ground instrument location as in e.g. coastal areas and islands and with COC as example of such a station included in this study. This is also the well-known requirement of site adaptations e.g. in the siting assessment for solar energy systems (Polo et al., 2016; Salamalikis et al., 2022).

Irrespective of the sub-hourly or hourly statistics presented in the literature mentioned above, most of the studies using ASP data in their evaluation report negative MBE for this site with the exception of Yu et al. (2019) and ABoM (2022). ASP is located within a desert region. The negative bias is indicative of the possible failure of these methods for the desert surface with high albedo and potential aerosols presence. CRS v4.6 perform well in this case and shows a smaller bias compared to other studies.

4.2. CRS cloud-free and cloud type validation

To further investigate the origin of the biases identified in the all-sky evaluation, the analysis is refined by separating the retrieval performance according to cloud type derived from the APOLLO_NG cloud retrieval. As sky conditions typically evolve on a shorter time scale, the cloud-free and cloud type assessment is therefore performed on the 1 min scale of the CRS.

Fig. 7 displays the relative bias and the relative RMSE of 1-min resolved GHI and BNI for each station for the cloud types resulting of APOLLO_NG cloud mask with the cloud probability threshold being set to 1% selecting all minutes in the CRS 1 min output. Three cloud categories are considered. Events detected as clear by APOLLO_NG are referred to as cloud-free conditions. The optically thick cloud category aggregates instances classified as low, medium, and high optically thick clouds (cloud types 5–7), while the optically thin cloud category corresponds to cloud type 8, representing thin cirrus. Within each region, the stations are ordered according to increasing vza.

For cloud-free conditions, CRS shows a small positive bias for both GHI and BNI across most regions with the exception of the mountain station, where a slight negative bias appears. This deviation may be related to differences between the coarse-resolution atmospheric inputs used in the McClear clear-sky model and the actual high-elevation station conditions, as well as topographic shading and local surface albedo variability.

For optically thick clouds, the bias pattern shows larger variability over stations and regions. Such mixed behavior is expected because this category includes clouds with a broad range of optical depths and spatial structures. As already seen in the all-sky results, stations with vza greater than about 60° tend to exhibit negative biases, indicating that retrieval uncertainties associated with viewing geometry and cloud optical property estimation become more pronounced at large satellite viewing angles.

For optically thin clouds, the bias is mostly positive for stations with vza below 60°, suggesting a slight overestimation of irradiance when thin cirrus are present. For vza $\geq$ 60°, the bias tends to become negative

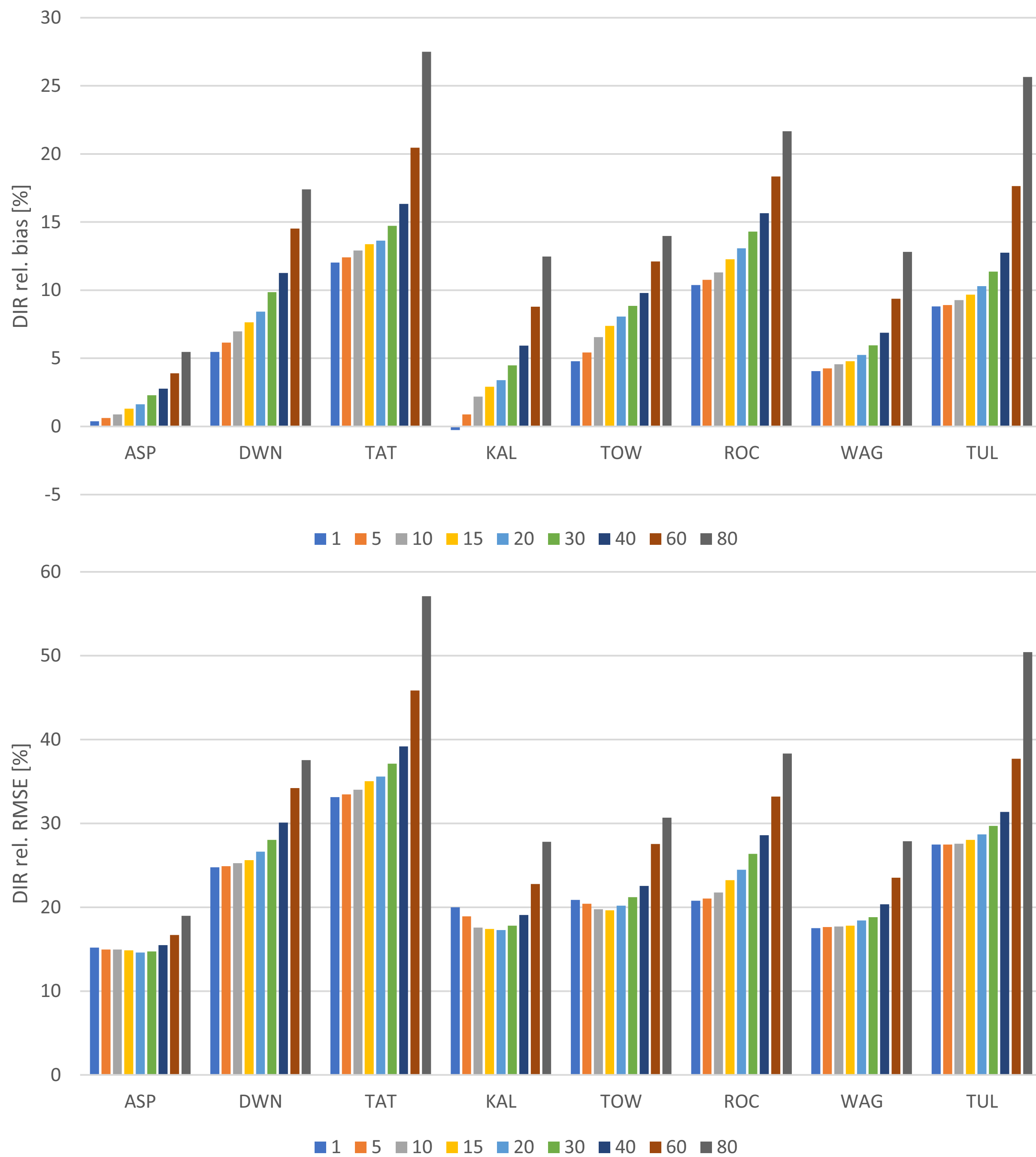

Fig. 5. Relative bias and RMSE for hourly direct horizontal irradiance (obtained from BNI) irradiation as function of the Cloud Probability Threshold (CPT) selected to switch from the cloud-free to the all-sky module in Heliosat-4.

as also observed for the thick cloud case but with a slightly smaller magnitude.

The relative RMSE is smallest under clear-sky conditions and largest for optically thick cloud cases, which may include situations dominated by broken cloud fields. The observed bias patterns likely result from a combination of viewing geometry effects and surface and cloud heterogeneity, whose individual contributions cannot be separated using the all-sky and cloud-type assessments presented so far. Nevertheless, this analysis already reveals clear dependencies of the retrieval performance on viewing zenith angle and cloud regime, with larger bias deviations occurring at vza $\geq 60^{\circ}$ and under more heterogeneous cloud conditions. To further investigate these effects, irradiance variability classes derived from 1 min observations are analysed in the following section.

The cloud-free 1 min time scale GHI rMBE ranges between -3.6 and 7.4% with a mean of 3.7% and the rRMSE is observed in the range of 98.5 and 21.4% with a mean as 15.4% without including the LYU site which appear to be the largest outlier here with rMBE and rRMSE as 17.6 and 42.4%. LYU is situated at a small island of around 1 km width. For COC, the rMBE and rRMSE are 2.8 and 18.5% respectively. For our evaluation done on the 1 min resolution, the cloud-free GHI MBE are found between -28.7 and 39.9 W/m^2 with a mean of 22 W/m^2 and 56.2 to 137.0 W/m^2 for RMSE having a mean of 93.5 W/m^2 without LYU for which the bias and RMSE are 80.2 and 192.8 W/m^2 respectively. The location COC has a MBE of 20 and RMSE value of 130.5 W/m^2.

Only a few studies show the SSI evaluation against the ground measurements for different sky conditions. Yu et al., 2019 and Letu et al., 2023 perform the retrieval on 10 min resolution and carried out

Table 3
GHI and BNI bias (MBE), relative bias (rMBE), RMSE and rRMSE for all-sky, hourly temporal resolution for 2016-2025 in desert (orange), continental (green) and coastal/subpixel (blue) and mountainous (brown) regions.

Station	Irradiance	MBE (W/m²)	rMBE (%) [CI 95%]	RMSE (W/m²)	rRMSE (%) [CI 95%]
ASP	GHI	12.1	2.0 (1.8 – 2.1)	57.5	9.5 (9.2 – 9.8)
	BNI	45.3	6.3 (6.1 – 6.6)	128.6	18.0 (17.6 – 18.4)
KAL	GHI	9	1.6 (1.4 – 1.8)	67.6	12.1 (11.7 – 12.5)
	BNI	33.9	5.3 (4.9 – 5.7)	148.1	23.0 (22.6 – 23.5)
DWN	GHI	23	4.2 (3.9 – 4.4)	95.5	17.4 (17.0 – 17.8)
	BNI	46.9	9.2 (8.7 – 9.6)	151.8	29.7 (29.1 – 30.1)
ROC	GHI	23.8	4.4 (4.2 – 4.6)	79	14.6 (14.3 – 14.9)
	BNI	78.1	14.3 (13.9 – 14.6)	153.1	28.0 (27.5 – 28.4)
SON	GHI	19.3	3.6 (3.2 – 3.9)	86.2	15.9 (15.4 – 16.4)
	BNI	34.4	7.7 (7.1 – 8.3)	123	27.6 (26.9 – 28.4)
NEW	GHI	3.2	0.6 (0.3 – 1.0)	81.5	16.2 (15.6 – 16.7)
	BNI	62.8	12.7 (12.1 – 13.2)	147.4	29.7 (28.9 – 30.5)
WAG	GHI	21.6	4.4 (4.2 – 4.6)	64.2	13.0 (12.7 – 13.3)
	BNI	71	13.4 (13.0 – 13.7)	141.3	26.6 (26.1 – 27.0)
TAT	GHI	17.2	4.4 (4.2 – 4.6)	60.4	15.5 (15.2 – 15.7)
	BNI	34.8	10.0 (9.7 – 10.3)	112	32.1 (31.6 – 32.6)
TUL	GHI	12.9	3.0 (2.8 – 3.3)	72.3	16.9 (16.6 – 17.3)
	BNI	60.8	15.3 (14.8 – 15.8)	138.8	35.0 (34.4 – 35.5)
QIQ	GHI	5.7	1.4 (1.0 – 1.9)	54.6	13.7 (13.0 – 14.4)
	BNI	11.2	2.4 (1.5 – 3.5)	127.1	27.6 (26.4 – 28.8)
LAU	GHI	0.7	0.2 (-0.3 – 0.7)	107.6	26.6 (25.9 – 27.4)
	BNI	22.9	5.4 (4.6 – 6.2)	184.2	43.4 (42.4 – 44.4)
HOW	GHI	-12.3	-3.1 (-3.7 – -2.5)	88.9	22.3 (21.4 – 23.1)
	BNI	-38.7	-15.9 (-17.1 – -14.8)	102.9	42.2 (41.0 – 43.5)
TIR	GHI	-31	-6.2 (-6.6 – -5.7)	101.8	20.3 (19.7 – 20.9)
	BNI	-23	-10.1 (-11.9 – -8.5)	128.1	56.6 (54.9 – 58.3)
GUR	GHI	-32.3	-7.4 (-8.2 – -6.7)	101	23.3 (22.5 – 24.0)
	BNI	-83.3	-26.6 (-28.0 – -25.2)	150.5	48.1 (46.8 – 49.5)
TOW	GHI	27.3	4.8 (4.6 – 5.0)	71.2	12.6 (12.2 – 12.9)
	BNI	77.7	13.8 (13.4 – 14.2)	149.5	26.5 (26.0 – 27.0)
BRO	GHI	15.5	2.6 (2.4 – 2.7)	58.9	9.7 (9.5 – 10.0)
	BNI	43.5	6.5 (6.2 – 6.7)	136	20.2 (19.8 – 20.6)
MNM	GHI	-1.7	-0.3 (-0.4 – -0.2)	60.4	11.5 (11.3 – 11.7)
	BNI	3	0.6 (0.4 – 0.9)	123.8	25.0 (24.8 – 25.3)
KWA	GHI	-29.3	-5.1 (-5.5 – -4.7)	90.3	15.6 (15.1 – 16.1)
	BNI	-74.4	-16.1 (-17.4 – -14.8)	175.9	38.0 (36.8 – 39.2)
LYU	GHI	-9.2	-2.5 (-2.9 – -2.1)	109.6	30.0 (29.6 – 30.5)
	BNI	-6.3	-3.3 (-4.4 – -2.2)	122.3	64.1 (62.8 – 65.3)
ISH	GHI	8.4	2.0 (1.8 – 2.2)	73.7	17.6 (17.3 – 17.8)
	BNI	44.5	14.9 (14.5 – 15.3)	126.9	42.5 (42.0 – 43.1)
LEA	GHI	4.3	0.7 (0.5 – 0.8)	50.6	8.0 (7.7 – 8.3)
	BNI	-14.6	-1.9 (-2.3 – -1.6)	145.8	19.2 (18.8 – 19.5)
FUA	GHI	18.9	4.9 (4.8 – 5.1)	61.6	16.0 (15.8 – 16.3)
	BNI	37.5	12.0 (11.6 – 12.3)	105.5	33.8 (33.3 – 34.3)
CEH	GHI	12.6	2.5 (2.1 – 2.8)	82.6	16.2 (15.7 – 16.6)
	BNI	52.2	14.3 (13.5 – 15.0)	131.7	36.0 (35.2 – 36.8)
ADE	GHI	15.6	3.2 (3.1 – 3.4)	54.8	11.4 (11.2 – 11.6)
	BNI	71.5	14.4 (14.1 – 14.8)	135.2	27.3 (26.8 – 27.8)
TRI	GHI	4.6	0.9 (0.5 – 1.3)	83.3	16.0 (15.6 – 16.5)
	BNI	36.7	10.0 (9.2 – 10.7)	125.9	34.2 (33.4 – 34.9)
GER	GHI	0.3	0.0 (-0.1 – 0.2)	60.5	10.4 (10.1 – 10.7)
	BNI	12.7	2.0 (1.6 – 2.4)	144.2	22.8 (22.3 – 23.3)
CAP	GHI	-9.6	-2.4 (-2.6 – -2.2)	61.6	15.2 (14.9 – 15.6)
	BNI	14.4	4.4 (3.8 – 5.1)	126.4	38.9 (38.2 – 39.5)
SAP	GHI	-2.6	-0.8 (-1.1 – -0.4)	79	22.5 (22.1 – 23.0)
	BNI	26.7	9.4 (8.5 – 10.2)	157.3	55.3 (54.2 – 56.4)
ABS	GHI	9.9	2.8 (2.5 – 3.0)	60.6	16.8 (16.5 – 17.2)
	BNI	25.5	8.1 (7.5 – 8.7)	126.2	40.1 (39.0 – 41.1)
COC	GHI	-64.9	-12.2 (-12.5 – -11.9)	118.2	22.2 (21.9 – 22.5)
	BNI	-136	-33.6 (-34.4 – -32.8)	237.5	58.6 (57.9 – 59.3)
FEN	GHI	-9	-2.1 (-2.5 – -1.7)	84.9	19.3 (18.8 – 19.9)
	BNI	-5.5	-1.9 (-2.6 – -1.1)	106.8	36.6 (35.6 – 37.5)
YUS	GHI	-19.9	-4.0 (-4.4 – -3.6)	127.4	25.5 (25.1 – 26.0)
	BNI	26.8	5.8 (5.1 – 6.5)	195.6	42.6 (41.7 – 43.5)

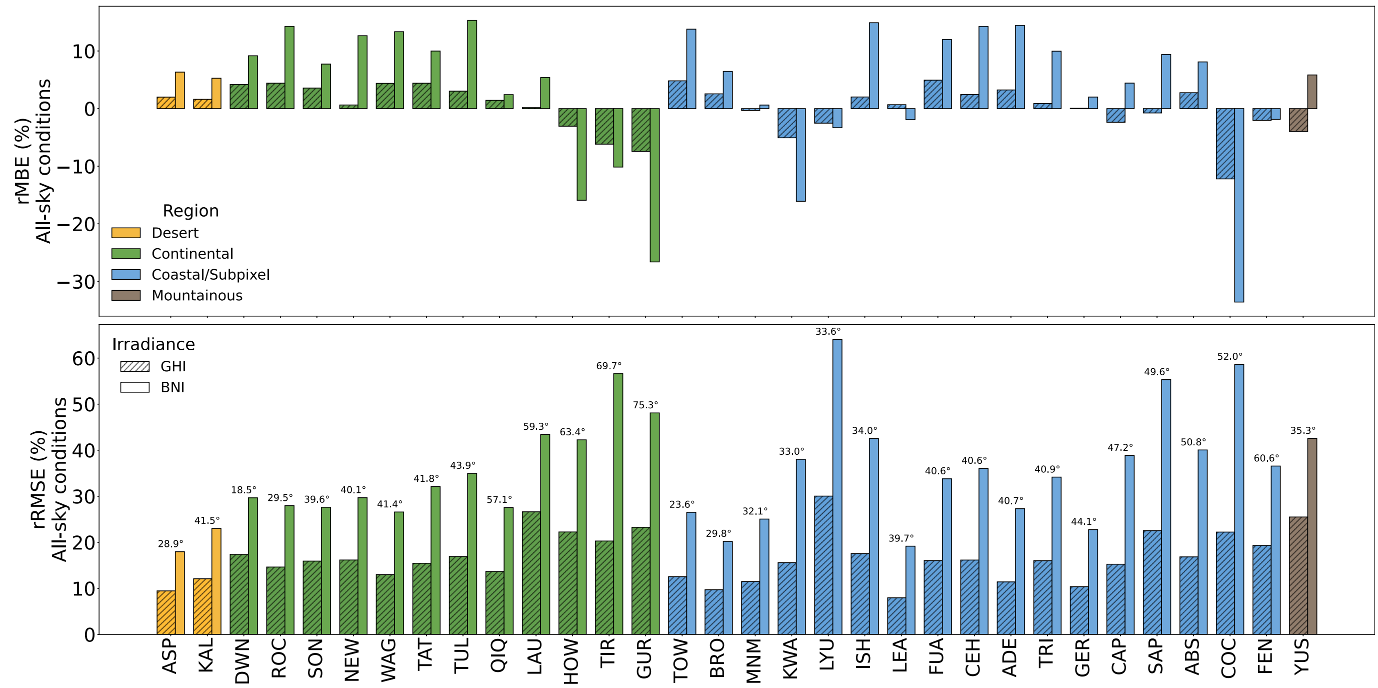

Fig. 6. Relative MBE (upper plot) and relative RMSE (lower plot) for hourly all-sky GHI and BNI in different geographical regions as desert (orange), continental (green) and coastal/subpixel (blue) and mountainous (brown) regions. The stations are ordered in each group in terms of increasing vza.

Table 4
Summary of previously published relevant studies on SSI within the Himawari FOV.

Published studies	Product specification and period	Ground observations	MBE (W/m^2)	RMSE (W/m^2)
Bright (2019)*	SOLCAST commercial database with diverse time periods	ASP, DAR, DWN, FUA, ISH, NEW, SAP, GUR, TIR, HOW, LAU and TAT	−13.2–23.2	53.1–100.5
Qin et al. (2021)*	July 2016–April 2019	11 ABoM sites	−2.8–9.2	48.5–79.1
ABoM (2022)*	ABoM archive data 2017	13 ABoM stations	2.7	48.5
Damiani et al. (2018)	AMATERASS SSI data retrieved for Japan with 1 km and 2.5 min resolution	4 SKYNET observations	20.4–31.3 (including RE) 31.4–51.6 (excluding RE)	70.7–95 (including RE) 73.0–104.7 (excluding RE)
Ma et al. (2020)	Spatial resolution of 5 km for the year 2016	13 stations from ABoM and BSRN	7.3 (at 9 ABoM sites) and 16.9 (at 4 BSRN stations)	89.8 (at 9 ABoM sites) and 79.2 (at 4 BSRN stations)
Letu et al. (2020)	5 km for the year 2016, excluding Jan., Feb., and July	112 stations: 89 from CMA, 1 from AERONET, 9 from ABoM, 6 from BSRN, 1 from ESRL_GMD, and 16 from GTMBA network	9.5 (average excluding CMA stations)	81.1 (average excluding CMA stations)
Letu et al. (2022)	0.05° spatial resolution for the year 2016	27 sites from ABoM BSRN, GTMBA, and CMA networks	3.3	104.9
Letu et al. (2023)	0.05° spatial resolution for 2016–2019	8 BSRN stations and 1 at Xianghe site	5.8	72.9
Li et al. (2023)	Spatial resolution of 5 km for the year 2017	10 BSRN stations (including COC)	−14.1	82.4
Valor et al. (2023)**	Spatial resolution of 0.01° for the year 2016	6 BSRN stations	−61–30	137–179

Aerosol Robotic Network (AERONET), Chinese Meteorological Administration (CMA), Earth System Research Laboratory Global Monitoring Division (ESRL_GMD).
* SSI datasets including bias correction.
** For Valor et al. (2023) RMSE computation is based on median.

the comparison on this instantaneous resolution with collocated ground-based measurements.

The station-wise comparison of the 10 min cloud-free GHI by Yu et al., 2019 for 15 BSRN and ABoM sites resulted in MBE between 3.6 and 40.0 W/m^2 and RMSE in the range 33 and 84 W/m^2 excluding the COC island for which they obtained the MBE and RMSE as −45.1 and 92 W/m^2 respectively. Letu et al., 2023, for their cloud-free SSI product evaluation against 8 BSRN and 1 Xianghe station at 10 min scale obtained the MBE and RMSE as 14.3 and 73.3 for snow/ice free surface and 21.4 and 68.5 W/m^2 for snow/ice on ground in spring, 23.7 and 83.5 W/

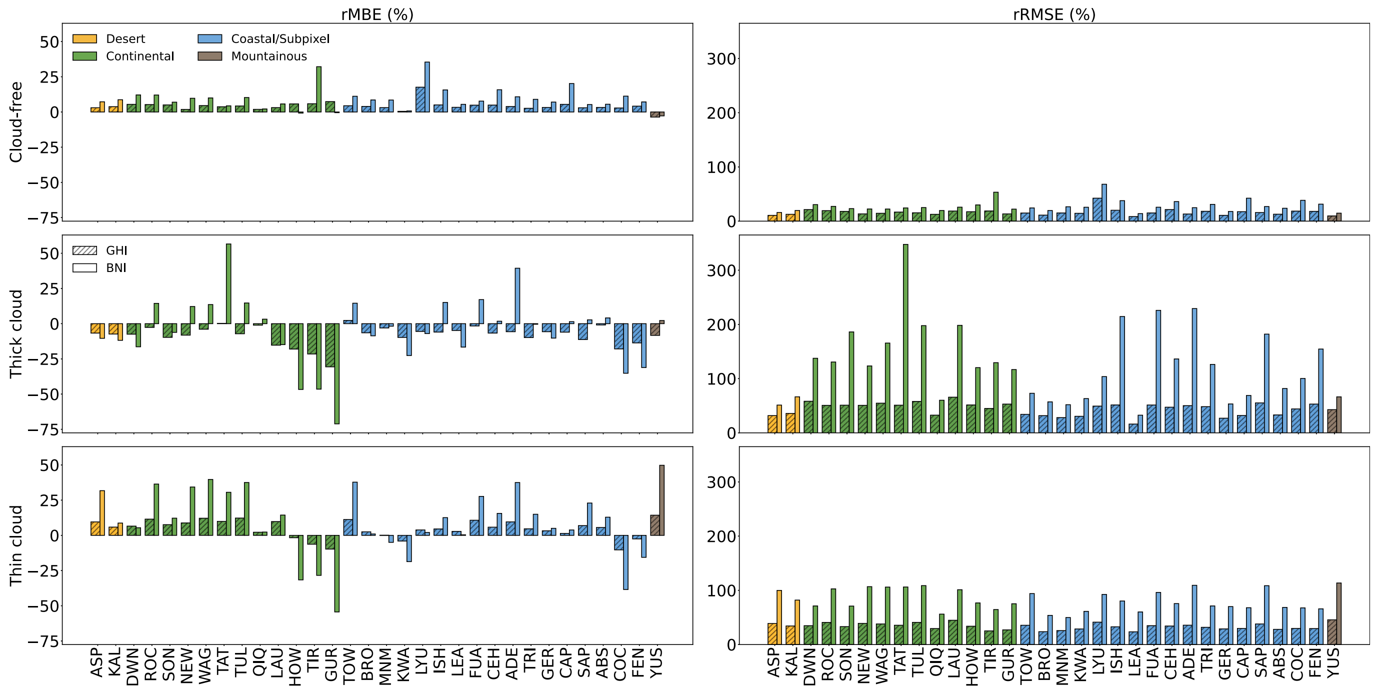

Fig. 7. Relative bias (left) and relative RMSE (right) for instantaneous (minute scale) GHI and BNI grouping the cases according to cloud type derived from the APOLLO_NG cloud retrieval with a 1% cloud probability threshold. Results are provided for different classes of regions as desert (orange), continental (green) and coastal/subpixel (blue) and mountainous (brown) regions. The stations are ordered in each group in terms of increasing vza.

m^2 for snow/ice free surface in summer, 39.6 and 98.7 W/m^2 for snow/ice free surface in fall and 28.3 and 96.1 W/m^2 for the snow/ice free events and 23.1 and 51.9 W/m^2 for the ground with snow/ice in the winter seasons respectively.

GHI cloud-free biases in our analyses are comparable to those found in the two studies comparing 10 min GHI estimates i.e. Yu et al., 2019 and Letu et al. (2023) whereas the range of the RMSE is smaller as expected for a 10 min dataset due to temporal averaging effects.

For cloud-free 1 min BNI values, rMBE is between −2.8–32.2% with a mean of 8.6% and rRMSE is lying in the range 13.9–53.4% with a mean value of 26.5% excluding the LYU that again shows large values of rMBE and rRMSE as an island site. For COC the rMBE is 14.9 and the rRMSE is 49.0%. The mean MBE and the mean RMSE for the 1 min clear sky BNI are 85.7 and 200 W/m^2 respectively.

The cloud-free GHI and BNI relative biases are low across all regions and all stations showing slight overestimation. Visual assessment of BNI timeseries reveals that a majority of these situations are found during cloud-free days when the cloud masking performs very well. Therefore, this positive bias can be mainly attributed to aerosol and water vapor estimates. Such deviations are constantly monitored by the CRS team with an even stricter case screening based on the temporal variability of the ground observation itself.

The 1 min resolved GHI's rMBE and rRMSE for the optically thick clouds (type 5, 6, and 7) are between −30.6–2.3% and 16.2–65.8% respectively with the mean of rMBE as −7.8% and rRMSE as 44.3% excluding COC island. For the optically thin clouds, the rMBE and rRMSE are in the range − 9.7–14.3% and 23.5–45.6% respectively with the mean rMBE as 5.2 and the mean rRMSE as 33.6%. 1 min GHI statistics for the optically thick clouds without the COC site reveal the mean of MBE and RMSE as −27.7 and 151.5 W/m^2 respectively and these metrics for the optically thin clouds as 22.6 and 158.3 W/m^2.

For 1 min resolved BNI, rMBE and rRMSE for the optically thick clouds are between −71.1–56.6% and 32.6–347.6% respectively showing mean of rMBE as −3.5% and mean rRMSE of 127.5% without COC station. Here the GUR station shows exceptionally large negative rMBE of −71%. For the optically thin clouds, rMBE and rRMSE are in the ranges −54.4–49.8% and 49.8–113.6% respectively with mean rMBE as 11.1% and the mean rRMSE as 82.8%. For the optically thin clouds, again GUR location shows a large negative rMBE here with the value −54.4%. The 1 min resolved mean MBE and RMSE for the stations without COC are −14.6 and 194 W/m^2 for optically thick clouds and are 31.7 and 265 W/m^2 for optically thin clouds respectively.

Limited studies split the results into cloud conditions and for a high temporal resolution. In their SSI product evaluation against 8 BSRN and 1 Xianghe station at 10 min scale, Letu et al., 2023 showed the statistics by splitting the cloudy sky data into water and ice phase clouds. For water clouds, they obtained the MBE and RMSE as −3.6 and 130.2 for snow/ice free surface and − 32.6 and 142.0 W/m^2 for snow/ice ground in spring, −0.3 and 126.3 W/m^2 for snow/ice free surface in summer, 7.2 and 133.7 for snow/ice free surface in fall and − 0.3 and 133.3 for the snow/ice free events and − 50 and 104.3 for the ground with snow/ice in the winter seasons respectively. In case of ice clouds, they obtained the MBE and RMSE as 9.5 and 94.2 for snow/ice free surface and − 45.0 and 141.6 W/m^2 for snow/ice on ground in spring, 15.1 and 112.6 W/m^2 for snow/ice free surface in summer, 23.3 and 114.7 for snow/ice free surface in fall and 3.5 and 127.9 for the snow/ice free events and 8.1 and 56.0 for the ground with snow/ice in the winter seasons respectively. Considering the classification of water clouds and ice clouds in Letu et al., 2023 being approximately representative of the optically thick clouds and thin cloud respectively in our study, it can be observed that, in general, the direction of the GHI bias is mostly negative for the water (thick) clouds and have a positive trend for the optically thin clouds in both studies.

4.3. Variability class dependent validation

The solar irradiance transmitting through the atmosphere undergoes extinction by various atmospheric constituents such as clouds, aerosols, water vapor and ozone. The spatiotemporal scales of the SSI variability due to clouds range widely with the lowest as small as second or meters, e.g. cloud shading or cloud enhancement in partly cloudy situations (Mol and van Heerwaarden, 2025). Because of this strong variability, evaluating SSI retrieval performance solely through aggregated statistical metrics can obscure the physical processes responsible for retrieval errors. A useful approach to better understand the limitations of satellite-based irradiance retrieval models is to analyze their performance under different sky regimes. The variability-based diagnostics provide guidance for identifying atmospheric regimes where retrieval parameterizations may require improvement. The classification of sky conditions therefore plays an important role in solar energy applications, including power forecasting, nowcasting, synthetic irradiance generation for solar energy system assessment, and irradiance decomposition models (McCandless et al., 2016; Carreno et al., 2020; Rayati et al., 2021; Schreck et al., 2020; Riihimaki et al., 2021; Schaible et al., 2024; Lopez et al., 2024). Pérez-Ortiz et al. (2016) and Hartmann (2020) provide an overview of different methods applied to classify the state of the sky. To our knowledge, the usage of the variability classes solely based on GHI minute observations as a diagnostic framework for evaluating Himawari satellite-based SSI retrievals has not been previously explored.

We evaluate the CRS results using a GHI-based variability classification method as described in de Miranda et al. (2026). The authors extended the previous BNI classification method from Schroedter-Homscheidt et al. (2018) to use only GHI measurements, which are more widely available than BNI due to the high costs of tracker systems. This previous BNI method has been widely used e.g. in timeseries generation for solar energy applications (Schreck et al., 2020) or in nowcast model development and evaluation (Nouri et al., 2023; Schaible et al., 2024). Separation into different cloud conditions based on irradiance variability can help to understand and identify the limitations on the irradiance retrievals related to each sky condition without the need for an auxiliary retrieval of aerosol or cloud conditions with their own specific uncertainties.

The new GHI classification method proposed by de Miranda et al. (2026) is based on a reference database of 277 1 min GHI observations from the Carpentras BSRN station, manually classified into eight variability classes, considering different sky conditions dominated either by aerosols or various cloud types. The algorithm computes 13 variability indices (VIs) from 1 min GHI observations and its clear sky component (from the McClear model) and applies a three-step decision process: discriminant filter, probability-based classification, and median distance-based approach. The first two steps classify samples inside the variability indices reference database domain, while the last step addresses outliers caused by sunrise/sunset, specific climate conditions, or clear sky model inaccuracies. Therefore, the method is based on a comparison of the variability indices computed for a new dataset with the ones from the reference database, which was manually classified forming a ground truth for sky conditions classification.

The method defines eight variability classes, which includes different cloud types – such as cumulus, stratus, cirrus, and others – that can differ in thickness, altitude, and optical properties, direct influencing the amount of solar irradiance they transmit or reflect. Associating these variability classes with their corresponding cloud types enables an assessment of how varying sky conditions affect SSI models. Satellite imagery from the APOLLO-NG cloud retrieval algorithm (based on MSG) and MODIS RGB True Colors composites were used to visually associate the variability classes with the more common cloud types and conditions in the Carpentras reference database. Typical examples are shown in Appendix C.

Classes 1 is associated with clear sky condition. Class 2 corresponds to a nearly clear-sky which could be impacted by aerosols, thin cirrus or sub-visible convective clouds. Class 3 typically exhibits spatially heterogenous cirrus conditions or very small cumulus clouds. Class 4 mainly registers visible and sub-visible cumulus clouds. Class 5 lies in-between optically thin and thick clouds and often shows mixed characteristics, usually a thick heterogenous cirrus with higher optical thickness than in class 3 dominate this class. Classes 6–8 mainly constitute optically thick clouds. Class 6 is characterized often by multilayer clouds having lower broken clouds with cirrus fields above them, typically causing also cloud-induced enhancements in irradiances. Class 7 also usually contains multilayer clouds but with larger optical thickness compared to class 6. Class 8 signifies close to or complete overcast situation comprising single-layer or multilayer stratus that may have an upper non-stratus cirrus filed layer. This classification adds further detail in assessment compared to cloud/cloud-free or cloud type discriminations used in previous sections.

Fig. 8 shows the distribution of the hourly sky conditions based on the 1 min GHI classification for all stations for the whole time period used in our assessment. The stations are ordered according to increasing average GHI from the ground measurements. The stations LEA, ASP, BRO and GER are observed to have approximately 73, 62, 59 and 50% clear and nearly clear sky instances (i.e. combination of classes 1 and 2) respectively. ASP, BRO and LEA are marked with least amount of optically thick broken cloud (i.e. combination of classes 6 and 7) cases lying in the range of 9–13% whereas the highest number of these incidences are observed for LYU as about 49%. The sites ABS, FUA, ISH, LAU, SAP, TAT and LYU have highest overcast incidences ranging between 25 and 33%.

Fig. 9 shows the spread of the RMSE values across the variability classes against the mean of the GHI for each class per station. It can be observed that for the clear and close to clear classes i.e. 1 & 2, the spread in RMSEs is low, with the exception of one outlier with around 120 W/m^2 from BSRN-KWA station. This station has a very low percentage of clear and close to clear cases (7.1% for class 1 and 2). The highest spread is observed for class 4 and 6 i.e. broken cloud cases. This scatterplot also shows that the errors in partly and fully overcast conditions (classes 7 and 8) have a lower RMSE on average as compared to the broken cloud cases, but they also exhibit the lowest mean irradiance value. For relative RMSE, this will create larger values in overcast cases than the broken clouds due to low irradiance values. Therefore, the variability classes results are analysed with MBE and RMSE in W/m^2.

Figs. 10 and 11 illustrate the biases and RMSE respectively for the hourly GHI and BNI data under each class. SSI estimation and prediction models are known to perform better in clear sky compared to cloudy sky. In our variability based GHI and BNI evaluation, the deviations for GHI and BNI are also found to be lowest for the clear and almost clear cases and increase with cloudiness till class 7. The class 8 with more homogeneous cloud coverage shows relatively smaller biases compared to other optically thick classes (4–7). The MBE for GHI and BNI are in general positive for the desert and continental category in all classes for most of the stations with the exception of the locations close to the edge of the satellite field of view, where the biases increase with increasing vza. Coastal stations with the possibility of having land/water mixed pixels exhibit mixed deviations for the clear sky and the classes 3–6.

For class 1, the MBE values are smallest and the RMSE are minimal indicating best agreement with the ground measurements. This behavior reflects the stable atmospheric conditions and the absence of clouds, under which the assumptions used in the radiative transfer modeling are largely fulfilled. The positive MBE observed at most desert and continental stations indicates a slight overestimation of irradiance by the retrieval, which may arise from minor uncertainties in aerosol representation or surface reflectance assumptions. For the coastal regions, the result depends upon how the land sea mask interprets the surface underneath. If the land-sea mask assumes the satellite pixel to be an ocean pixel, the shallow water and land will be too bright and will be interpreted as a cloud cover. This can create a negative bias, primarily caused by non-detected cloud-free situations. This especially is likely in areas with a large tidal hub height. If the land-sea mask assumptions hold for the correct detection (land pixel) which are dominated either by land or shallow waters with higher albedo than the ocean, large negative biases are not expected as very dominant result and also not observed in mixed pixel conditions (with exception of KWA and COC). Further analysis of the CRS results in the islands stations of COC, MNM, and KWA are discussed in Appendix B.

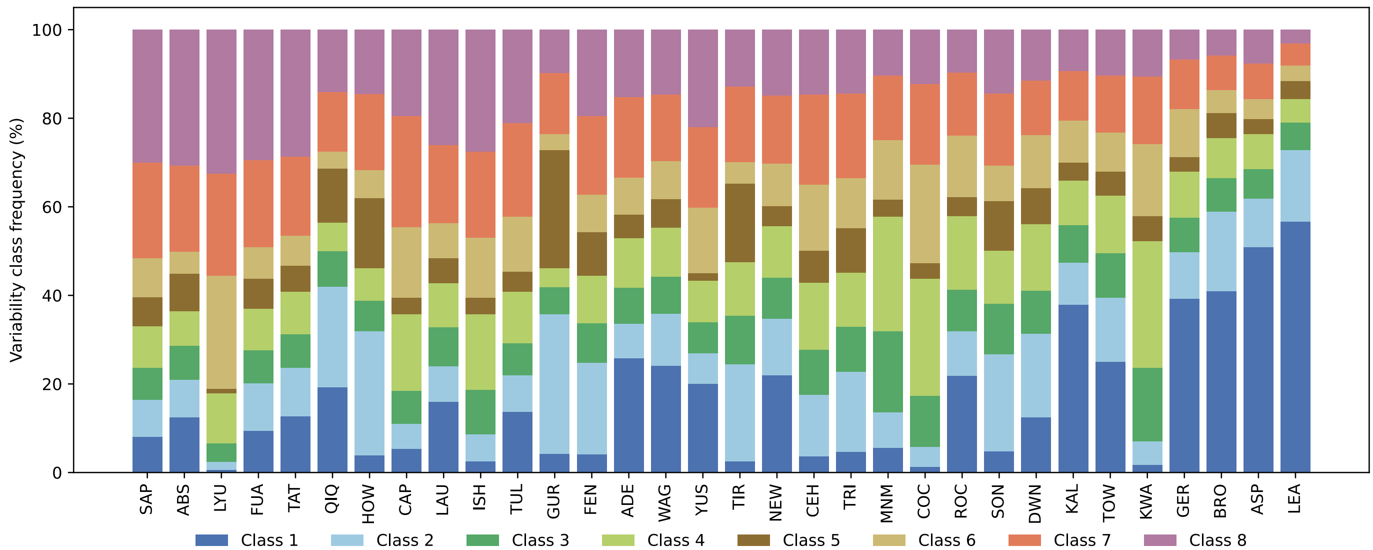

Fig. 8. Percentage distribution of the sky conditions based on the 1 min GHI data for the stations used in this study. Stations are ordered with increasing average GHI measured at the ground stations.

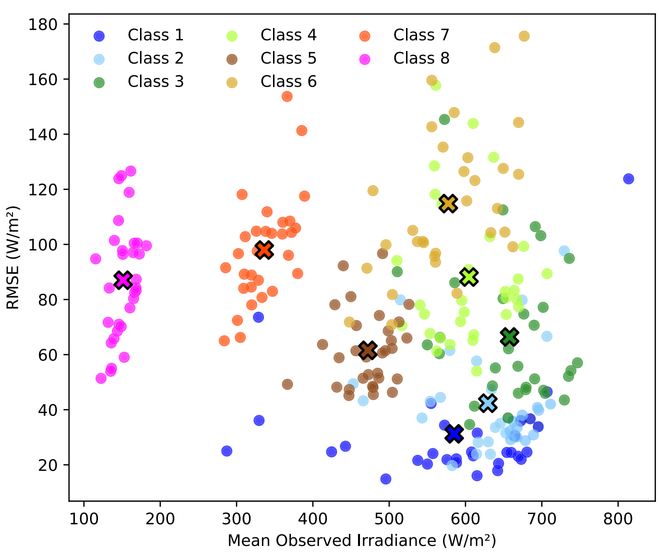

Fig. 9. Distribution of the RMSE values vs the mean of observed GHI for each variability class per station.

For classes 2 and 3, the MBE remains relatively small but RMSE begins to increase. For these two classes, the overestimations in the desert and continental regions can be attributed to the presence of small cirrus clouds above the ground stations that may not be fully detected within the satellite pixel or the opposite would imply to the negative biases observed at a few stations. The increase in RMSE from class 2 to class 3 likely reflects the increasing spatial mismatch between the point measurement and the satellite pixel as cloud variability increases.

In class 4 conditions, both MBE and RMSE increase compared to the previous classes, indicating growing discrepancies between the satellite retrieval and ground observations. These scenes typically correspond to thin cumulus or partially cloudy conditions, where the satellite pixel contains a mixture of cloudy and clear regions. In such cases, the retrieval algorithm assigns a single representative cloud optical thickness to the entire pixel, which may not accurately reflect the cloud coverage affecting the ground station. This mismatch results in increased random deviations captured by the RMSE and can also introduce systematic biases reflected in the MBE. Additionally, parallax effects and viewing geometry become increasingly relevant for these partly cloudy situations, particularly for stations with vza larger than ∼ 60°, where the translation of satellite brightness into cloud optical depth becomes more uncertain.

It should be noted that most stations have a very low proportion of class 5 clouds for the studied timeframe with the exception of GUR, HOW and TIR. This class typically represents situations with moderately thick cirrus clouds with medium variability, where the satellite pixel often contains a mixture of cloudy and partially clear regions. As for class 4, the single pixel mixture of cloudy scenes may increase RMSE due to the variability within the pixel, while the MBE may exhibit both positive and negative deviations depending on whether the cloud presence within the satellite pixel is overestimated or underestimated relative to the ground observation.

In the optically thick clouds classes, most of the stations have occurrences of 20–36% optically thick broken cloud conditions (combining classes 6 and 7) with the exception of ASP, BRO, LEA and GUR in the timeframe studied here which have the least number of clouds in these classes. The size of the MBE and RMSE is substantially large for class 6 and 7. The large magnitude of both MBE and RMSE for these classes reflects the increasing difficulty of representing such cloud conditions within the satellite retrieval. The impact of sub-pixel cloud variability becomes more pronounced in these classes, as well in class 4. These large values can be attributed to the heterogeneity within the cloudy pixel where scattered and/or multilayered clouds lead to substantial spatial variability in surface irradiance. Typically, the operational setup relies on simplified plane-parallel assumptions, which limit the ability to fully represent the complex radiative effects associated with heterogeneous cloud structures. In particular, processes such as parallax displacement and multiple scattering are not fully represented. The impact of parallax effects becomes especially relevant for stations observed at large viewing zenith angles, where the apparent cloud position may differ from the location influencing the ground measurement. Currently, parallax correction is not applied in the CAMS operational service, although the implementation of a new cloud-top-temperature-based parallax correction scheme is under investigation.

Previous studies have shown that this heterogeneity has a large impact in the broken clouds filed and remains significant in the overcast clouds (Barker and Davies, 1992; Girodo et al., 2006). In addition to horizontal photon transport arising from the three-dimensional structure of clouds, further 3-D cloud radiative effects such as radiation enhancement (RE) can occur. These effects are not represented in the

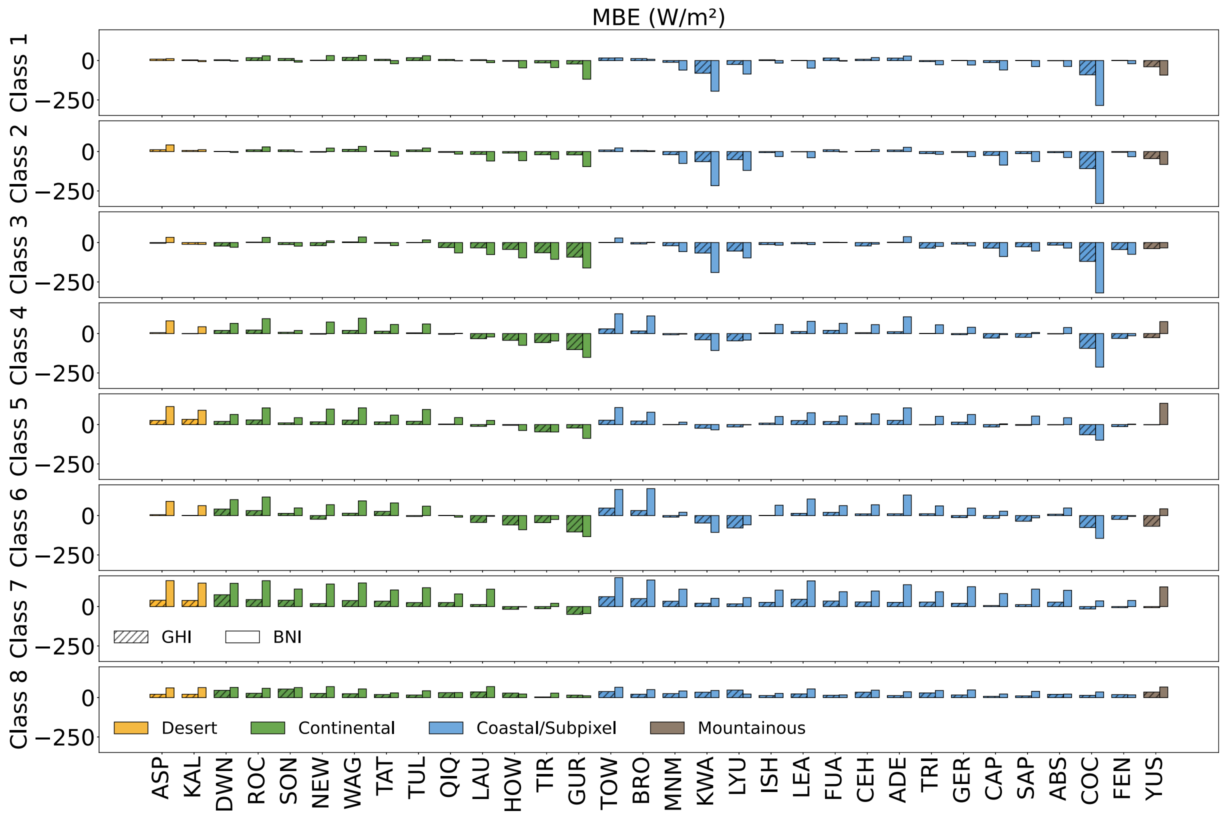

Fig. 10. Relative MBE for hourly all-sky GHI and BNI for the in different geographical regions as in desert (orange), continental (green) and coastal/subpixel (blue) and mountainous (brown) regions for all the variability classes (1–8). The stations are ordered in each group in terms of increasing vza.

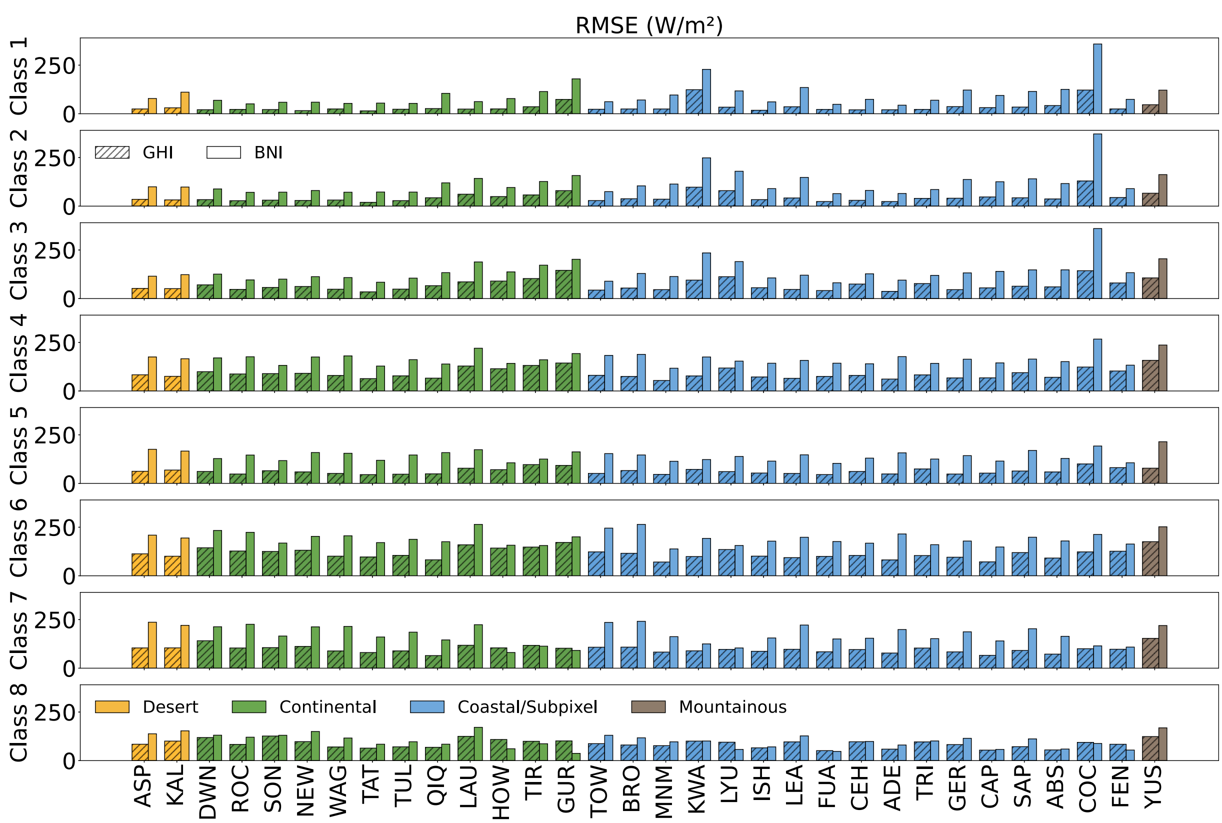

Fig. 11. Relative RMSE for hourly all-sky GHI and BNI in different geographical regions as in desert (orange), continental (green) and coastal/subpixel (blue) and mountainous (brown) regions for all the variability classes (1–8). The stations are ordered in each group in terms of increasing vza.

DISORT radiative transfer solver used in LibRadtran, and consequently are not included in the Heliosat-4 look-up tables used in the operational retrieval. RE events are typically associated with cumulus cloud systems in various heights (Schade et al., 2007; Mol et al., 2023) and may occur when scattered optically thick clouds are located in the vicinity of the direct sunlight's path. Such conditions can locally enhance surface irradiance, potentially producing negative biases in the satellite-derived irradiances under broken cloud regimes.

In contrast to classes 6 and 7, class 8 shows smaller MBE and RMSE, despite the presence of large optically thick clouds. This improvement is likely related to the greater homogeneity of the cloud field under fully overcast conditions. Under such circumstances, the plane-parallel assumptions used in the radiative transfer modeling are likely to be better satisfied, allowing the satellite retrieval to represent the surface irradiance more accurately. However, fully homogeneous conditions may not be realized and some deviations may still occur due to unresolved cloud variability and viewing geometry effects.

Only a few studies explore the impact of different cloud conditions on the SSI. Damiani et al. (2018) used clearness index based on ground observations to create six classes including RE (radiation enhancement) events, and carried out the comparison of the AMATERASS product against SKYNET stations and reported that the largest underestimation was observed for the RE events, the largest overestimation for the overcast conditions and the overestimation inclined to decrease towards clearer conditions. Tan et al. (2023) also performed the comparison of their SSI estimates resulting from different machine learning methods and the ensemble with BSRN station for sky index-based weather classification (Igawa, 2014) dividing the sky conditions into 5 classes ranging from Clear, I-Clear, Intermediate, and I-Overcast and Overcast (where I stands for intermediate). The results from all algorithms for the five different weather conditions showed highest deviations for the overcast conditions, subsequently performing better towards the clearer cases and having the lowest overestimations for the clear sky conditions. Our results illustrate the tendency to a better accuracy in overcast conditions compared to heterogeneous cloud conditions which illustrates the better satisfying CRS performance in homogeneous conditions if compared to other studies. Nevertheless, heterogeneous cloud conditions remain a challenge. Further service evolution will be monitored with the help of this recently introduced evaluation framework providing much deeper insight into different cloud conditions and their impact.

4.4. Diurnal, seasonal, and interannual assessment

Temporal variability analysis, including diurnal, seasonal, and interannual variations is presented to assess retrieval performance under different solar zenith angles and daily cloud evolution, as well as systematic changes associated with atmospheric and cloud patterns throughout the year. This analysis also evaluates the stability and robustness of the retrieval across multiple years of Himawari

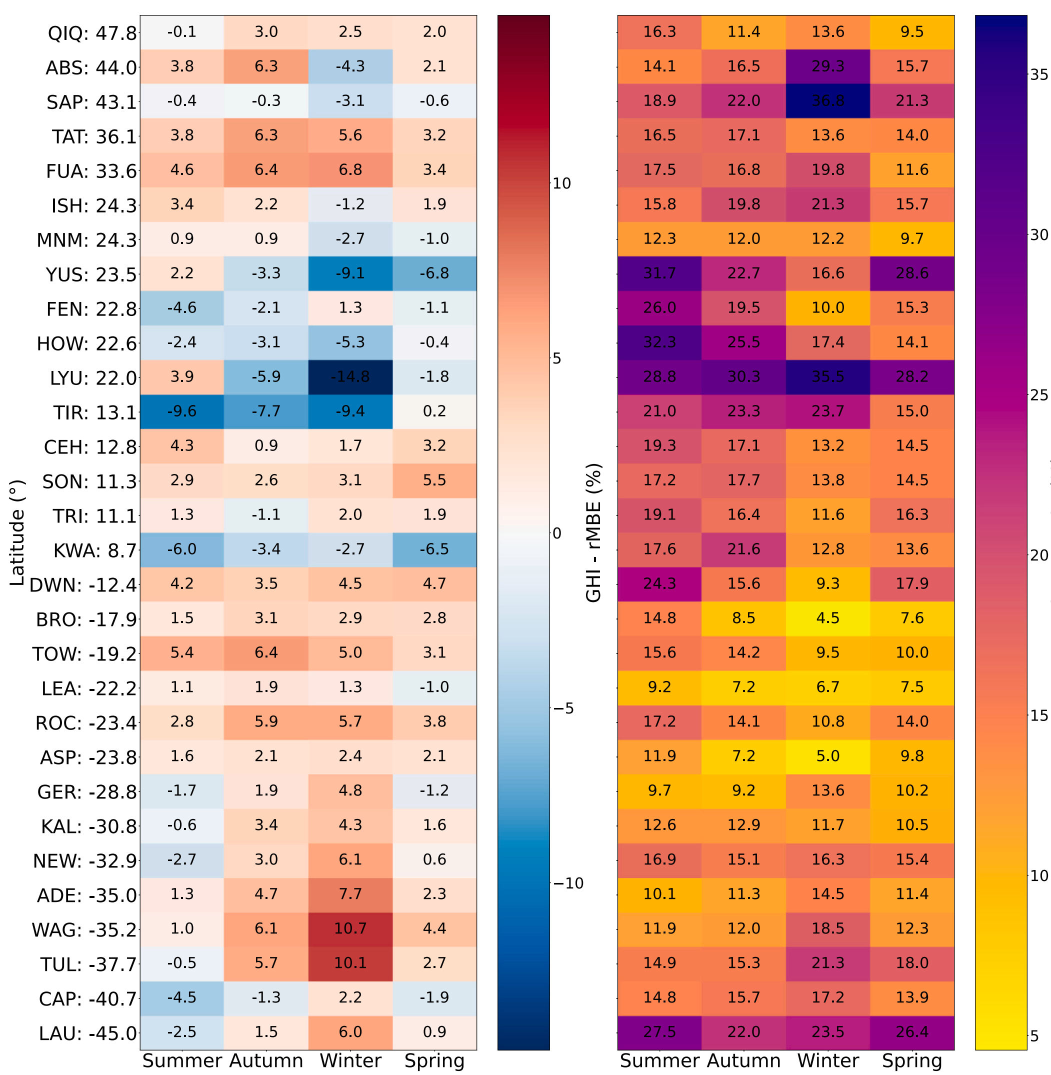

Fig. 12. GHI rMBE and rRMSE per season for all stations. The stations are ordered according to the increasing latitude.

observations and complements the regime-based evaluation to provide a more comprehensive understanding of the CRS performance.

Fig. 12 shows the rMBE and rRMSE metrics for GHI per season for all stations, which are ordered according to the increasing latitude excluding the COC location. Since similar seasonal patterns were found for BNI, here only the seasonal metrics of GHI are shown.

Overall, the rMBE remain relatively small for most of the stations typically within ±5%. Some stations exhibit stronger seasonal deviations e.g. LYU shows the strongest negative bias in winter (−14.8%) while WAG and TUL show the largest positive bias in winter (10–11%). A general pattern can be observed in MBE for stations located in the mid-latitudes (above 30° and below −30°). At these locations, winter and autumn having large solar zenith angle (SZA) tend to exhibit more positive MBE values. In contrast, summer and spring generally show MBE values closer to zero, corresponding to more favorable solar illumination conditions. Within the tropical region (−30° to 30°) the MBE is negative in the north and positive in the south. This suggests that local cloud variability and scene heterogeneity may play a larger role in controlling the bias in these regions.

For the RMSE, the stations of ABS and SAP exhibit the highest percentages of overcast conditions (joining classes 7 and 8) and a correspondingly larger RMSE in the winter (29.3% and 36.8%, respectively), which may be related to the snow presence affecting the retrieval. The YUS station also shows higher RMSE in summer and spring, which may be associated to its high elevation (3858 m). The next stations with large RMSE values are LYU, HOW, and LAU. LYU has a considerable percentage of broken cloud conditions (36.7% joining classes 4 and 6), which are challenging for the retrieval as discussed in the previous section. HOW and LAU are located close to the edge of Himawati FOV (∼60° vza) influenced by the geometrical factors as discussed previously. Overall, the RMSE mainly exhibits location specific issues and do not show retrieval specific problems across the seasons.

The diurnal analysis is performed using the boxplots for 32 stations excluding the COC station as a function of True solar time (TST), as shown in Fig. 13. Higher biases are observed both in GHI and BNI at the morning and late afternoon hours where the GHI bias is higher in the afternoon compared to the morning hours. This higher afternoon bias in GHI may be explained by the cloud formation happening during the day resulting in more cloudy situations. At the middle of the day, the errors in the medians are lower indicating stable retrieval performance during high solar elevation. The spread in the bias at and around midday is larger compared to the edges which may be related to the CRS retrieval heterogeneity within the 32 stations.

In general, the GHI RMSE is larger at and around midday, reflecting the dependence of radiative transfer processes on solar zenith angle (SZA), which is implicitly represented through the diurnal TST analysis. The medians of BNI RMSE remain relatively consistent due to its lesser sensitivity to the solar zenith angle compared to GHI. Additional diagnostic checks performed as a function of solar zenith angle (not shown) revealed patterns consistent with the TST-based results, confirming that the diurnal representation captures the dominant solar geometry dependence relevant for the retrieval performance.

For the interannual assessment, only TAT, MNM, FUA, ISH, SAP, WAG, TUL, ADE, BRO, CAP, ROC, ASP, DWN, LAU stations were considered, as they provide consistent data coverage during the 2016–2020 period. Only years with more than 80% availability were considered for the statistical calculation. The statistics were computed using the hourly time series for each individual year.

Figure 14 presents the interannual variation of CRS GHI and BNI retrieval performance. The GHI MBE remains relatively stable across the

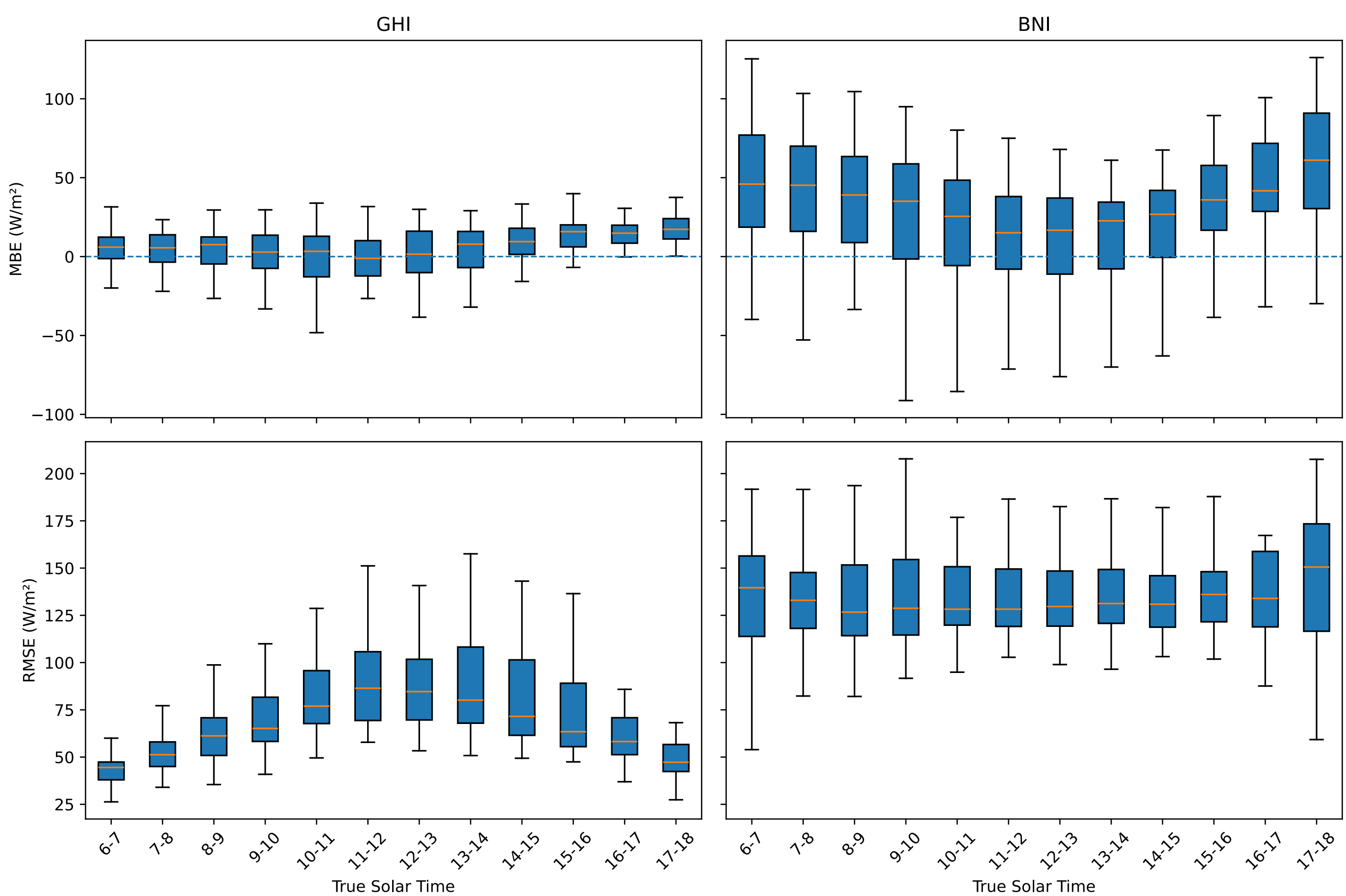

Fig. 13. Diurnal analysis with boxplots of all stations (excluding COC) as a function of True solar time (TST).

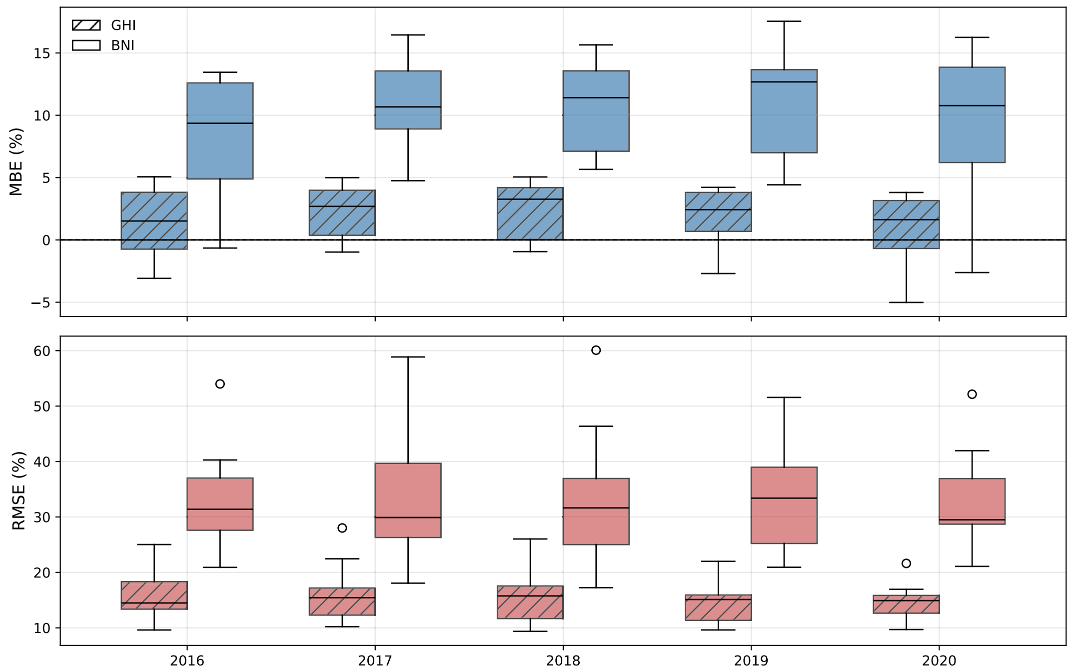

Fig. 14. Interannual variation of CRS model for hourly GHI and BNI in terms of relative MBE and RMSE.

years, with median values ranging from 1.5 to 3.3%, while the RMSE varies between 14.5% and 15.8%. For BNI, the MBE medians range from approximately 9.4% to 12.7%, and the RMSE from 29.5% to 33.4%. Overall, the interannual variation of the statistics is small, indicating stable performance of the CRS retrieval over the five-year period.

5. Conclusions

This study evaluated the use of APOLLO_NG together with the fast radiative transfer method Heliosat-4 as operated in CAMS Radiation Service v4.6 for the retrieval of surface solar irradiance from Himawari observations. Ground observations from the Baseline Surface Radiation Network (BSRN) and the Australian Bureau of Meteorology (ABoM) and the ones provided by IEA-PVPS were used to compare the all-sky global horizontal and direct normal irradiance.

The study extends the findings previously made for MSG SEVIRI and confirms the previously made choice of 1% as the optimum cloud probability threshold in the cloud masking for solar energy application (Schroedter-Homscheidt et al., 2022).

The assessment was extended to several levels of detail by providing assessments in different ways to describe sky conditions. This includes cloud masking into cloud/cloud-free cases, cloud types mainly reflecting water/mixed phase from thin cirrus cloud discrimination and an additional classification into aerosol- and cloud-type dominated situations as defined by the observed variability in the surface solar irradiance in 1 min ground observations. Compared to previous studies, the level of detail of assessment is not seen before.

The variability classes-based assessment confirms a very good performance of the model for clear and almost clear situation. The evaluation highlights the uncertainties in the CAMS schemes under high albedo surface as shallow water/coastal areas whereas the modelled land albedo may be too high, but any modelled ocean albedo would be very much too low. The effect of snow surface is not investigated in this assessment due to the lack of snow conditions at the validation stations.

The model uncertainty related to the heterogeneous clouds effects is reflected in the higher biases for optically thick broken cloud classes. The broken cloud fields appear to be major contributor to the observed overestimation of all-sky radiation. Overall, the results indicate that the magnitude of the deviations is strongly linked to cloud heterogeneity, viewing geometry, and surface characteristics. The present analysis provides a first quantitative assessment of these effects using irradiance-based variability classes. This new assessment strategy can be used to monitor improvements of the cloud retrieval community in cloud retrieval science in future. The use of irradiances as an evaluation tool provides valuable feedback to the cloud retrieval community as it does not need to assume anything about cloud types or homogeneity of comparison cases and provides integrated assessment in all retrieval conditions with independent observations. However, a full attribution of the individual contributions from cloud heterogeneity, parallax effects, surface albedo uncertainties, and radiative transfer limitations cannot be achieved with the current dataset alone. Ongoing investigations within dedicated observational efforts, including the C3SAR (https://c3sar.de/campaign/) campaign in 2026 and Eye2Sky (Schmidt et al., 2025) network, aim to further disentangle these effects and assess their relative importance under different cloud regimes and viewing condition.

Though the comparison to existing validation studies is restricted due to different sets of stations and time periods, CRS v4.6 evaluation reveals similar or better performance than other published validation studies. A detailed intercomparison of CRS with other datasets at the map or grid scale requires dedicated spatial harmonization and analysis and is therefore beyond the scope of the presented analyses. Such a comparison is the subject of future work.

The CRS v4.6 dataset is well suited for solar resource assessment, allows with its maximum 24hous delayed data provision services for system performance monitoring, provides a long-term and highly quality-controlled dataset for grid integration studies as well as grid extension planning and can be used as training dataset e.g. for the development of solar energy forecasting.

While the present study focuses on establishing a diagnostic evaluation framework, the results directly provide guidance for future retrieval development. The regime-dependent error patterns identified in this study indicate specific areas for methodological refinement that will be addressed in the future evolution activities. These areas include improved treatment of broken cloud fields, improvement of land/sea mask, review of anisotropy correction of various cloud types, an enhanced treatment of multilayer clouds with a revised mixed phase of ice crystals and water droplets. For an improved treatment of the broken clouds in the retrieval which currently assume a horizontally homogenous cloud and neglect 3D cloud reflection effects, the use of 500 m resolved visible channel from the AHI instrument is currently under investigation. The use of high resolution in the irradiance retrievals requires especially the implementation of parallax effects that will be more pronounced than earlier for MSG SEVIRI, which is not yet implemented and therefore currently under investigation.

CRediT authorship contribution statement

Faiza Azam: Writing – review & editing, Writing – original draft, Visualization, Validation, Software, Resources, Project administration, Investigation, Formal analysis, Data curation, Conceptualization. **Diego Rodrigues de Miranda:** Writing – review & editing, Visualization, Validation, Software, Resources, Data curation, Conceptualization. **Marion Schroedter-Homscheidt:** Writing – review & editing, Validation, Resources, Project administration, Methodology, Investigation, Funding acquisition, Data curation, Conceptualization. **Mireille Lefèvre:** Writing – review & editing, Validation, Resources, Investigation, Data curation. **Laurent Saboret:** Writing – review & editing, Validation, Resources, Investigation, Data curation. **Yves-Marie Saint-Drenan:** Writing – review & editing, Validation, Resources, Investigation, Data curation, Conceptualization.

Declaration of competing interest

The authors declare that they have no known competing financial interests or personal relationships that could have appeared to influence the work reported in this paper.

Acknowledgements

The authors thank EUMETSAT and Australian Bureau of Meteorology (ABoM) for HImawari data provision. We would like to also thank all operators of the ground stations of the BSRN network for their valuable measurements and ABoM for providing ground observations from their own network and for contributing to the BSRN network. This study was supported by the Copernicus Atmosphere Monitoring Service (CAMS) as funded by the European Union and implemented by ECMWF.

Appendix A. Ground observations quality control

The Quality control (QC) report gives a full visual picture with not only the often recommended quality tests, but allows also the quality assessment on the basis of time series plots. The tests include K-tests (Geuder et al., 2015; Gueymard, 2017), BSRN closure tests (Long and Dutton, 2002), BSRN extremely rare limit (ERL) and physically possible limit (PPL) tests (Long and Dutton, 2002), Rayleigh lower limit tests (Long and Shi, 2008), overcast lower limit test, and the tracker off test (Long and Shi, 2008). A detailed explanation of all tests used can be found in El Alani et al. (2021).

Fig. A.1 provides an arbitrarily chosen station example for a single data year. Panel 1 provides the general station information. Time series of GHI, Direct Normal Irradiance (DNI) and DHI radiation are displayed in panel 2 and illustrate data availability as well as failures such as pyrheliometer tracker problems or any misalignment of a shadow-band or shading disc. In panels 3a till 13, color coding represents the density of the points. Panel 3 depicts a two-dimensional time representation for the GHI, DNI and DHI components as a function of the time of day and calendar date with overlaid sunrise and sunset. This verifies coherence of the radiation time series, data time-referencing and the temporal resolution. It may detect any pre-filtered data. Panel 4 shows the ratio of the DHI and GHI as a function of time in situations for which the measured DNI is very low (DNI < 10 W/m^2). This detects calibration issues or the presence of other perturbations. Panel 5 is a representation of the ratio of measured GHI, and its estimation made with observations of diffuse and direct components as a function of time. This identifies problems in calibration, perturbation as shading, or noise if the three sensors are not collocated. In panels 6, 8, and 10, the GHI, DNI and DHI irradiance are plotted as a function of top of atmosphere (TOA) irradiance. This visualizes Physically Possible Limit (PPL) and Extremely Rare Limit (ERL) tests proposed by Long and Dutton (2002) as grey curves. Panel 7 displays the diffuse fraction, i.e., the ratio of DHI to GHI, as a function of solar zenith angle (SZA) known as the two-component test of the BSRN quality control. Limits of tests are displayed by a dotted line. Panel 9 provides the SERI K tests (Habte and Sengupta, 2019). GHI and DNI are normalized by the TOA counterpart (by definition kt and kn respectively) and displayed in a scatter plot. Panel 11 plots the diffuse fraction as a function of clearness index. It verifies the coherence of GHI and DHI. The limits by Geuder et al., 2015 (black dotted line) verify that the DHI is not greater than the GHI and that the DHI is smaller than the GHI for clearness indices greater than 0.6. Panels 12 and 13 are different visualizations of the BSRN closure tests (Long and Dutton, 2002) already used in panel 5. In panel 12, measurements of GHI are displayed as a function of estimates made with the direct and diffuse components in a scatter plot. The black lines in this plot are the limits set for different SZA values (SZA $< 75^\circ$ and SZA $> 75^\circ$). The ratio of the GHI measurements and the GHI estimated by its components is shown as a function of the SZA in panel 13. In panels 14a, 14b and 14c, the histograms of kt, kn and the diffuse fractions are given. The valid and the flagged data shown are separately in blue and red. These histograms allow to identify if a station has a significant modification of statistical distributions e.g. due to a severe shadowing or misalignment issues. Panel 15a and panel 15b evaluate the effects of possible shadow on GHI and DNI after normalizing measurements to kt and kn respectively.

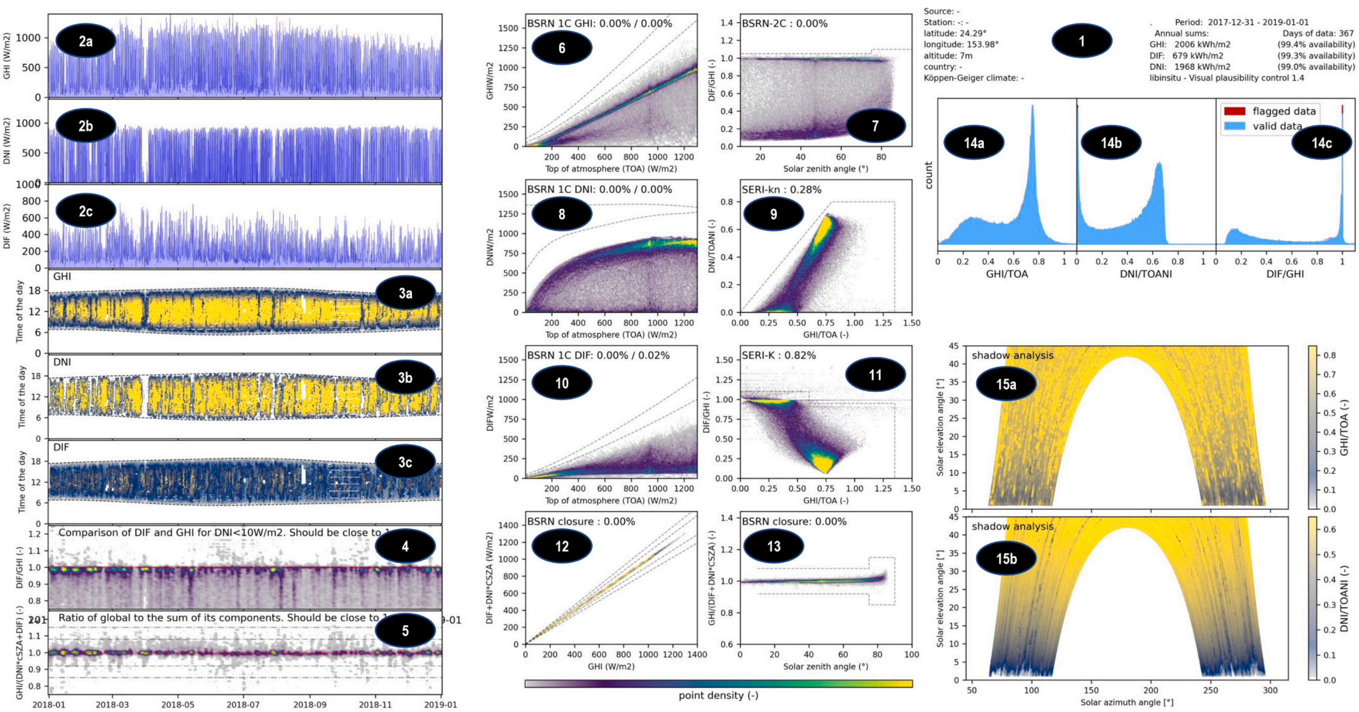

Fig. A.1. Different panels of the multiplot approach used for the visual inspection of the ground measurements. The panels are numbered to facilitate the description of the different analysis performed in the visual control.

Appendix B. Investigation of CRS retrieval under challenging situations over island stations

Some specific days from the stations BSRN-COC, BSRN-MNM, and BSRN-KWA are further investigated under close to clear and scattered cloud sky conditions. These stations are located in coastal/subpixel areas, with Cocos Island (COC) in the Indian Ocean with the largest satellite zenith angle (vza) of 53° among the island stations, and Minamitorishima (MNM) and Kwajalein (KWA) islands in the Pacific Ocean with vza of 32.1° and 33°, respectively. All the figures presented in the left panels in each plot show the GHI, clear-sky GHI and BNI 1 min measurements, the hourly GHI and CRS GHI (named as CAMS GHI) as well as the hourly variability classes (depicted with bars in the background). The center panel shows the MODIS True Color composite and the right panel shows the RGB composite from APOLLO_NG, where the thermal infrared channel is used as 'blue' channel, highlighting lower-level warm clouds being in yellowish and colder clouds (optically thin cirrus or thin ice cirrus) in blueish color.

The retrieval on island stations can be challenging when shallow waters are interpreted as cloud cover if the land/sea mask assume the pixel to be an ocean. Fig. B.1 shows a day dominated by clear sky, cirrus and sub-visible cirrus clouds (classes 1, 2, and 3) for the COC island. The shallow waters in the archipelago are visible in greenish tones in the MODIS image and brown and yellow in the APOLLO_NG composite. For this specific day, the CRS GHI underestimates the measured GHI resulting in negative MBE. In contrast, Fig. B.2 shows the results for MNM station for a clear sky hour. MNM has no visible surrounding shallow waters thereby simplifying the conditions and contributing to the improved accuracy of the CRS retrieval (−0.3% of MBE compared to −12.2% of MBE in COC island for all-sky conditions). The KWA station is also surrounded by shallow waters at its coastline but to a lesser extent than in COC, as shown in Fig. B.3 which explains the smaller but also negative MBE observed at this location persistently during all seasons.

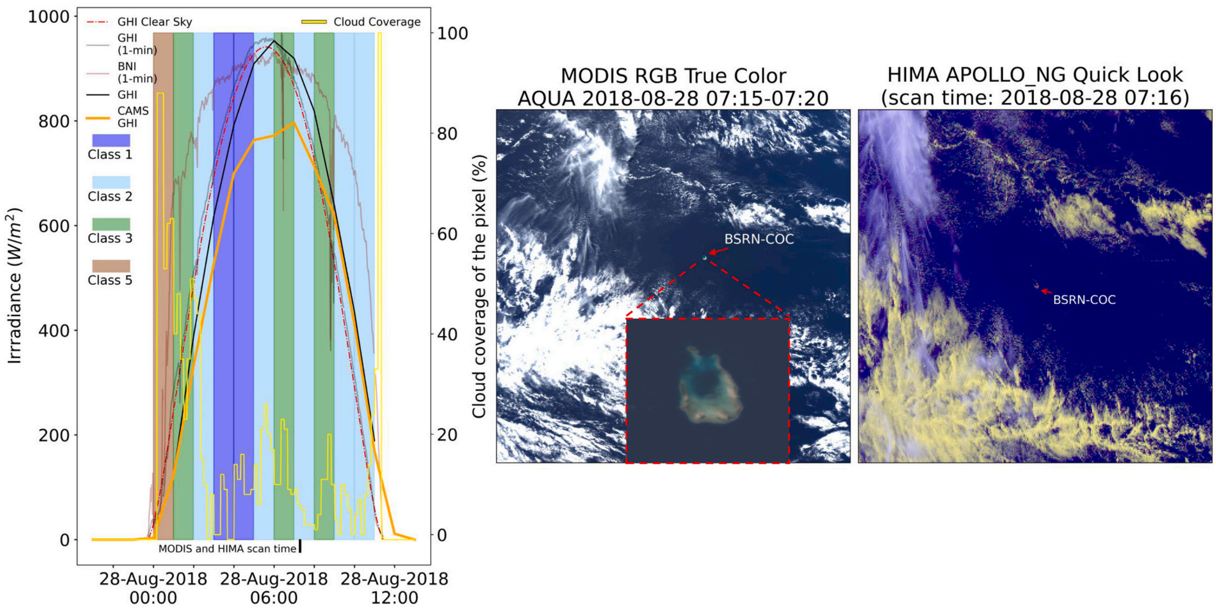

Fig. B.1. Clear sky and thin cirrus sky conditions on August 28, 2018 at BSRN-COC (Himawari imagery © JMA/EUMETSAT/DLR).

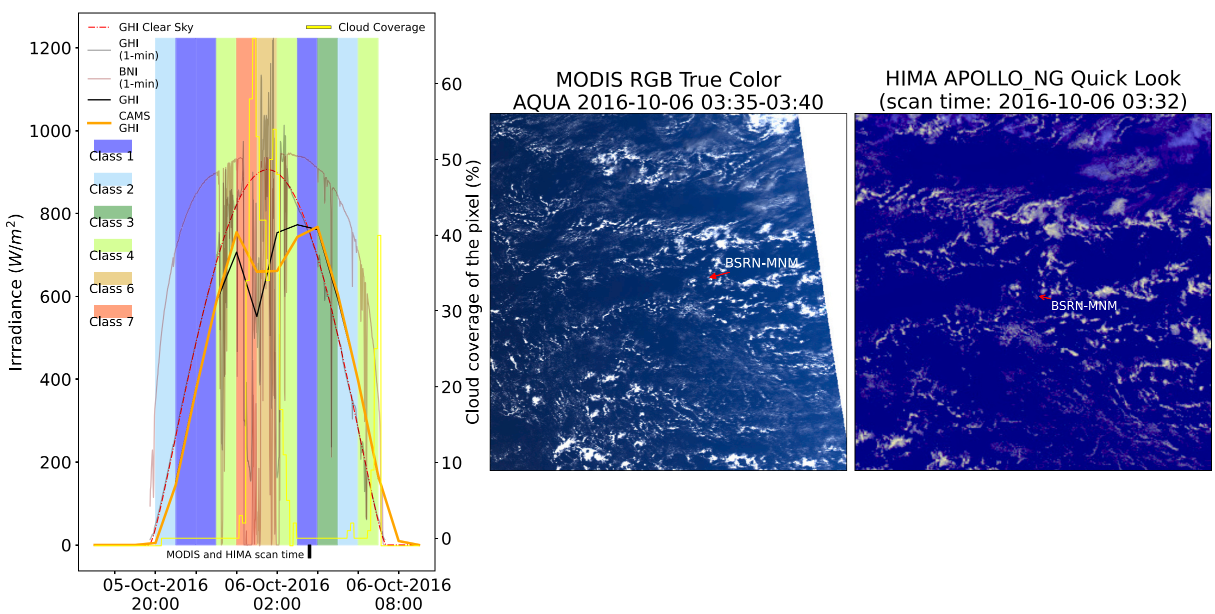

Fig. B.2. Clear sky, thin cirrus, and scattered clouds sky conditions on October 05, 2016 at BSRN-MNM (Himawari imagery © JMA/EUMETSAT/DLR).

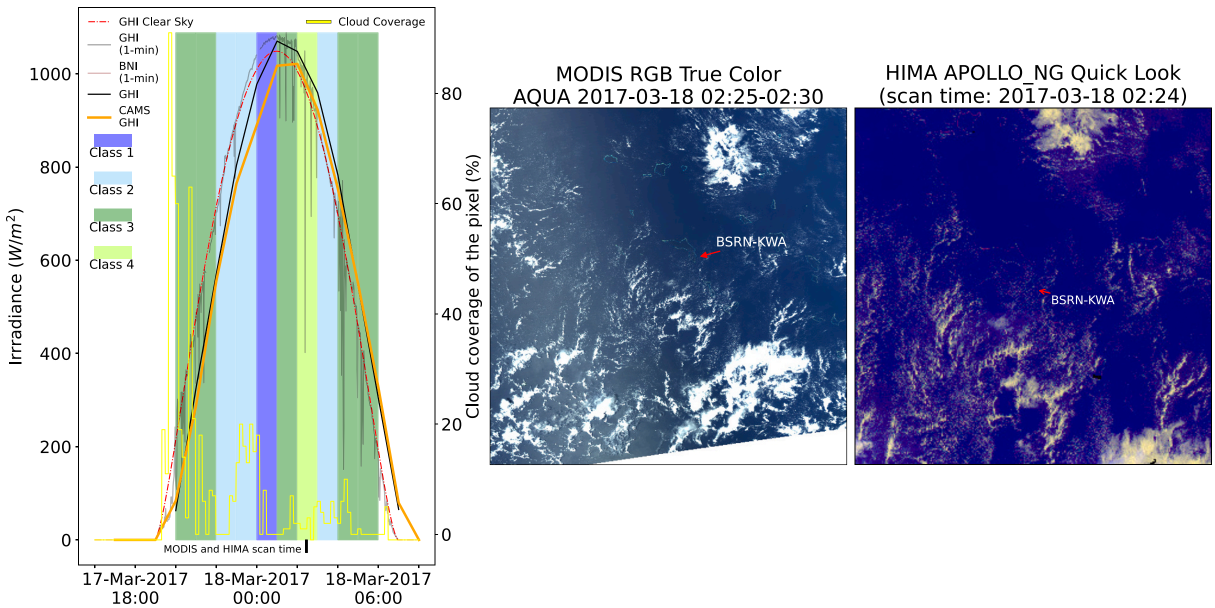

Fig. B.3. Clear sky and thin cirrus sky conditions on Mach 17, 2017 at BSRN-KWA (Himawari imagery © JMA/EUMETSAT/DLR).

Figs. B.4 and B.5 show the results of COC and MNM in scattered cloud conditions. For COC, the MBE is more accurate as thicker clouds are covering the shallow waters in most situations for the day under consideration. RMSE increases as the peaks of the scattered clouds do not always align due to the high variability conditions which pose challenges to the retrieval, as the plane parallel cloud assumption are not fulfilled.

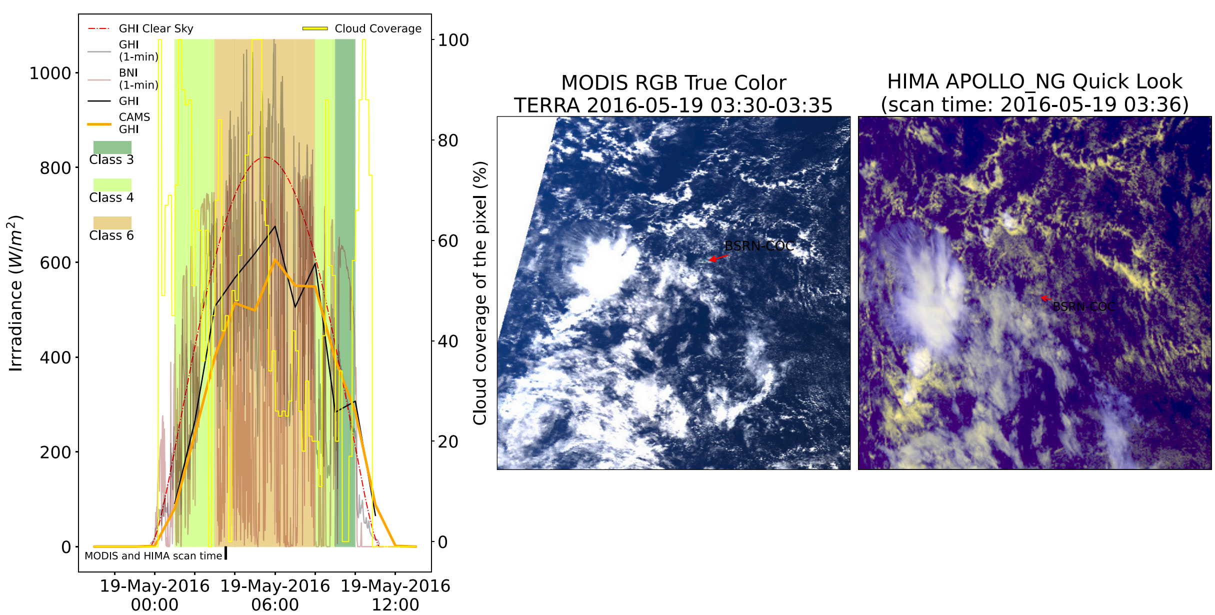

Fig. B.4. Day dominated by scattered cloud conditions on May 19, 2016 at BSRN-COC (Himawari imagery © JMA/EUMETSAT/DLR).

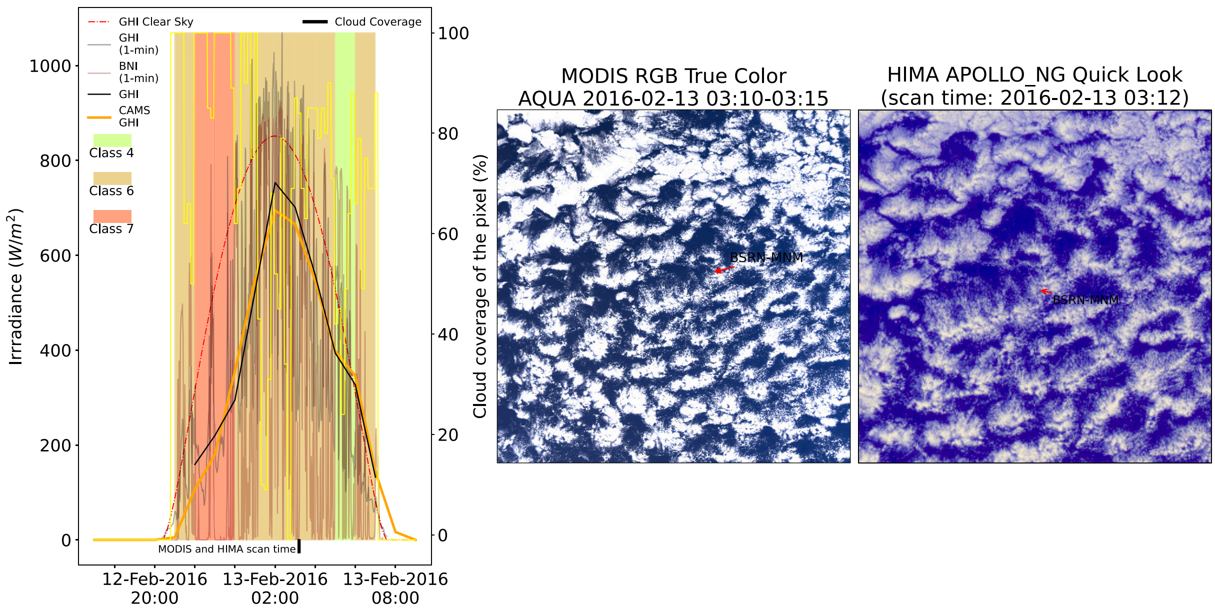

Fig. B.5. Day dominated by scattered cloud conditions on February 12, 2016 at BSRN-MNM (Himawari imagery © JMA/EUMETSAT/DLR).

Appendix C. Visual illustrations of irradiance variability classes and corresponding cloud conditions

Satellite imagery from the APOLLO-NG cloud retrieval algorithm (based on MSG) and MODIS RGB True Colors composites were used to visually associate the variability classes with the more common cloud types and conditions for all cases in the Carpentras reference database (de Miranda et al., 2026). Examples are given in Table C.1. The first column shows GHI and BNI 1-min resolved timeseries from the reference database used for classification, highlighting the hour being classified. The second column displays the color composite image from APOLLO_NG channels together with its cloud mask output. The third column presents a MODIS true color image within the corresponding time window. Finally, the fourth column provides a description of each class.

Table C.1
A visual demonstration of the classes through example images from the reference database used in classification by de Miranda et al. (2026) (first column), the composite from SEVIRI and the cloud masking (white: fully cloudy, grey: partially cloudy, brown/blue: cloud-free land/water) output from APOLLO_NG respectively (second column), the true color composite from MODIS for the timestamp lying within the classification window (third column) and the description of the frequently found cloud types corresponding to each class (fifth column) (MSG imagery © EUMETSAT/DLR).

Ground reference database used for classification	APOLLO_NG channels composite (left) and Cloud Mask (right)	MODIS RGB True Color	Classes description
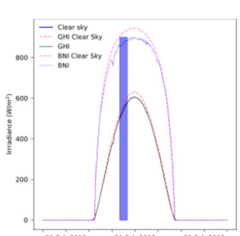	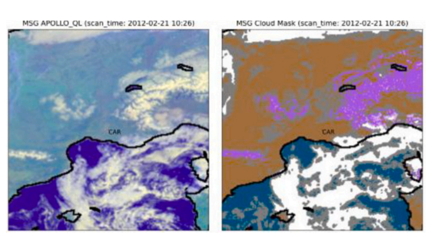	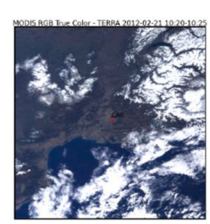	**Class 1** – Clear sky
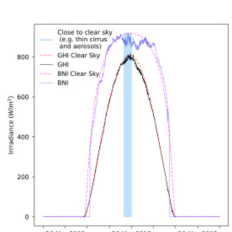	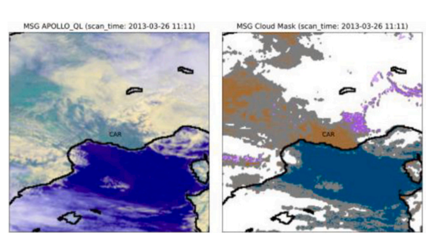	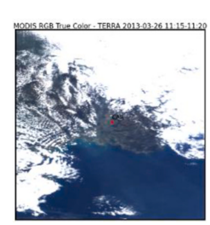	**Class 2** – Thin cirrus, aerosols and very small convective clouds may occur seldomly

(continued on next page)

Table C.1 (*continued*)

Ground reference database used for classification	APOLLO_NG channels composite (left) and Cloud Mask (right)	MODIS RGB True Color	Classes description
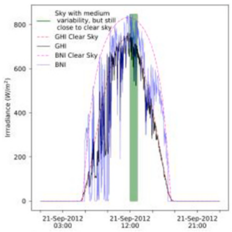	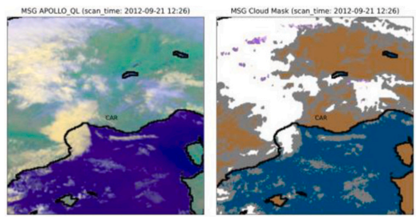	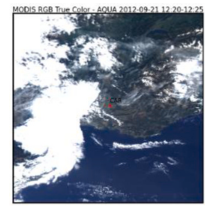	**Class 3** – Thick spatially heterogenous cirrus conditions or small cumulus clouds
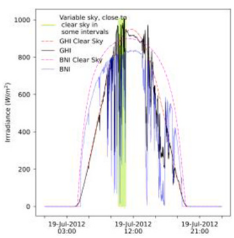	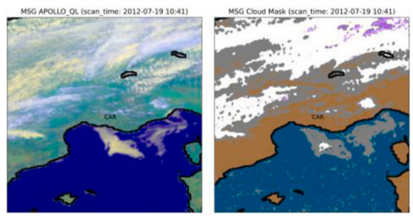		**Class 4** – Visible and sub-visible cumulus clouds
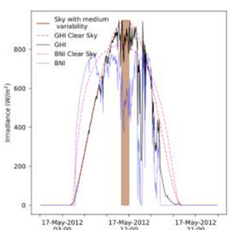	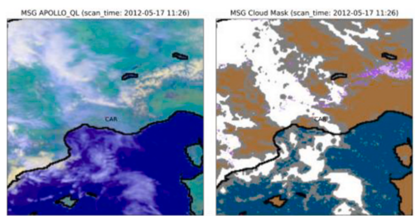	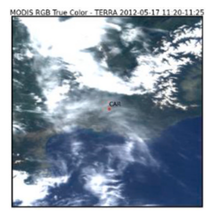	**Class 5** – Thick heterogenous cirrus with higher optical thickness than in class 3
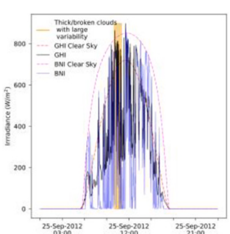	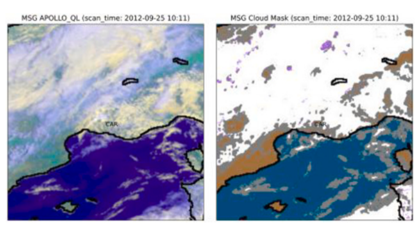	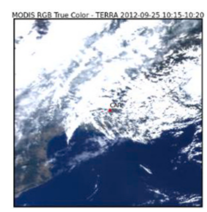	**Class 6** – Dominated by multilayer clouds (broken low clouds and cirrus fields)
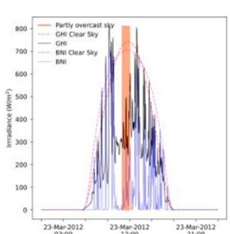	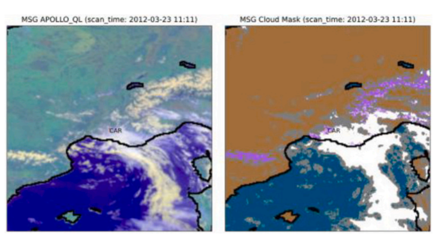	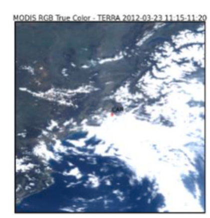	**Class 7** – Multilayer clouds with a larger optical thickness than class 6
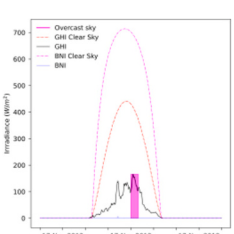	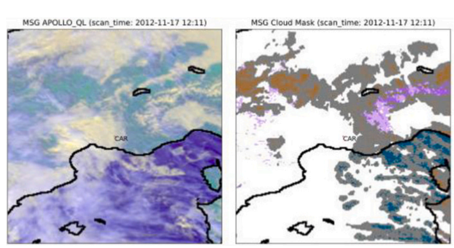	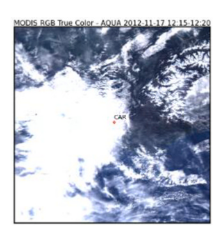	**Class 8** – Single-layer or multi-layer stratus with higher optical thickness, may have an upper layer non-stratus cirrus field

Appendix D. Statistical metrics with uncertainty for the variability-based assessment

The MBE and RMSE in W/m^2 per variability class are presented here in Tables D.1 until D.4. Right below the reported metrices, uncertainty bounds using the non-parametric bootstrap approach are shown, considering 95% confidence intervals (CI) of the MBE and RMSE bootstrap distributions.

Table D.1
GHI MBE (W/m^2) per variability class.

<table>
<tr><th></th><th>Class 1</th><th>Class 2</th><th>Class 3</th><th>Class 4</th><th>Class 5</th><th>Class 6</th><th>Class 7</th><th>Class 8</th></tr>
<tr><td rowspan="2">ASP</td><td>9.1</td><td>11.8</td><td>−4.4</td><td>5.9</td><td>26.9</td><td>5.6</td><td>40.6</td><td>21</td></tr>
<tr><td>8.6|9.6</td><td>10.2|13.4</td><td>−7.7|-1.3</td><td>1.3|10.7</td><td>21.9|31.9</td><td>−3.0|14.1</td><td>35.4|45.9</td><td>16.4|25.7</td></tr>
<tr><td rowspan="2">KAL</td><td>4.2</td><td>6.9</td><td>−11</td><td>−1</td><td>33.3</td><td>0.9</td><td>39</td><td>21.1</td></tr>
<tr><td>3.4|5.0</td><td>5.3|8.7</td><td>−13.6|-8.2</td><td>−5.1|2.7</td><td>28.4|38.2</td><td>−4.3|6.0</td><td>34.0|43.8</td><td>15.8|26.3</td></tr>
<tr><td rowspan="2">DWN</td><td>5.1</td><td>1.3</td><td>−22.1</td><td>20</td><td>20.6</td><td>41.5</td><td>75.3</td><td>46.2</td></tr>
<tr><td>4.1|6.0</td><td>0.1|2.5</td><td>−25.3|-18.9</td><td>16.0|24.0</td><td>17.4|23.9</td><td>35.0|47.7</td><td>69.8|80.7</td><td>41.0|51.4</td></tr>
<tr><td rowspan="2">ROC</td><td>18.2</td><td>11.3</td><td>3</td><td>22.4</td><td>29.7</td><td>31.7</td><td>44.6</td><td>27.4</td></tr>
<tr><td>17.8|18.7</td><td>10.0|12.5</td><td>0.5|5.3</td><td>19.4|25.7</td><td>26.9|32.3</td><td>26.6|36.7</td><td>40.8|48.4</td><td>23.6|31.1</td></tr>
<tr><td rowspan="2">SON</td><td>13.2</td><td>10.6</td><td>−13.1</td><td>8.4</td><td>11</td><td>14.1</td><td>40.5</td><td>54.3</td></tr>
<tr><td>11.5|14.9</td><td>9.1|11.9</td><td>−16.9|-9.4</td><td>2.7|14.1</td><td>6.9|15.0</td><td>3.8|23.3</td><td>35.1|46.1</td><td>47.8|61.1</td></tr>
<tr><td rowspan="2">NEW</td><td>2.4</td><td>−3.9</td><td>−19.8</td><td>−3.9</td><td>17.6</td><td>−23.3</td><td>19</td><td>26.3</td></tr>
<tr><td>1.7|3.1</td><td>−5.7|-2.3</td><td>−23.9|-15.7</td><td>−9.7|2.0</td><td>12.0|23.1</td><td>−31.8|-14.4</td><td>13.2|24.8</td><td>20.9|31.7</td></tr>
<tr><td rowspan="2">WAG</td><td>20.6</td><td>13.7</td><td>4.2</td><td>20.2</td><td>28.5</td><td>14.9</td><td>38.5</td><td>24.5</td></tr>
<tr><td>20.2|21.0</td><td>12.4|14.9</td><td>1.8|6.7</td><td>16.6|23.7</td><td>26.0|31.0</td><td>9.9|20.0</td><td>35.3|41.5</td><td>22.0|27.0</td></tr>
<tr><td rowspan="2">TAT</td><td>8.2</td><td>3.8</td><td>−4.2</td><td>15.1</td><td>16.8</td><td>27</td><td>34.6</td><td>19.6</td></tr>
<tr><td>7.8|8.6</td><td>3.2|4.4</td><td>−5.5|-2.9</td><td>13.0|17.1</td><td>15.0|18.6</td><td>23.4|30.8</td><td>32.8|36.3</td><td>18.4|20.8</td></tr>
<tr><td rowspan="2">TUL</td><td>18.3</td><td>10.4</td><td>−0.9</td><td>4.8</td><td>21</td><td>−5.7</td><td>25.3</td><td>16.3</td></tr>
<tr><td>17.8|18.9</td><td>9.0|11.7</td><td>−3.5|1.8</td><td>1.4|8.1</td><td>18.0|23.8</td><td>−10.0|-1.2</td><td>22.5|28.2</td><td>14.2|18.5</td></tr>
<tr><td rowspan="2">QIQ</td><td>7.2</td><td>−4.9</td><td>−31.9</td><td>−4.5</td><td>3.4</td><td>1.1</td><td>25.6</td><td>31.3</td></tr>
<tr><td>5.1|9.2</td><td>−8.2|-1.8</td><td>−39.3|-24.7</td><td>−13.9|4.7</td><td>−2.0|8.3</td><td>−13.6|15.2</td><td>19.9|31.3</td><td>25.8|37.2</td></tr>
<tr><td rowspan="2">LAU</td><td>5.5</td><td>−17.9</td><td>−33.9</td><td>−32.6</td><td>−11.2</td><td>−43.7</td><td>13</td><td>35.8</td></tr>
<tr><td>4.4|6.4</td><td>−21.8|-14.4</td><td>−38.5|-29.3</td><td>−39.5|-25.7</td><td>−17.0|-5.5</td><td>−52.8|-34.5</td><td>8.3|17.7</td><td>31.8|39.7</td></tr>
<tr><td rowspan="2">HOW</td><td>−4.4</td><td>−9.4</td><td>−43.8</td><td>−43</td><td>−4.6</td><td>−59.5</td><td>−17.2</td><td>28.7</td></tr>
<tr><td>−8.1|-1.0</td><td>−11.9|-6.9</td><td>−51.7|-35.1</td><td>−53.9|-31.5</td><td>−9.5|0.5</td><td>−74.7|-44.8</td><td>−24.0|-10.2</td><td>21.3|36.8</td></tr>
<tr><td rowspan="2">TIR</td><td>−14.6</td><td>−20.2</td><td>−64.9</td><td>−57.1</td><td>−46.4</td><td>−44.9</td><td>−13.5</td><td>3.9</td></tr>
<tr><td>−19.7|-9.7</td><td>−22.9|-17.4</td><td>−71.2|-59.1</td><td>−65.2|-48.7</td><td>−51.0|-41.5</td><td>−61.0|-29.6</td><td>−20.1|-6.4</td><td>−2.6|10.9</td></tr>
<tr><td rowspan="2">GUR</td><td>−21.7</td><td>−20.8</td><td>−92.9</td><td>−101.7</td><td>−21.7</td><td>−104</td><td>−49.6</td><td>15.5</td></tr>
<tr><td>−32.4|-10.2</td><td>−25.3|-16.3</td><td>−107.1|-77.9</td><td>−117.2|-85.6</td><td>−27.3|-16.5</td><td>−127.7|-79.6</td><td>−57.3|-41.6</td><td>5.3|26.6</td></tr>
<tr><td rowspan="2">TOW</td><td>16.4</td><td>10</td><td>1</td><td>30.1</td><td>27.7</td><td>47.6</td><td>62.8</td><td>38.6</td></tr>
<tr><td>15.8|16.9</td><td>8.8|11.1</td><td>−1.3|3.3</td><td>26.6|33.6</td><td>24.7|30.8</td><td>41.2|53.6</td><td>58.6|66.8</td><td>34.6|42.5</td></tr>
<tr><td rowspan="2">BRO</td><td>12.9</td><td>7.3</td><td>−8.8</td><td>16.4</td><td>22.5</td><td>32.1</td><td>50.5</td><td>21.3</td></tr>
<tr><td>12.5|13.4</td><td>6.0|8.5</td><td>−11.7|-6.0</td><td>12.9|20.0</td><td>18.5|26.2</td><td>24.8|39.4</td><td>45.5|55.5</td><td>16.7|26.0</td></tr>
<tr><td rowspan="2">MNM</td><td>−11.1</td><td>−19.8</td><td>−20.2</td><td>−7.6</td><td>−1</td><td>−9.9</td><td>34</td><td>25.1</td></tr>
<tr><td>−12.1|-10.2</td><td>−20.9|-18.8</td><td>−21.3|-19.2</td><td>−8.7|-6.5</td><td>−3.5|1.5</td><td>−12.0|-7.8</td><td>32.1|36.2</td><td>22.8|27.4</td></tr>
<tr><td rowspan="2">KWA</td><td>−80.5</td><td>−64.2</td><td>−66.5</td><td>−39.6</td><td>−23.3</td><td>−47.2</td><td>21.3</td><td>34.2</td></tr>
<tr><td>−100.4|-63.2</td><td>−73.1|-55.7</td><td>−70.8|-62.1</td><td>−43.0|-36.1</td><td>−31.2|-15.9</td><td>−53.1|-41.7</td><td>15.7|27.6</td><td>26.8|41.9</td></tr>
<tr><td rowspan="2">LYU</td><td>−24.7</td><td>−51.8</td><td>−53.9</td><td>−46.1</td><td>−15.1</td><td>−78.8</td><td>17.4</td><td>47.9</td></tr>
<tr><td>−28.9|-20.8</td><td>−58.4|-45.8</td><td>−60.5|-47.2</td><td>−50.6|-41.8</td><td>−22.9|-7.6</td><td>−82.0|-75.7</td><td>14.6|20.0</td><td>45.9|49.9</td></tr>
<tr><td rowspan="2">ISH</td><td>5</td><td>−6.5</td><td>−13</td><td>4</td><td>9.2</td><td>1.1</td><td>26.9</td><td>13.1</td></tr>
<tr><td>3.8|6.0</td><td>−7.9|-5.2</td><td>−14.9|-11.2</td><td>2.2|5.8</td><td>6.3|12.0</td><td>−1.7|4.0</td><td>24.9|28.8</td><td>11.9|14.3</td></tr>
<tr><td rowspan="2">LEA</td><td>−0.4</td><td>−1.8</td><td>−7.4</td><td>13.1</td><td>25.8</td><td>14.2</td><td>46.5</td><td>23.4</td></tr>
<tr><td>−1.2|0.4</td><td>−3.6|-0.2</td><td>−10.7|-4.5</td><td>8.5|17.7</td><td>22.2|29.3</td><td>5.8|22.5</td><td>40.0|52.8</td><td>15.0|32.3</td></tr>
<tr><td rowspan="2">FUA</td><td>16.3</td><td>11.6</td><td>2.1</td><td>20.5</td><td>19.5</td><td>20.7</td><td>35.2</td><td>14.8</td></tr>
<tr><td>15.7|16.8</td><td>10.8|12.3</td><td>0.4|3.8</td><td>17.9|23.2</td><td>17.7|21.3</td><td>16.4|24.7</td><td>33.3|37.1</td><td>13.7|15.8</td></tr>
<tr><td rowspan="2">CEH</td><td>8.4</td><td>1.7</td><td>−21.5</td><td>5.6</td><td>9.9</td><td>10.8</td><td>29.4</td><td>34.3</td></tr>
<tr><td>6.4|10.5</td><td>−0.1|3.4</td><td>−26.5|-16.8</td><td>1.2|10.1</td><td>5.2|14.8</td><td>4.9|16.5</td><td>25.1|33.9</td><td>29.2|39.7</td></tr>
<tr><td rowspan="2">ADE</td><td>15.7</td><td>9.9</td><td>2.6</td><td>11.8</td><td>27.1</td><td>11.4</td><td>26.8</td><td>12.8</td></tr>
<tr><td>15.3|16.1</td><td>8.7|11.1</td><td>0.6|4.5</td><td>9.1|14.6</td><td>24.5|29.6</td><td>7.1|15.5</td><td>24.1|29.4</td><td>10.6|15.0</td></tr>
<tr><td rowspan="2">TRI</td><td>−6.5</td><td>−12.6</td><td>−35.7</td><td>0.2</td><td>−2</td><td>11.5</td><td>28.6</td><td>29.5</td></tr>
<tr><td>−8.6|-4.4</td><td>−14.6|-10.8</td><td>−40.6|-31.1</td><td>−5.0|5.6</td><td>−7.0|3.0</td><td>4.7|18.2</td><td>23.6|33.7</td><td>24.3|34.8</td></tr>
<tr><td rowspan="2">GER</td><td>−0.5</td><td>−5.6</td><td>−9.8</td><td>−7.1</td><td>15.3</td><td>−12.7</td><td>20.9</td><td>16.5</td></tr>
<tr><td>−1.5|0.5</td><td>−7.7|-3.5</td><td>−12.5|-7.1</td><td>−10.6|-3.7</td><td>11.2|19.5</td><td>−17.4|-7.8</td><td>16.5|24.7</td><td>11.4|21.9</td></tr>
<tr><td rowspan="2">CAP</td><td>−12.6</td><td>−24</td><td>−35.5</td><td>−28.4</td><td>−15.1</td><td>−17.4</td><td>6.8</td><td>8.2</td></tr>
<tr><td>−14.5|-10.7</td><td>−26.6|-21.6</td><td>−37.8|-33.2</td><td>−30.8|-26.3</td><td>−19.3|-11.1</td><td>−20.2|-14.8</td><td>4.7|8.8</td><td>6.4|9.9</td></tr>
<tr><td rowspan="2">SAP</td><td>1.3</td><td>−13.1</td><td>−26.6</td><td>−23.8</td><td>−4.7</td><td>−36</td><td>12.4</td><td>10.9</td></tr>
<tr><td>−0.6|3.0</td><td>−15.2|-11.1</td><td>−29.9|-23.5</td><td>−28.2|-19.3</td><td>−8.4|-1.0</td><td>−41.7|-30.0</td><td>9.5|15.5</td><td>9.1|12.9</td></tr>
<tr><td rowspan="2">ABS</td><td>−1.4</td><td>−6.9</td><td>−16.2</td><td>−2.3</td><td>−2</td><td>8.7</td><td>28.2</td><td>20.7</td></tr>
<tr><td>−3.3|0.4</td><td>−8.9|-5.1</td><td>−19.4|-13.0</td><td>−6.2|1.5</td><td>−4.9|1.1</td><td>2.6|15.1</td><td>25.9|30.6</td><td>19.3|22.1</td></tr>
<tr><td rowspan="2">COC</td><td>−90.7</td><td>−108.6</td><td>−119.7</td><td>−94</td><td>−64.8</td><td>−75.9</td><td>−15.2</td><td>14.4</td></tr>
<tr><td>−101.9|-79.4</td><td>−114.0|-103.5</td><td>−123.7|-115.9</td><td>−96.5|-91.7</td><td>−71.1|-58.4</td><td>−79.3|-72.5</td><td>−18.9|-11.7</td><td>10.2|18.9</td></tr>
</table>

(*continued on next page*)

Table D.1 (*continued*)

	Class 1	**Class 2**	**Class 3**	**Class 4**	**Class 5**	**Class 6**	**Class 7**	**Class 8**
FEN	1.6 −0.9|4.1	−4.8 −7.0|-2.8	−44.7 −49.2|-40.1	−30.7 −36.8|-24.4	−12.8 −18.3|-7.6	−24 −32.9|-15.0	−6.9 −11.9|-2.2	18.9 14.9|22.8
YUS	−39.6 −40.5|-38.7	−44.8 −47.9|-42.0	−38.5 −44.8|-32.3	−26.1 −34.4|-18.0	−1.6 −11.2|8.0	−67.9 −74.4|-61.1	−6.9 −12.5|-1.0	35 31.0|39.1

Table D.2
GHI RMSE (W/m^2) per variability class.

	Class 1	Class 2	Class 3	Class 4	Class 5	Class 6	Class 7	Class 8
ASP	24.6 23.4|25.8	35.1 31.5|38.8	52.1 46.1|58.4	83.3 77.4|89.2	62.3 56.2|68.7	113.1 106.0|120.4	104.4 98.6|110.3	84.3 76.5|92.4
KAL	30.6 29.5|31.8	32.3 29.6|35.3	51.2 46.3|56.0	75.4 68.7|82.0	68.6 63.1|74.4	100.7 95.0|106.8	104.7 99.5|110.4	100.5 92.8|108.0
DWN	20.8 18.8|23.0	33.6 31.1|36.3	70.7 63.8|77.7	99.3 93.3|105.5	61.4 57.3|66.3	144.3 138.9|149.5	141.3 135.3|147.4	118.9 111.0|126.7
ROC	22.2 21.7|22.7	28.1 25.3|31.1	47.3 41.8|52.8	87.5 83.1|91.7	48.2 45.1|51.4	127.6 122.8|132.4	104 100.0|107.9	83.3 78.2|88.3
SON	21.6 19.6|23.9	30.9 28.4|33.6	57 51.4|62.6	89.4 84.3|94.7	65.1 59.2|71.3	125.4 118.0|133.4	105.9 100.9|110.7	126.6 117.3|135.7
NEW	16.1 13.5|18.9	29.1 26.0|32.4	62.1 52.5|72.6	90.9 83.6|98.5	59.1 52.6|65.3	131.5 121.6|140.9	111.8 106.0|118.0	97.7 90.7|104.6
WAG	24.7 24.1|25.2	31.6 29.5|33.8	48.2 43.8|52.8	79.7 75.3|84.4	51.5 48.8|54.3	101 95.9|105.7	88.9 86.0|91.8	70.2 67.4|73.0
TAT	14.9 14.3|15.6	19.7 18.8|20.7	34.6 32.7|36.6	63.6 61.2|66.1	45.2 43.4|46.9	96.8 93.8|100.0	80.8 78.7|82.6	64.2 61.9|66.7
TUL	23.3 22.0|25.3	28.3 24.6|32.5	48.6 42.9|54.5	78 73.1|83.0	47.3 43.4|51.9	105.1 100.6|109.6	89.2 86.7|91.7	71 68.8|73.3
QIQ	26.7 23.2|30.2	43.3 37.7|49.4	66.3 53.7|78.8	66 57.6|74.7	49.2 44.3|54.1	82.3 69.4|95.8	65 60.0|70.4	68.5 58.6|80.1
LAU	24.1 16.2|32.1	61.5 48.4|75.7	86.1 77.4|95.2	128.5 118.8|137.5	78.1 70.6|86.0	159.6 149.7|168.9	118.1 112.7|123.5	125 118.1|132.0
HOW	25 20.4|29.9	49.4 46.2|52.6	90.1 77.5|101.8	114.5 102.6|126.5	70.6 65.8|75.2	142.7 128.2|157.6	104.8 98.4|110.9	108.7 97.6|120.1
TIR	36.1 30.3|41.9	57.7 54.6|60.7	103.2 95.8|110.3	131.6 122.7|140.6	96.7 91.4|102.1	147.9 135.8|159.8	117.5 111.3|124.1	99.5 88.4|111.0
GUR	73.6 62.2|83.8	79.9 75.4|84.4	145.3 126.4|162.8	143.9 126.2|160.5	92.3 87.3|97.5	171.4 150.7|192.2	102.8 96.5|109.1	101.4 90.6|112.9
TOW	23.1 22.6|23.7	28.8 25.3|32.7	43.5 38.1|49.1	80.6 74.5|86.9	51.4 47.1|56.0	123.2 117.0|129.6	108 103.4|112.6	87.3 81.7|93.6
BRO	24.5 23.5|25.8	38.1 34.8|42.0	54.2 48.2|60.4	74.6 70.2|78.9	66 60.4|72.0	115.8 107.9|123.9	108.4 102.7|114.3	80.3 74.3|86.9
MNM	24.5 23.2|25.8	35.8 33.7|38.1	46 43.5|48.4	54 51.7|56.4	46.3 43.9|48.8	70.9 68.8|73.1	83 80.2|85.9	77 72.6|81.5
KWA	123.8 87.9|157.2	97.6 81.9|115.1	94.9 89.6|100.2	77.4 73.1|81.7	71.9 62.8|81.1	99.1 91.8|107.2	89.4 82.5|96.3	100.4 90.0|110.4
LYU	33.8 27.9|40.3	79.8 66.9|93.3	112.5 104.5|120.5	118.2 113.5|122.9	60.6 53.2|68.1	135.3 132.2|138.6	96.7 94.3|99.0	94.8 92.2|97.2
ISH	17.9 16.2|19.6	33.6 29.0|38.6	55.8 50.4|61.8	72 69.2|74.8	53.2 49.2|57.7	101.1 97.8|104.5	87 85.0|88.8	65.8 63.8|67.7
LEA	36 34.9|37.1	42 39.8|44.3	47 40.8|54.3	65.2 59.2|71.1	51.2 47.5|55.0	93.5 85.3|101.9	97.3 89.2|105.2	96.5 77.8|114.8
FUA	21.9 21.4|22.4	23.9 22.5|26.0	41.3 38.0|44.7	74.7 71.2|78.5	45.5 43.4|47.7	99.9 96.1|104.1	84.5 82.2|86.8	51.4 50.0|52.7
CEH	20.3 18.3|22.0	30.1 27.6|33.1	74.7 65.2|84.2	80.1 75.1|85.2	61.4 55.6|67.3	104.5 99.7|109.2	96 91.9|100.3	97 89.4|105.0
ADE	20.5 20.1|21.0	23.9 21.5|26.4	37.1 33.8|40.4	61.3 58.1|64.5	48.5 45.6|51.3	81.8 77.7|85.5	78 75.5|80.9	59 56.8|61.1
TRI	22 18.3|26.1	39.8 34.2|45.4	77.2 69.6|84.7	82.9 77.3|87.9	74.2 67.7|81.5	104.3 99.0|109.7	103.8 98.5|109.1	96.4 89.1|103.7
GER	36.7 35.0|38.4	40.8 37.9|43.9	45.9 41.9|49.9	67.2 62.9|71.8	48.1 43.1|53.3	95.6 90.2|101.2	84.1 79.5|88.3	82.6 74.5|90.5
CAP	31.5 26.3|37.8	47.4 40.4|55.3	55.2 51.3|59.7	67.7 63.7|72.4	52.7 47.3|59.1	71.8 68.0|76.4	66.2 64.0|68.4	54 52.0|55.9
SAP	34.4 30.6|38.4	43 39.4|46.8	63.6 58.9|68.1	94.1 89.1|99.1	63.7 59.4|68.1	119.5 114.3|124.6	91.5 88.8|94.3	71.7 68.5|75.1

(*continued on next page*)

Table D.2 (*continued*)

<table>
<tr><th></th><th>Class 1</th><th>Class 2</th><th>Class 3</th><th>Class 4</th><th>Class 5</th><th>Class 6</th><th>Class 7</th><th>Class 8</th></tr>
<tr><td>ABS</td><td>42.3
35.7|48.8</td><td>37
31.3|42.9</td><td>60.3
53.6|66.8</td><td>70.5
65.8|75.2</td><td>58.9
55.3|62.5</td><td>91.4
85.4|97.5</td><td>72.4
70.3|74.6</td><td>55
53.5|56.5</td></tr>
<tr><td>COC</td><td>121.9
108.4|135.1</td><td>129.5
123.8|136.0</td><td>143.4
139.1|148.0</td><td>123.2
120.6|126.2</td><td>100.1
93.1|107.4</td><td>123.2
119.2|127.1</td><td>100.2
96.4|104.2</td><td>93.8
88.1|99.3</td></tr>
<tr><td>FEN</td><td>24.7
20.5|29.2</td><td>44.5
40.1|49.2</td><td>80.3
74.0|86.6</td><td>102.8
94.4|111.2</td><td>81
74.3|87.9</td><td>126.5
117.5|136.1</td><td>97.5
93.2|102.2</td><td>84.2
78.5|89.8</td></tr>
<tr><td>YUS</td><td>46.5
44.7|48.3</td><td>66.6
60.6|72.7</td><td>106.5
97.1|116.1</td><td>157.7
150.4|165.3</td><td>78.2
67.3|89.5</td><td>175.6
169.5|181.0</td><td>153.7
149.2|158.0</td><td>123.9
118.7|128.7</td></tr>
</table>

Table D.3
BNI MBE (W/m^2) per variability class.

<table>
<tr><th></th><th>Class 1</th><th>Class 2</th><th>Class 3</th><th>Class 4</th><th>Class 5</th><th>Class 6</th><th>Class 7</th><th>Class 8</th></tr>
<tr><td>**ASP**</td><td>12
10.1|13.7</td><td>42.2
37.5|46.6</td><td>33.3
26.4|40.1</td><td>80.9
71.6|90.1</td><td>114.5
102.6|126.1</td><td>90.3
76.2|104.4</td><td>164.8
154.8|174.7</td><td>61.7
54.0|69.0</td></tr>
<tr><td>**KAL**</td><td>−7
−10.1|-4.1</td><td>11.8
6.2|17.0</td><td>−11.6
−18.9|-4.5</td><td>43.4
34.8|52.3</td><td>91.1
78.8|103.6</td><td>63.1
53.1|73.4</td><td>149.2
140.8|157.6</td><td>63.6
55.7|71.3</td></tr>
<tr><td>**DWN**</td><td>−3.6
−6.8|-0.5</td><td>−5.2
−8.4|-1.8</td><td>−29.9
−36.6|-23.5</td><td>64.7
58.1|71.6</td><td>64.4
58.1|70.9</td><td>101.4
91.5|111.2</td><td>148
140.8|155.1</td><td>64.7
59.3|70.3</td></tr>
<tr><td>**ROC**</td><td>30.4
29.0|31.8</td><td>29.8
26.4|32.9</td><td>33.2
28.3|37.6</td><td>94.7
89.2|100.3</td><td>106
98.6|113.8</td><td>117.9
109.5|126.0</td><td>164.5
157.9|170.9</td><td>59.1
53.9|64.5</td></tr>
<tr><td>**SON**</td><td>−10.1
−16.3|-4.4</td><td>−2.1
−5.6|1.4</td><td>−22.9
−29.8|-16.5</td><td>19.6
10.8|28.3</td><td>43.8
36.6|51.5</td><td>48.6
35.5|62.3</td><td>111.3
104.1|118.8</td><td>63.7
56.9|71.0</td></tr>
<tr><td>**NEW**</td><td>31.6
29.2|33.8</td><td>22.1
17.6|26.8</td><td>11.1
2.6|19.1</td><td>73.3
63.8|83.7</td><td>98.3
85.3|111.0</td><td>69.2
56.3|82.2</td><td>143.3
134.9|152.1</td><td>69.7
62.1|77.0</td></tr>
<tr><td>**WAG**</td><td>32.8
31.5|34.0</td><td>33
30.0|35.7</td><td>35.5
30.1|40.7</td><td>97.7
90.9|104.5</td><td>106.4
99.8|113.4</td><td>93.5
84.1|102.5</td><td>150.2
144.4|156.2</td><td>55.1
51.0|59.3</td></tr>
<tr><td>**TAT**</td><td>−20.1
−21.5|-18.5</td><td>−29.2
−31.3|-27.1</td><td>−19.4
−22.3|-16.2</td><td>57.9
54.1|61.6</td><td>60.1
55.6|64.6</td><td>80.5
74.4|86.6</td><td>105.8
102.7|108.9</td><td>29.9
28.3|31.5</td></tr>
<tr><td>**TUL**</td><td>30.7
29.0|32.5</td><td>22.5
18.9|25.9</td><td>17.3
11.6|22.8</td><td>61
54.2|67.3</td><td>96.1
88.3|103.4</td><td>59.8
52.3|67.5</td><td>119.9
115.4|124.6</td><td>43.4
40.6|46.3</td></tr>
<tr><td>**QIQ**</td><td>−2
−10.6|6.6</td><td>−16.4
−25.5|-7.7</td><td>−65.7
−80.2|-51.2</td><td>1.7
−18.2|21.0</td><td>44.7
28.9|60.0</td><td>−10.1
−40.9|21.2</td><td>80.5
68.8|93.1</td><td>32
24.9|39.7</td></tr>
<tr><td>**LAU**</td><td>−13.3
−16.0|-10.9</td><td>−60
−68.1|-52.0</td><td>−76.3
−86.3|-66.7</td><td>−21.4
−33.5|-10.1</td><td>26.4
13.4|38.6</td><td>−4.5
−21.3|12.9</td><td>110.7
103.0|118.5</td><td>69.9
64.7|74.9</td></tr>
<tr><td>**HOW**</td><td>−46.4
−55.1|-37.9</td><td>−58
−62.1|-53.7</td><td>−97.1
−108.3|-86.3</td><td>−74.5
−88.1|-61.1</td><td>−37.5
−44.9|-30.1</td><td>−90
−104.4|-75.6</td><td>−2.4
−7.9|3.1</td><td>22.6
18.5|26.9</td></tr>
<tr><td>**TIR**</td><td>−44.5
−65.9|-22.9</td><td>−48.5
−58.3|-39.0</td><td>−106.2
−120.5|-91.6</td><td>−47.1
−61.1|-33.3</td><td>−46.9
−55.2|-38.8</td><td>−24.5
−43.9|-5.7</td><td>20.9
13.9|28.2</td><td>28.3
23.0|34.2</td></tr>
<tr><td>**GUR**</td><td>−118.6
−147.2|-89.3</td><td>−95.5
−103.3|-88.0</td><td>−161.3
−178.1|-144.5</td><td>−151.3
−169.2|-132.9</td><td>−87.6
−96.7|-77.8</td><td>−133.8
−159.0|-108.6</td><td>−44.4
−51.7|-37.0</td><td>11.6
8.0|15.3</td></tr>
<tr><td>**TOW**</td><td>17.3
15.2|19.3</td><td>23
20.0|26.2</td><td>29.1
24.4|33.4</td><td>125.8
119.4|132.1</td><td>108.2
100.2|115.5</td><td>166.1
155.2|176.5</td><td>184
176.7|191.1</td><td>65.7
59.9|71.6</td></tr>
<tr><td>**BRO**</td><td>8.3
6.6|9.9</td><td>4.9
1.1|8.8</td><td>1.9
−4.8|8.7</td><td>112.2
104.8|119.3</td><td>78.6
70.6|86.3</td><td>171.2
157.8|185.3</td><td>168.9
159.7|178.4</td><td>50.8
44.4|57.6</td></tr>
<tr><td>**MNM**</td><td>−60.4
−63.8|-57.0</td><td>−75.6
−78.8|-72.6</td><td>−57.3
−59.8|-54.9</td><td>−3.1
−5.5|-0.7</td><td>15.3
9.3|21.3</td><td>21.2
17.2|25.0</td><td>110.5
107.2|114.0</td><td>42.1
39.5|45.2</td></tr>
<tr><td>**KWA**</td><td>−194.9
−234.4|-162.5</td><td>−216.8
−239.9|-195.2</td><td>−190.3
−204.8|-177.0</td><td>−107.6
−118.4|-96.6</td><td>−33.3
−53.0|-14.4</td><td>−106.8
−121.9|-92.1</td><td>52.4
41.3|62.8</td><td>45.2
36.2|54.7</td></tr>
<tr><td>**LYU**</td><td>−85.7
−103.1|-69.5</td><td>−119.8
−136.7|-103.5</td><td>−97.3
−110.2|-85.0</td><td>−41.4
−48.5|-34.1</td><td>−2
−25.5|20.8</td><td>−58.6
−63.5|-53.9</td><td>56.9
54.0|60.1</td><td>22.4
20.9|23.9</td></tr>
<tr><td>**ISH**</td><td>−16.2
−20.1|-12.3</td><td>−31.6
−35.2|-28.0</td><td>−16.8
−20.4|-13.2</td><td>58
54.6|61.4</td><td>51.5
45.9|57.2</td><td>65.9
61.1|70.4</td><td>104.5
101.8|107.4</td><td>26.5
25.3|27.9</td></tr>
<tr><td>**LEA**</td><td>−48.3
−51.1|-45.5</td><td>−39.1
−45.4|-32.8</td><td>−12.8
−21.5|-4.6</td><td>77.9
67.0|87.8</td><td>75.1
64.1|86.3</td><td>105.4
89.1|121.0</td><td>163.4
151.7|175.4</td><td>55.1
43.4|68.1</td></tr>
<tr><td>**FUA**</td><td>−3.4
−5.3|-1.6</td><td>−2.6
−4.8|-0.5</td><td>0.8
−2.8|4.2</td><td>65.2
60.5|70.2</td><td>55
51.2|58.8</td><td>63.2
56.0|70.1</td><td>94.4
91.4|97.3</td><td>17.3
16.4|18.3</td></tr>
<tr><td>**CEH**</td><td>19
10.5|27.5</td><td>12.2
7.3|17.1</td><td>−10
−18.9|-1.3</td><td>56.6
49.1|64.2</td><td>67.9
58.9|77.0</td><td>68.7
59.9|77.6</td><td>98.9
93.1|104.8</td><td>47.1
42.3|52.4</td></tr>
<tr><td>**ADE**</td><td>28.5
27.5|29.5</td><td>27.2
23.7|30.3</td><td>37.3
32.5|42.0</td><td>106.6
100.3|113.0</td><td>106.3
98.9|113.9</td><td>130.5
121.4|139.7</td><td>139
133.9|144.4</td><td>37
34.3|40.0</td></tr>
<tr><td>**TRI**</td><td>−26.6
−33.2|-20.0</td><td>−17.5
−21.5|-13.3</td><td>−24.2
−32.2|-16.5</td><td>55.8
47.3|63.6</td><td>52.5
44.7|60.3</td><td>61.6
52.0|71.4</td><td>94.3
88.4|100.3</td><td>45.1
39.8|50.1</td></tr>
<tr><td>**GER**</td><td>−28.3
−31.7|-24.8</td><td>−32.4
−40.3|-24.7</td><td>−20.8
−29.9|-12.5</td><td>40.2
31.2|49.2</td><td>64
51.3|76.4</td><td>47.6
37.9|57.5</td><td>126.2
118.7|134.1</td><td>48.7
41.8|55.9</td></tr>
<tr><td>**CAP**</td><td>−59.8
−65.0|-55.2</td><td>−85.9
−92.2|-79.8</td><td>−88.8
−94.9|-82.7</td><td>−6.8
−12.0|-1.4</td><td>4.5
−4.2|13.6</td><td>27.8
22.2|33.5</td><td>82.7
79.1|86.1</td><td>22.7
20.9|24.5</td></tr>
<tr><td>**SAP**</td><td>−38.2
−43.9|-32.9</td><td>−63.2
−69.7|-56.5</td><td>−54
−61.8|-46.1</td><td>6.7
−1.3|15.2</td><td>54
44.5|63.7</td><td>−14.3
−24.5|-4.1</td><td>111
105.7|116.3</td><td>39.8
36.9|42.6</td></tr>
<tr><td>**ABS**</td><td>−37.5
−42.8|-32.7</td><td>−37.6
−43.7|-31.9</td><td>−34.9
−43.3|-27.5</td><td>38.4
30.3|46.2</td><td>43.5
37.3|49.7</td><td>48.2
36.4|59.9</td><td>103.5
99.1|107.9</td><td>22.2
20.7|23.8</td></tr>
<tr><td>**COC**</td><td>−285.2</td><td>−330.3</td><td>−319.9</td><td>−213.3</td><td>−99.2</td><td>−144.6</td><td>36.4</td><td>35.8</td></tr>
</table>

(*continued on next page*)

Table D.3 (*continued*)

<table>
<tr><th></th><th>Class 1</th><th>Class 2</th><th>Class 3</th><th>Class 4</th><th>Class 5</th><th>Class 6</th><th>Class 7</th><th>Class 8</th></tr>
<tr><td></td><td>−316.4|-253.0</td><td>−343.4|-317.5</td><td>−327.9|-311.9</td><td>−218.3|-208.3</td><td>−112.7|-83.9</td><td>−150.1|-139.1</td><td>32.5|40.5</td><td>32.2|39.6</td></tr>
<tr><td rowspan="2">FEN</td><td>−20.1</td><td>−32.7</td><td>−74.5</td><td>−14.1</td><td>3</td><td>−5</td><td>38.9</td><td>17.4</td></tr>
<tr><td>−27.4|-12.6</td><td>−36.5|-28.8</td><td>−82.0|-67.1</td><td>−23.0|-5.8</td><td>−4.2|10.0</td><td>−16.7|6.8</td><td>34.0|43.7</td><td>14.8|19.9</td></tr>
<tr><td rowspan="2">YUS</td><td>−92.4</td><td>−81.7</td><td>−33.8</td><td>75.9</td><td>135.3</td><td>43.1</td><td>125.3</td><td>67.3</td></tr>
<tr><td>−95.6|-89.4</td><td>−90.1|-73.2</td><td>−46.2|-21.1</td><td>63.3|88.2</td><td>112.8|156.6</td><td>32.2|53.3</td><td>118.4|132.6</td><td>62.2|72.5</td></tr>
</table>

Table D.4
BNI RMSE (W/m^2) per variability class.

<table>
<tr><th></th><th>Class 1</th><th>Class 2</th><th>Class 3</th><th>Class 4</th><th>Class 5</th><th>Class 6</th><th>Class 7</th><th>Class 8</th></tr>
<tr><td rowspan="2">ASP</td><td>78.5</td><td>99.7</td><td>115.1</td><td>175.1</td><td>175.5</td><td>209.2</td><td>236.6</td><td>138</td></tr>
<tr><td>74.8|82.2</td><td>93.8|105.5</td><td>106.7|124.9</td><td>168.2|182.3</td><td>164.1|186.8</td><td>197.1|222.0</td><td>225.5|246.9</td><td>121.4|153.8</td></tr>
<tr><td rowspan="2">KAL</td><td>111</td><td>98.4</td><td>123</td><td>165.9</td><td>166.3</td><td>194.5</td><td>220.6</td><td>153.3</td></tr>
<tr><td>107.0|115.2</td><td>91.4|105.7</td><td>114.8|131.4</td><td>158.7|173.6</td><td>157.0|175.4</td><td>186.5|202.6</td><td>211.3|229.8</td><td>137.0|168.0</td></tr>
<tr><td rowspan="2">DWN</td><td>69.3</td><td>88.7</td><td>125.8</td><td>170.2</td><td>127.7</td><td>233.4</td><td>213.3</td><td>130.8</td></tr>
<tr><td>64.4|74.5</td><td>84.9|92.4</td><td>119.5|132.6</td><td>164.4|176.0</td><td>122.7|133.0</td><td>226.1|240.8</td><td>205.6|220.7</td><td>121.3|140.2</td></tr>
<tr><td rowspan="2">ROC</td><td>51</td><td>71.2</td><td>96</td><td>176.1</td><td>145.8</td><td>223.7</td><td>226.1</td><td>120.5</td></tr>
<tr><td>48.9|53.3</td><td>66.5|76.6</td><td>88.9|103.5</td><td>171.0|181.4</td><td>138.1|153.7</td><td>217.5|229.8</td><td>218.9|233.4</td><td>109.8|130.6</td></tr>
<tr><td rowspan="2">SON</td><td>59.2</td><td>72</td><td>100</td><td>131.7</td><td>117.3</td><td>168.5</td><td>165.6</td><td>130.5</td></tr>
<tr><td>53.6|64.5</td><td>67.4|76.9</td><td>92.5|107.5</td><td>124.2|139.1</td><td>111.1|123.3</td><td>157.3|179.0</td><td>158.0|173.8</td><td>118.6|142.7</td></tr>
<tr><td rowspan="2">NEW</td><td>59.5</td><td>80.5</td><td>112.7</td><td>174.9</td><td>158.8</td><td>202.9</td><td>212.9</td><td>149.9</td></tr>
<tr><td>56.0|63.1</td><td>75.3|85.8</td><td>102.6|123.4</td><td>165.9|183.6</td><td>145.4|171.9</td><td>193.0|212.8</td><td>203.0|222.4</td><td>136.1|163.3</td></tr>
<tr><td rowspan="2">WAG</td><td>53.3</td><td>71.8</td><td>108.1</td><td>180.7</td><td>155</td><td>206</td><td>215</td><td>116.3</td></tr>
<tr><td>51.3|55.4</td><td>68.3|75.4</td><td>101.8|114.2</td><td>174.8|186.6</td><td>148.9|161.3</td><td>199.5|212.8</td><td>208.6|221.5</td><td>108.4|124.2</td></tr>
<tr><td rowspan="2">TAT</td><td>54.8</td><td>72.7</td><td>84.1</td><td>128.2</td><td>118.8</td><td>170.8</td><td>160.6</td><td>84.4</td></tr>
<tr><td>52.6|57.2</td><td>70.3|75.1</td><td>81.2|86.9</td><td>125.1|131.5</td><td>114.0|123.8</td><td>165.9|175.8</td><td>156.5|164.7</td><td>79.7|88.9</td></tr>
<tr><td rowspan="2">TUL</td><td>53.3</td><td>72.4</td><td>105.2</td><td>161.2</td><td>146.1</td><td>187.8</td><td>185.5</td><td>97.1</td></tr>
<tr><td>50.7|56.9</td><td>66.9|78.2</td><td>98.2|112.9</td><td>155.8|166.7</td><td>138.8|153.1</td><td>182.3|194.1</td><td>180.3|190.5</td><td>91.1|102.7</td></tr>
<tr><td rowspan="2">QIQ</td><td>105</td><td>120</td><td>133.4</td><td>138.8</td><td>158.3</td><td>175.4</td><td>145.7</td><td>84.5</td></tr>
<tr><td>90.4|120.1</td><td>111.2|129.6</td><td>120.6|147.3</td><td>123.9|154.2</td><td>142.4|174.7</td><td>153.5|197.5</td><td>129.8|162.3</td><td>65.1|102.9</td></tr>
<tr><td rowspan="2">LAU</td><td>62.4</td><td>142.7</td><td>188.5</td><td>220.1</td><td>173.4</td><td>264.5</td><td>223.9</td><td>171.3</td></tr>
<tr><td>51.1|74.1</td><td>125.1|159.5</td><td>175.8|201.8</td><td>209.7|230.4</td><td>162.6|184.5</td><td>252.6|276.5</td><td>214.7|232.4</td><td>160.2|181.8</td></tr>
<tr><td rowspan="2">HOW</td><td>78.2</td><td>96.1</td><td>137.4</td><td>141.9</td><td>106.1</td><td>157.4</td><td>80.8</td><td>61</td></tr>
<tr><td>65.9|90.2</td><td>91.5|100.7</td><td>125.8|149.3</td><td>130.7|153.3</td><td>98.3|114.1</td><td>146.1|168.7</td><td>74.6|86.9</td><td>50.3|71.8</td></tr>
<tr><td rowspan="2">TIR</td><td>114.3</td><td>126.9</td><td>171.8</td><td>160.6</td><td>125.2</td><td>155.9</td><td>113.4</td><td>86.8</td></tr>
<tr><td>97.6|130.5</td><td>119.5|134.3</td><td>160.9|183.0</td><td>151.7|169.8</td><td>119.3|131.0</td><td>142.3|168.6</td><td>102.6|124.6</td><td>69.4|103.1</td></tr>
<tr><td rowspan="2">GUR</td><td>179.7</td><td>157.7</td><td>202.2</td><td>192.6</td><td>162.2</td><td>200.6</td><td>91.4</td><td>37.2</td></tr>
<tr><td>155.7|202.5</td><td>150.1|165.1</td><td>187.1|217.1</td><td>175.9|208.5</td><td>154.6|169.8</td><td>180.4|218.8</td><td>84.1|98.8</td><td>31.7|42.8</td></tr>
<tr><td rowspan="2">TOW</td><td>62</td><td>74.7</td><td>89.3</td><td>182.9</td><td>153.3</td><td>245.3</td><td>235.7</td><td>130.4</td></tr>
<tr><td>60.1|63.8</td><td>70.8|78.9</td><td>84.0|95.0</td><td>176.4|189.8</td><td>145.1|161.0</td><td>236.4|254.4</td><td>228.0|242.8</td><td>118.9|141.7</td></tr>
<tr><td rowspan="2">BRO</td><td>70.9</td><td>104.5</td><td>129.2</td><td>188.3</td><td>146.3</td><td>264.5</td><td>241.4</td><td>117.4</td></tr>
<tr><td>68.6|73.4</td><td>100.1|109.3</td><td>121.7|136.8</td><td>182.4|194.1</td><td>140.1|152.4</td><td>253.9|275.5</td><td>231.6|251.8</td><td>103.4|130.9</td></tr>
<tr><td rowspan="2">MNM</td><td>96.5</td><td>113.7</td><td>113.5</td><td>117.1</td><td>113.7</td><td>138.4</td><td>162.4</td><td>96.8</td></tr>
<tr><td>93.0|100.0</td><td>109.9|117.8</td><td>110.5|116.5</td><td>114.5|119.7</td><td>107.9|119.9</td><td>135.0|141.7</td><td>158.2|166.7</td><td>89.5|104.1</td></tr>
<tr><td rowspan="2">KWA</td><td>228.4</td><td>248.7</td><td>234.9</td><td>175</td><td>122.7</td><td>192.5</td><td>125.1</td><td>100.9</td></tr>
<tr><td>177.8|291.3</td><td>221.8|276.2</td><td>219.9|251.3</td><td>165.2|184.7</td><td>108.9|136.7</td><td>178.8|206.0</td><td>113.0|137.6</td><td>82.8|117.9</td></tr>
<tr><td rowspan="2">LYU</td><td>117.6</td><td>179.7</td><td>190.3</td><td>153.6</td><td>138.6</td><td>156</td><td>104.3</td><td>57.6</td></tr>
<tr><td>95.7|143.4</td><td>158.8|201.1</td><td>175.1|204.5</td><td>147.2|160.4</td><td>120.4|156.3</td><td>151.8|160.4</td><td>100.1|108.5</td><td>53.2|61.9</td></tr>
<tr><td rowspan="2">ISH</td><td>61.3</td><td>90.3</td><td>106.3</td><td>142.8</td><td>114.5</td><td>178.3</td><td>155.7</td><td>70.7</td></tr>
<tr><td>54.2|68.3</td><td>83.9|96.7</td><td>101.2|111.4</td><td>139.7|145.8</td><td>109.6|119.7</td><td>174.4|182.2</td><td>152.3|159.2</td><td>67.2|74.4</td></tr>
<tr><td rowspan="2">LEA</td><td>135.1</td><td>148</td><td>120.3</td><td>157.3</td><td>147.1</td><td>198.3</td><td>222.1</td><td>127.3</td></tr>
<tr><td>131.3|138.7</td><td>140.4|155.7</td><td>110.5|130.8</td><td>149.3|165.2</td><td>137.7|155.9</td><td>184.7|211.6</td><td>208.5|235.6</td><td>97.2|155.9</td></tr>
<tr><td rowspan="2">FUA</td><td>48.6</td><td>64.4</td><td>81.3</td><td>142.9</td><td>103.1</td><td>176.4</td><td>150.6</td><td>47.4</td></tr>
<tr><td>46.9|50.2</td><td>62.2|66.8</td><td>77.5|85.1</td><td>138.4|147.8</td><td>99.7|106.4</td><td>170.3|182.2</td><td>146.5|154.5</td><td>44.3|50.3</td></tr>
<tr><td rowspan="2">CEH</td><td>74.1</td><td>80.9</td><td>127.5</td><td>139.9</td><td>129.9</td><td>167.8</td><td>154.2</td><td>98.4</td></tr>
<tr><td>64.7|83.9</td><td>76.4|85.7</td><td>116.6|137.4</td><td>133.9|146.0</td><td>122.6|137.2</td><td>160.0|175.4</td><td>147.4|161.5</td><td>89.6|107.6</td></tr>
<tr><td rowspan="2">ADE</td><td>44.1</td><td>65.2</td><td>94.9</td><td>176.8</td><td>157.3</td><td>215.4</td><td>199</td><td>80.3</td></tr>
<tr><td>42.9|45.3</td><td>60.4|70.3</td><td>89.1|100.8</td><td>170.9|182.9</td><td>149.2|165.7</td><td>206.2|224.3</td><td>192.8|205.5</td><td>73.2|87.6</td></tr>
<tr><td rowspan="2">TRI</td><td>69.6</td><td>85.6</td><td>119.4</td><td>142.1</td><td>125.3</td><td>160.1</td><td>152.1</td><td>101.3</td></tr>
<tr><td>61.9|77.8</td><td>80.3|91.1</td><td>111.1|127.9</td><td>135.7|148.5</td><td>118.9|131.6</td><td>152.4|167.9</td><td>145.5|158.7</td><td>91.0|111.0</td></tr>
<tr><td rowspan="2">GER</td><td>121.9</td><td>137.3</td><td>132.2</td><td>163.5</td><td>142.9</td><td>178.9</td><td>187.3</td><td>114.8</td></tr>
<tr><td>116.3|127.2</td><td>126.6|147.5</td><td>121.4|143.4</td><td>156.0|170.8</td><td>130.4|157.1</td><td>170.6|187.0</td><td>177.9|197.1</td><td>94.7|132.8</td></tr>
<tr><td rowspan="2">CAP</td><td>94.3</td><td>125.6</td><td>139.6</td><td>144.6</td><td>114.8</td><td>148.3</td><td>140.4</td><td>57.5</td></tr>
<tr><td>89.2|100.1</td><td>116.7|136.8</td><td>133.1|146.5</td><td>140.0|149.3</td><td>104.9|125.9</td><td>143.2|153.4</td><td>135.4|145.5</td><td>50.8|64.2</td></tr>
<tr><td rowspan="2">SAP</td><td>114.8</td><td>140.7</td><td>147.8</td><td>164.2</td><td>169.6</td><td>198.5</td><td>203.1</td><td>111.8</td></tr>
<tr><td>103.7|126.2</td><td>130.0|151.3</td><td>138.6|156.4</td><td>157.0|171.1</td><td>157.8|181.1</td><td>190.8|205.9</td><td>196.3|209.4</td><td>104.7|118.6</td></tr>
<tr><td rowspan="2">ABS</td><td>125.5</td><td>116.3</td><td>147.9</td><td>151.1</td><td>128.4</td><td>179.4</td><td>164.1</td><td>59.5</td></tr>
<tr><td>111.4|139.2</td><td>103.0|130.0</td><td>133.3|162.8</td><td>143.1|159.3</td><td>121.5|135.5</td><td>169.9|188.6</td><td>158.3|170.2</td><td>54.2|64.5</td></tr>
<tr><td rowspan="2">COC</td><td>359</td><td>371.8</td><td>360.5</td><td>267</td><td>192.4</td><td>213</td><td>115</td><td>88.3</td></tr>
<tr><td>328.1|386.8</td><td>359.6|384.0</td><td>353.3|367.6</td><td>262.7|271.6</td><td>179.1|206.1</td><td>208.1|217.9</td><td>109.4|120.6</td><td>79.3|97.4</td></tr>
<tr><td rowspan="2">FEN</td><td>74.2</td><td>90.1</td><td>133.2</td><td>132.8</td><td>106.1</td><td>163.4</td><td>108.7</td><td>54.3</td></tr>
<tr><td>62.7|86.9</td><td>84.3|96.0</td><td>124.9|141.8</td><td>125.5|140.0</td><td>99.5|112.6</td><td>153.8|172.9</td><td>102.3|115.0</td><td>46.5|61.7</td></tr>
<tr><td rowspan="2">YUS</td><td>121.4</td><td>162.4</td><td>204.9</td><td>236.4</td><td>214.4</td><td>252.4</td><td>219.6</td><td>168.8</td></tr>
<tr><td>113.9|129.5</td><td>145.9|178.9</td><td>187.4|221.8</td><td>224.3|247.7</td><td>194.7|234.4</td><td>243.6|260.4</td><td>210.6|228.8</td><td>157.9|179.8</td></tr>
</table>

Data availability

The authors do not have permission to share data.

References

ABoM, 2012. Australian one minute solar radiation data. http://www.bom.gov.au/climate/data/oneminsolar/about-IDCJAC0022.shtml.

ABoM, 2022. http://www.bom.gov.au/research/publications/researchreports/BRR-062.pdf.

Barker, Howard W., Davies, John A., 1992. Solar radiative fluxes for stochastic, scale-invariant broken cloud fields. J. Atmos. Sci. 49 (13), 1115–1126. https://doi.org/10.1175/1520-0469(1992)049<1115:SRFFSS>2.0.CO;2.

Beyer, Hans Georg, Costanzo, Claudio, Heinemann, Detlev, 1996. Modifications of the Heliosat procedure for irradiance estimates from satellite images. In: Sol. Energy 56 (3), 207–212. https://doi.org/10.1016/0038-092X(95)00092-6.

Blanc, Ph., Wald, L., 2012. The SG2 algorithm for a fast and accurate computation of the position of the Sun for multi-decadal time period. In: Sol. Energy 86 (10), 3072–3083. https://doi.org/10.1016/j.solener.2012.07.018.

Blanc, P., Jolivet, R., Ménard, L., Saint-Drenan, Y-M., 2022. Data sharing of in-situ measurements following GEO and FAIR principles in the solar energy sector ⟨hal-03811628⟩.

Bright, Jamie M., 2019. Solcast: Validation of a satellite-derived solar irradiance dataset. In: Sol. Energy 189, 435–449. https://doi.org/10.1016/j.solener.2019.07.086.

Cano, D., Monget, J.M., Albuisson, M., Guillard, H., Regas, N., Wald, L., 1986. A method for the determination of the global solar radiation from meteorological satellite data. In: Sol. Energy 37 (1), 31–39. https://doi.org/10.1016/0038-092X(86)90104-0.

Carreno, Ignacio Losada, Ramakrishna, Raksha, Scaglione, Anna, Arnold, Daniel, Roberts, Ciaran, Ngo, Sy-Toan, et al., 2020. SoDa: An Irradiance-Based Synthetic Solar Data Generation Tool. In: 2020 IEEE International Conference on Communications, Control, and Computing Technologies for Smart Grids (SmartGridComm). Tempe, AZ, USA, 11/11/2020–11/13/2020. Institute of Electrical and Electronics Engineers; IEEE Communications Society. Piscataway, NJ: IEEE, pp. 1–6.

Cho, H.-M., et al., 2015. Frequency and causes of failed MODIS cloud property retrievals for liquid phase clouds over global oceans. J. Geophys. Res. Atmos. 120. https://doi.org/10.1002/2015JD023161.

Damiani, Alessandro, Irie, Hitoshi, Horio, Takashi, Takamura, Tamio, Khatri, Pradeep, Takenaka, Hideaki, et al., 2018. Evaluation of Himawari-8 surface downwelling solar radiation by ground-based measurements. In: Atmos. Meas. Tech. 11 (4), 2501–2521. https://doi.org/10.5194/amt-11-2501-2018.

de Miranda, Diego Rodrigues, Azam, Faiza, Lezaca, Jorge, Saint-Drenan, Yves-Marie, Schroedter-Homscheidt, Marion, 2026. Cloud type and aerosol aware solar irradiance variability classification for solar resource assessment. Renew. Energy 263, 125387. ISSN 0960-1481. https://doi.org/10.1016/j.renene.2026.1253.

Deneke, H.M., Feijt, A.J., Roebeling, R.A., 2008. Estimating surface solar irradiance from METEOSAT SEVIRI-derived cloud properties. In: Remote Sens. Environ. 112 (6), 3131–3141. https://doi.org/10.1016/j.rse.2008.03.012.

Driemel, Amelie, Augustine, John, Behrens, Klaus, Colle, Sergio, Cox, Christopher, Cuevas-Agulló, Emilio, et al., 2018. Baseline surface radiation network (BSRN): structure and data description (1992–2017). In: Earth Syst. Sci. Data 10 (3), 1491–1501. https://doi.org/10.5194/essd-10-1491-2018.

El Alani, Omaima, Ghennioui, Hicham, Ghennioui, Abdellatif, Saint-Drenan, Yves-Marie, Blanc, Philippe, Hanrieder, Natalie, Dahr, Fatima-Ezzahra, 2021. A visual support of standard procedures for solar radiation quality control. In: Int. J. Renew. Energy Dev. 10 (3), 401–414. https://doi.org/10.14710/ijred.2021.34806.

Forstinger, A., Wilbert, S., Jensen, A., Kraas, B., Fernández-Peruchena, Carlos M., Gueymard, C., Ronzio, D., Yang, D., Collino, E., Polo, J., Ruiz-Arias, J., Blanc, P., Saint-Drenan, Yves-M., 2023. Worldwide Benchmark of Modelled Solar Irradiance Data 2023 PVPS Task 16 Solar Resource for High Penetration and Large Scale.

Frey, R.A., Ackerman, S.A., Liu, Y., Strabala, K.I., Zhang, H., Key, J.R., Wang, X., 2008. Cloud detection with MODIS. Part I: improvements in the MODIS cloud mask for Collection 5. J. Atmos. Oceanic Technol. 25 (7), 1057–1072.

Gautier, Catherine, Diak, Georges, Masse, Serge, 1980. A simple physical model to estimate incident solar radiation at the surface from GOES satellite data. In: J. Appl. Meteorol. 19 (8), 1005–1012. https://doi.org/10.1175/1520-0450(1980)019<1005:ASPMTE>2.0.CO;2.

Geiger, Bernhard, Meurey, Catherine, Lajas, Dulce, Franchistéguy, Laurent, Carrer, Dominique, Roujean, Jean-Louis, 2008. Near real-time provision of downwelling shortwave radiation estimates derived from satellite observations. In: Meteorol. Appl. 15 (3), 411–420. https://doi.org/10.1002/met.84.

Geuder, N., Wolfertstetter, F., Wilbert, S., Schüler, D., Affolter, R., Kraas, B., et al., 2015. Screening and flagging of solar irradiation and ancillary meteorological data. In: Energy Procedia 69, 1989–1998. https://doi.org/10.1016/j.egypro.2015.03.205.

Girodo, Marco, Mueller, Richard W., Heinemann, Detlev, 2006. Influence of three-dimensional cloud effects on satellite derived solar irradiance estimation—First approaches to improve the Heliosat method. In: Sol. Energy 80 (9), 1145–1159. https://doi.org/10.1016/j.solener.2005.09.005.

Greuell, W., Meirink, J.F., Wang, P., 2013. Retrieval and validation of global, direct, and diffuse irradiance derived from SEVIRI satellite observations. In: JGR-Atmos. 118 (5), 2340–2361. https://doi.org/10.1002/jgrd.50194.

Gschwind, Benoit, Wald, Lucien, Blanc, Philippe, Lefèvre, Mireille, Schroedter-Homscheidt, Marion, Arola, Antti, 2019. Improving the McClear model estimating the downwelling solar radiation at ground level in cloud-free conditions – McClear v3. In: metz 28 (2), 147–163. https://doi.org/10.1127/metz/2019/0946.

Gueymard, Christian A., 2017. Cloud and albedo enhancement impacts on solar irradiance using high-frequency measurements from thermopile and photodiode radiometers. Part 1: impacts on global horizontal irradiance. In: Sol. Energy 153, 755–765. https://doi.org/10.1016/j.solener.2017.05.004.

Habte, A.M., Sengupta, M., 2019. Data Quality Assessment Using SERI-QC. National Renewable Energy Lab.(NREL), Golden, CO (United States).

Hammer, Annette, Heinemann, Detlev, Hoyer, Carsten, Kuhlemann, Rolf, Lorenz, Elke, Müller, Richard, Beyer, Hans Georg, 2003. Solar energy assessment using remote sensing technologies. In: Remote Sens. Environ. 86 (3), 423–432. https://doi.org/10.1016/S0034-4257(03)00083-X.

Hao, Dalei, Asrar, Ghassem R., Zeng, Yelu, Zhu, Qing, Wen, Jianguang, Xiao, Qing, Chen, Min, 2020. DSCOVR/EPIC-derived global hourly and daily downward shortwave and photosynthetically active radiation data at $0.1^{\circ} \times 0.1^{\circ}$ resolution. In: Earth Syst. Sci. Data 12 (3), 2209–2221. https://doi.org/10.5194/essd-12-2209-2020.

Hartmann, Bálint, 2020. Comparing various solar irradiance categorization methods – A critique on robustness. In: Renew. Energy 154, 661–671. https://doi.org/10.1016/j.renene.2020.03.055.

Hou, Ning, Zhang, Xiaotong, Zhang, Weiyu, Wei, Yu, Jia, Kun, Yao, Yunjun, et al., 2020. Estimation of surface downward shortwave radiation over China from Himawari-8 AHI data based on random forest. In: Remote Sens. 12 (1), 181. https://doi.org/10.3390/rs12010181.

IEA, 2022. https://www.iea.org/reports/world-energy-outlook-2022.

Igawa, N., 2014. Improving the All Sky Model for the luminance and radiance distributions of the sky. Sol. Energy 105, 354–372. https://doi.org/10.1016/j.solener.2014.03.020.

Jiang, Hou, Lu, Ning, Qin, Jun, Tang, Wenjun, Yao, Ling, 2019. A deep learning algorithm to estimate hourly global solar radiation from geostationary satellite data. In: Renew. Sust. Energ. Rev. 114, 109327. https://doi.org/10.1016/j.rser.2019.109327.

Jiang, B., Han, J., Liang, H., Liang, S., Yin, X., Peng, J., He, T., Ma, Y., 2023. The Hi-GLASS all-wave daily net radiation product: Algorithm and product validation. Sci. Remote Sens. 7, 100080. https://doi.org/10.1016/j.srs.2023.100080.

Klüser, L., Killius, N., Gesell, G., 2015. APOLLO_NG – a probabilistic interpretation of the APOLLO legacy for AVHRR heritage channels. In: Atmos. Meas. Tech. 8 (10), 4155–4170. https://doi.org/10.5194/amt-8-4155-2015.

Kriebel, K.T., Saunders, R.W., Gesell, G., 1989. Optical properties of clouds derived from fully cloudy AVHRR pixels. Beitr. Phys. Atmos. 62 (3), 165–171.

Laszlo, Istvan, Liu, Hongqing, Kim, Hye-Yun, Pinker, Rachel T., 2020. Shortwave radiation from ABI on the GOES-R series. In: The GOES-R Series. Elsevier, pp. 179–191 libinsitu: https://libinsitu.readthedocs.io/en/latest/index.html.

Lefèvre, M., Oumbe, A., Blanc, P., Espinar, B., Gschwind, B., Qu, Z., et al., 2013. McClear: a new model estimating downwelling solar radiation at ground level in clear-sky conditions. In: Atmos. Meas. Tech. 6 (9), 2403–2418. https://doi.org/10.5194/amt-6-2403-2013.

Letu, Husi, Yang, Kun, Nakajima, Takashi Y., Ishimoto, Hiroshi, Nagao, Takashi M., Riedi, Jérôme, et al., 2020. High-resolution retrieval of cloud microphysical properties and surface solar radiation using Himawari-8/AHI next-generation geostationary satellite. In: Remote Sens. Environ. 239, 111583. https://doi.org/10.1016/j.rse.2019.111583.

Letu, Husi, Nakajima, Takashi Y., Wang, Tianxing, Shang, Huazhe, Ma, Run, Yang, Kun, et al., 2022. A new benchmark for surface radiation products over the East Asia–Pacific Region retrieved from the Himawari-8/AHI next-generation geostationary satellite. In: Bull. Am. Meteorol. Soc. 103 (3), E873–E888. https://doi.org/10.1175/BAMS-D-20-0148.1.

Letu, Husi, Ma, Run, Nakajima, Takashi Y., Shi, Chong, Hashimoto, Makiko, Nagao, Takashi M., et al., 2023. Surface solar radiation compositions observed from Himawari-8/9 and Fengyun-4 Series. In: Bull. Am. Meteorol. Soc. 104 (10), E1772–E1789. https://doi.org/10.1175/BAMS-D-22-0154.1.

Li, Jun, Tang, Wenjun, Qi, Jingwen, Yan, Zhenyu, 2023. Mapping high-resolution surface shortwave radiation over East Asia with the new generation geostationary meteorological satellite Himawari-8. In: Int. J. Digital Earth 16 (1), 323–336. https://doi.org/10.1080/17538947.2023.2172225.

Linares-Rodriguez, Alvaro, Ruiz-Arias, José Antonio, Pozo-Vazquez, David, Tovar-Pescador, Joaquin, 2013. An artificial neural network ensemble model for estimating global solar radiation from Meteosat satellite images. In: Energy 61, 636–645. https://doi.org/10.1016/j.energy.2013.09.008.

Long, C.N., Dutton, E.G., 2002. BSRN Global Network Recommended QCtests, V2.0. Baseline Surface Radiation Network. https://bsrn.awi.de/fileadmin/user_upload/bsrn.awi.de/Publications/BSRN_recommended_QC_tests_V2.pdf.

Lopez, V.A.M., van Urk, G., Doodkorte, P.J.F., Zeman, M., Isabella, O., Ziar, H., 2024. Using sky-classification to improve the short-term prediction of irradiance with sky images and convolutional neural networks. Solar Energy 269, 112320. https://doi.org/10.1016/j.solener.2024.112320. ISSN 0038-092X.

Long, C.N., Shi, Y., 2008. An automated quality assessment and control algorithm for surface radiation measurements. In: TOASCJ 2 (1), 23–37. https://doi.org/10.2174/1874282300802010023.

Ma, Run, Letu, Husi, Yang, Kun, Wang, Tianxing, Shi, Chong, Xu, Jian, et al., 2020. Estimation of surface shortwave radiation from Himawari-8 satellite data based on a combination of radiative transfer and deep neural network. In: IEEE Trans. Geosci. Remote Sens. 58 (8), 5304–5316. https://doi.org/10.1109/TGRS.2019.2963262.

Mayer, B., Kylling, A., 2005. Technical note: the libRadtran software package for radiative transfer calculations - description and examples of use. In: Atmos. Chem. Phys. 5 (7), 1855–1877. https://doi.org/10.5194/acp-5-1855-2005.

Mayer, B., Kylling, A., Emde, C., Buras, R., Hamann, U., 2010. libRadtran: library for radiative transfer calculations. Edition 1.0 for libRadtran version 1.5-beta. http://www.libradtran.org (accessed at 10 April 2013).

McCandless, T.C., Haupt, S.E., Young, G.S., 2016. A regime-dependent artificial neural network technique for short-range solar irradiance forecasting. In: Renew. Energy 89, 351–359. https://doi.org/10.1016/j.renene.2015.12.030.

Meher, Jitendra Kumar, Rizvi, Syed Haider Abbas, Choudhary, Bhramar, Choudhary, Ravi, Thakre, Yash, Kumar, Ritesh, Singh, Vikram, 2024. Validating Meteosat Second Generation and Himawari-8 derived solar irradiance against ground measurements: Solarad AI's approach. In: Energies 17 (12), 2913. https://doi.org/10.3390/en17122913.

Mol, Wouter, van Heerwaarden, Chiel, 2025. Mechanisms of surface solar irradiance variability under broken clouds (2025). Atmos. Chem. Phys. 25 (8), 4419–4441. https://doi.org/10.5194/acp-25-4419-2025.

Mol, Wouter B., van Stratum, Bart J.H., Knap, Wouter H., van Heerwaarden, Chiel C., 2023. Reconciling observations of solar irradiance variability with cloud size distributions. In: JGR-Atmos. 128 (5). https://doi.org/10.1029/2022JD037894. Artikel e2022JD037894.

Mol, Wouter, Heusinkveld, Bert, Mangan, Mary Rose, Hartogensis, Oscar, Veerman, Menno, van Heerwaarden, Chiel, 2024. Observed patterns of surface solar irradiance under cloudy and clear-sky conditions. In: Q. J. R. Meteorol. Soc. 150 (761), 2338–2363. https://doi.org/10.1002/qj.4712.

Möser, Werner, Raschke, Ehrhard, 1984. Incident solar radiation over Europe estimated from METEOSAT Data. In: J. Climate Appl. Meteor. 23 (1), 166–170. https://doi.org/10.1175/1520-0450(1984)023%3C0166:ISROEE%3E2.0.CO;2.

Mueller, R.W., Matsoukas, C., Gratzki, A., Behr, H.D., Hollmann, R., 2009. The CM-SAF operational scheme for the satellite based retrieval of solar surface irradiance — A LUT based eigenvector hybrid approach. In: Remote Sens. Environ. 113 (5), 1012–1024. https://doi.org/10.1016/j.rse.2009.01.012.

Nijsse, Femke J.M.M., Mercure, Jean-Francois, Ameli, Nadia, Larosa, Francesca, Kothari, Sumit, Rickman, Jamie, et al., 2023. The momentum of the solar energy transition. In: Nat. Commun. 14 (1), 6542. https://doi.org/10.1038/s41467-023-41971-7.

Nouri, B., Wilbert, S., Blum, N., Fabel, Y., Lorenz, E., Hammer, A., Schmidt, T., Zarzalejo, L.F., Pitz-Paal, R., 2023. Probabilistic solar nowcasting based on all-sky imagers. Sol. Energy 253, 285–307. https://doi.org/10.1016/j.solener.2023.01.060.

Ohmura, A., Dutton, E.G., Forgan, B., Fröhlich, C., Gilgen, H., Hegner, H., Heimo, A., König-Langlo, G., McArthur, B., Müller, G., Philipona, R., Pinker, R., Whitlock, C.H., Dehne, K., Wild, M., 1998. Baseline surface radiation network (BSRN/WCRP): new precision radiometry for climate research. B. Am. Meteorol. Soc. 79, 2115–2136. https://doi.org/10.1175/1520-0477(1998)079<2115:BSRNBW>2.0.CO;2.

Perez, Richard, Ineichen, Pierre, Moore, Kathy, Kmiecik, Marek, Chain, Cyril, George, Ray, Vignola, Frank, 2002. A new operational model for satellite-derived irradiances: description and validation. In: Sol. Energy 73 (5), 307–317. https://doi.org/10.1016/S0038-092X(02)00122-6.

Pérez-Ortiz, María, Jiménez-Fernández, Silvia, Gutiérrez, Pedro, Alexandre, Enrique, Hervás-Martínez, César, Salcedo-Sanz, Sancho, 2016. A review of classification problems and algorithms in renewable energy applications. In: Energies 9 (8), 607. https://doi.org/10.3390/en9080607.

Pinker, R.T., Ewing, J.A., 1985. Modeling surface solar radiation: model formulation and validation. In: J. Clim. Appl. Meteorol. 24 (5), 389–401. https://doi.org/10.1175/1520-0450(1985)024<0389:MSSRMF>2.0.CO;2.

Pinker, R.T., Laszlo, I., Tarpley, J.D., Mitchell, K., 2002. Geostationary satellite parameters for surface energy balance. In: Adv. Space Res. 30 (11), 2427–2432. https://doi.org/10.1016/S0273-1177(02)80296-4.

Pinker, R.T., Laszlo, I., 1992. Modeling surface solar irradiance for satellite applications on a global scale. J. Appl. Meteor. 31, 194–211. https://doi.org/10.1175/1520-0450(1992)031<0194:MSSIFS>2.0.CO;2.

Polo, J., Wilbert, S., Ruiz-Arias, J.A., Meyer, R., Gueymard, C., Suri, M., Martín, L., Mieslinger, T., Blanc, P., Granti, I., Boland, J., Ineichen, P., Remund, J., Escobar, R., Troccoli, A., Sengupta, M., Nielsen, K.P., Renne, D., Geuder, N., Cebecauer, T., 2016. Preliminary survey on site-adaptation techniques for satellite-derived and reanalysis solar radiation datasets. Sol. Energy 132, 25–37.

Qin, Yi, Huang, Jing, McVicar, Tim R., West, Sam, Khan, Maryam, Steven, Andrew D.L., 2021. Estimating surface solar irradiance from geostationary Himawari-8 over Australia: a physics-based method with calibration. Sol. Energy 220 (2021), 119–129. ISSN 0038-092X. https://doi.org/10.1016/j.solener.2021.03.029.

Qu, Zhipeng, Oumbe, Armel, Blanc, Philippe, Espinar, Bella, Gesell, Gerhard, Gschwind, Benoît, et al., 2017. Fast radiative transfer parameterisation for assessing the surface solar irradiance: the Heliosat 4 method. In: metz 26 (1), 33–57. https://doi.org/10.1127/metz/2016/0781.

Rayati, Mohammad, de Falco, Pasquale, Proto, Daniela, Bozorg, Mokhtar, Carpita, Mauro, 2021. Generation data of synthetic high frequency solar irradiance for data-driven decision-making in electrical distribution grids. In: Energies 14 (16), 4734. https://doi.org/10.3390/en14164734.

Rigollier, C., Lefèvre, M., Wald, L., 2004. The method Heliosat-2 for deriving shortwave solar radiation from satellite images. In: Sol. Energy 77 (2), 159–169. https://doi.org/10.1016/j.solener.2004.04.017.

Riihimaki, Laura D., Li, Xinya, Hou, Zhangshuan, Berg, Larry K., 2021. Improving prediction of surface solar irradiance variability by integrating observed cloud characteristics and machine learning. In: Sol. Energy 225, 275–285. https://doi.org/10.1016/j.solener.2021.07.047.

Salamalikis, V., Tzoumanikas, P., Argiriou, A.A., Kazantzidis, A., 2022. Site adaptation of global horizontal irradiance from the Copernicus Atmosphere Monitoring Service for radiation using supervised machine learning techniques. Renew. Energy 195, 92–106.

Saunders, R.W., Kriebel, K.T., 1988. An improved method for detecting clear sky and cloudy radiances from AVHRR data. Int. J. Remote Sens. 9, 123–150. https://doi.org/10.1080/01431168808954841.

Schade, N.H., Macke, A., Sandmann, H., Stick, C., 2007. Enhanced solar global irradiance during cloudy sky conditions. Meteorol. Z. 16, 295–304.

Schaible, Jonas, Nouri, Bijan, Höpken, Lars, Kotzab, Tim, Loevenich, Matthias, Blum, Niklas, et al., 2024. Application of nowcasting to reduce the impact of irradiance ramps on PV power plants. In: EPJ Photovolt. 15, 15. https://doi.org/10.1051/epjpv/2024009.

Schmetz, Johannes, 1989. Towards a surface radiation climatology: Retrieval of downward irradiances from satellites. In: Atmos. Res. 23 (3–4), 287–321. https://doi.org/10.1016/0169-8095(89)90023-9.

Schmidt, T., Stührenberg, J., Blum, N., Lezaca, J., Annette, H., Wilbert, S., Bijan, N., Schroedter-Homscheidt, M., Heinemann, D., Vogt, T., et al., 2025. Eye2Sky–a network of all-sky imager and meteorological measurement stations for high resolution nowcasting of solar irradiance. In: Meteorol. Z. 34 (2025), 35. https://doi.org/10.1127/metz/2025/1245.

Schreck, Sebastian, Schroedter-Homscheidt, Marion, Klein, Martin, Cao, Karl Kiên, 2020. Satellite image-based generation of high frequency solar radiation time series for the assessment of solar energy systems. In: metz 29 (5), 377–392. https://doi.org/10.1127/metz/2020/1008.

Schroedter-Homscheidt, Marion, Kosmale, Miriam, Jung, Sandra, Kleissl, Jan, 2018. Classifying ground-measured 1 minute temporal variability within hourly intervals for direct normal irradiances. In: metz 27 (2), 161–179. https://doi.org/10.1127/metz/2018/0875.

Schroedter-Homscheidt, Marion, Azam, Faiza, Betcke, Jethro, Hanrieder, Natalie, Lefèvre, Mireille, Saboret, Lauren, Saint-Drenan, Yves-Marie, 2022. Surface solar irradiation retrieval from MSG/SEVIRI based on APOLLO Next Generation and HELIOSAT-4 methods. Meteorol. Z. 31 (6), 455–476. https://doi.org/10.1127/metz/2022/1132 (2022).

Schuurman, K.R., Meyer, A., 2024. Surface Solar Radiation: AI Satellite Retrieval Can Outperform Heliosat and Generalizes Well to Other Climate Zones. Online available at http://arxiv.org/pdf/2409.16316v1.

Sengupta, Manajit, Xie, Yu, Lopez, Anthony, Habte, Aron, Maclaurin, Galen, Shelby, James, 2018. The National Solar Radiation Data Base (NSRDB). In: Renew. Sust. Energ. Rev. 89, 51–60. https://doi.org/10.1016/j.rser.2018.03.003.

Shi, Hongrong, Li, Weiwei, Fan, Xuehua, Zhang, Jinqiang, Hu, Bo, Husi, Letu, et al., 2018. First assessment of surface solar irradiance derived from Himawari-8 across China. In: Sol. Energy 174, 164–170. https://doi.org/10.1016/j.solener.2018.09.015.

Stephens, G.L., Ackerman, S., Smith, E.A., 1984. A shortwave parameterization revised to improve cloud absorption. J. Atmos. Sci. 41, 687–690.

Takenaka, Hideaki, Nakajima, Takashi Y., Higurashi, Akiko, Higuchi, Atsushi, Takamura, Tamio, Pinker, Rachiel T., Nakajima, Teruyuki, 2011. Estimation of solar radiation using a neural network based on radiative transfer. In: J. Geophys. Res. 116 (D8). https://doi.org/10.1029/2009JD013337.

Tan, Yunhui, Wang, Quan, Zhang, Zhaoyang, 2023. Near-real-time estimation of global horizontal irradiance from Himawari-8 satellite data. In: Renew. Energy 215, 118994. https://doi.org/10.1016/j.renene.2023.118994.

Tarpley, J.D., 1979. Estimating incident solar radiation at the surface from geostationary satellite data. In: J. Appl. Meteorol. 18 (9), 1172–1181. https://doi.org/10.1175/1520-0450(1979)018%3C1172:EISRAT%3E2.0.CO;2.

Urraca, Ruben, Huld, Thomans, Gracia-Amillo, Ana, Martinez-de-Pison, Francisco Javier, Kaspar, Frank, Sanz-Garcia, Andres, 2018. Evaluation of global horizontal irradiance estimates from ERA5 and COSMO-REA6 reanalyses using ground and satellite-based data. Sol. Energy 164 (2018), 339–354. ISSN 0038-092X. https://doi.org/10.1016/j.solener.2018.02.059.

Valor, Enric, Puchades, Jesus, Niclos, Raquel, Galve Romero, Joan Miquel, Lacave, Oriol, Puig, Patricia, 2023. Determination and evaluation of surface solar irradiance with the MAGIC-Heliosat method adapted to MTSAT-2/Imager and Himawari-8/AHI sensors. In: IEEE Trans. Geosci. Remote Sens. 61, 1–19. https://doi.org/10.1109/TGRS.2023.3238180.

Verbois, Hadrien, Saint-Drenan, Yves-Marie, Becquet, Vadim, Gschwind, Benoit, Blanc, Philippe, 2023. Retrieval of surface solar irradiance from satellite imagery using machine learning: pitfalls and perspectives. In: Atmos. Meas. Tech. 16 (18), 4165–4181. https://doi.org/10.5194/amt-16-4165-2023.

Xie, Yu, Sengupta, Manajit, Dudhia, Jimy, 2016. A Fast All-sky Radiation Model for Solar applications (FARMS): algorithm and performance evaluation. In: Sol. Energy 135, 435–445. https://doi.org/10.1016/j.solener.2016.06.003.

Yu, Yuechi, Shi, Jiancheng, Wang, Tianxing, Letu, Husi, Yuan, Pengfei, Zhou, Wang, Hu, Lu, 2019. Evaluation of the Himawari-8 shortwave downward radiation (SWDR) product and its comparison with the CERES-SYN, MERRA-2, and ERA-Interim datasets. In: IEEE J. Sel. Top. Appl. Earth Observ. Remote Sens. 12 (2), 519–532. https://doi.org/10.1109/JSTARS.2018.2851965.

Yu, Yue-Chi, Shi, Jiancheng, Wang, Tianxing, Letu, Husi, Zhao, Changjun, 2021. All-sky total and direct surface shortwave downward radiation (SWDR) estimation from satellite: applications to MODIS and Himawari-8. In: Int. J. Appl. Earth Obs. Geoinf. 102, 102380. https://doi.org/10.1016/j.jag.2021.102380.